Shell Structures

Theory and Applications

Volume 4

Editors: Wojciech Pietraszkiewicz & Wojciech Witkowski

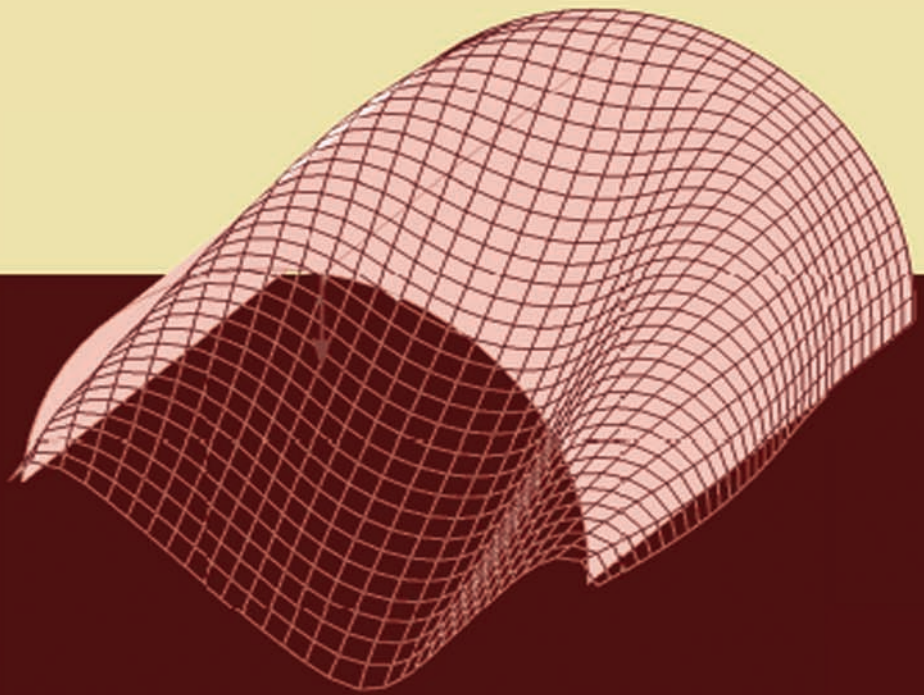

CRC Press
Taylor & Francis Group
A BALKEMA BOOK

Taylor & Francis
Taylor & Francis Group
http://taylorandfrancis.com

PROCEEDINGS OF THE 11TH INTERNATIONAL CONFERENCE "SHELL STRUCTURES: THEORY AND APPLICATIONS" (SSTA 2017), OCTOBER 11–13, 2017, GDANSK, POLAND

Shell Structures: Theory and Applications Volume 4

Editors

Wojciech Pietraszkiewicz & Wojciech Witkowski
Faculty of Civil and Environmental Engineering, Department of Mechanics of Materials and Structures, Gdansk University of Technology, Gdańsk, Poland

CRC Press
Taylor & Francis Group
Boca Raton London New York Leiden

CRC Press is an imprint of the
Taylor & Francis Group, an **informa** business
A BALKEMA BOOK

CRC Press/Balkema is an imprint of the Taylor & Francis Group, an informa business

Typeset by MPS Limited, Chennai, India
Printed and bound in Great Britain by CPI Group (UK) Ltd, Croydon, CR0 4YY

Published by: CRC Press/Balkema
Schipholweg 107C, 2316 XC Leiden, The Netherlands
e-mail: Pub.NL@taylorandfrancis.com
www.crcpress.com – www.taylorandfrancis.com

ISBN: 978-1-138-05045-7 (Hbk)
ISBN: 978-1-315-16660-5 (eBook)

Shell Structures: Theory and Applications Volume 4 – Pietraszkiewicz & Witkowski (eds)
© 2018 Taylor & Francis Group, London, ISBN 978-1-138-05045-7

Table of contents

Stability

Dynamics

Numerical analysis

Engineering design

Biomechanical problems

Miscellaneous topics

Taylor & Francis
Taylor & Francis Group
http://taylorandfrancis.com

Shell Structures: Theory and Applications Volume 4 – Pietraszkiewicz & Witkowski (eds)
© 2018 Taylor & Francis Group, London, ISBN 978-1-138-05045-7

Preface

Conferences "Shell Structures: Theory and Applications" are traditionally organized by the Section of Structural Mechanics of the Committee for Civil Engineering of the Polish Academy of Sciences in co-operation with other scientific and technological organizations. Previous SSTA conferences were held in Cracow (1974), Gołuń (1978), Opole (1982), Szklarska Poręba (1986), Janowice (1992), Jurata (1998, 2002, 2005, 2009) and Gdańsk (2013). The aim of the meetings is always the same: to bring together scientists, engineers, and other specialists of shell structures in order to discuss important results and new ideas in the field. The goal is to pursue more accurate theoretical models, to develop more powerful and versatile methods of analysis, as well as to disseminate expertise in design and maintenance of shell structures.

Three volumes *Shell Structures: Theory and Applications* published by Taylor & Francis Group, London 2006, 2010, and 2014 contained full texts of papers presented at the 8th, 9th and 10th SSTA Conferences held in Gdańsk (Poland), respectively. These three books have met with a considerable response of the international shell community.

This fourth volume of the series contains full texts of 132 papers selected for presentation at the 11th Conference "Shell Structures: Theory and Applications" to be held on October 11–13, 2017 in Gdańsk (Poland). The papers reflect a wide spectrum of scientific and engineering problems of shell structures. For readers convenience, the contents of the book is divided into eight thematic groups of papers: general lectures, theoretical modelling, stability, dynamics, numerical analyses, engineering problems, biomechanical applications, and miscellaneous topics. We do hope that information presented in this volume will be of interest to academics, students, designers and engineers dealing with various problems of thin-walled shell structures.

We would like to express our gratitude to all Authors for their valuable contributions and for their willingness to share their research and development activities with the shell international community. We are particularly grateful to the Authors of Invited General Lectures, Professors: E. Carrera & M. Petrolo (Italy), H. Fu & Y. Zhang (PR China), T. Lewiński *et al.* (Poland), S. Reese *et al.* (Germany), and J.M. Rotter (United Kingdom) for their exceptionally valuable and extensive contributions to this volume.

Each manuscript submitted to 11th SSTA and printed in this volume has been reviewed by a member of the International Advisory Board and then refined by the Author(s) according to the referee comments. We are deeply indebted to all members of the International Advisory Board for their important role in shaping the Conference program and for their great help in bringing all the papers to highest research standards. Most of the final texts have additionally been adjusted to technical requirements of the publisher, remaining printing errors have been corrected, and the English of some texts has been refined. We would like to thank very much indeed our associates T. Ferenc, D. Bruski, K. Daszkiewicz, R. Kędra, B. Kotarska-Lewandowska, M. Kujawa, J. Lachowicz, A. Sabik, M. Skowronek, B. Sobczyk, B. Zima for their invaluable help in bringing the book to its final form.

Financial support provided by SOFiSTiK AG, Nürnberg, Germany; Pomorska Okregowa Izba Inzynierów Budownictwa, Gdansk, Poland; PORR S.A., Warsaw, Poland; Gotowski BKiP, Bydgoszcz, Poland; Sika Poland Sp. z o.o, Warsaw, Poland; Design Office of Municipal Engineering (BPBK S.A.), Gdańsk, Poland is gratefully acknowledged.

Gdańsk, July 2017

Wojciech Pietraszkiewicz
Wojciech Witkowski

Taylor & Francis
Taylor & Francis Group
http://taylorandfrancis.com

Shell Structures: Theory and Applications Volume 4 – Pietraszkiewicz & Witkowski (eds)
© 2018 Taylor & Francis Group, London, ISBN 978-1-138-05045-7

Organizers

The Committee on Civil Engineering and Hydroengineering of the Polish Academy of Sciences, Section of Structural Mechanics and Materials

Polish Society of Theoretical and Applied Mechanics

The Committee on Mechanics of the Polish Academy of Sciences

Polish Association for Computational Mechanics

Gdańsk University of Technology, Faculty of Civil and Environmental Engineering, Department of Mechanics of Materials and Structures, Department of Structural Mechanics

Taylor & Francis
Taylor & Francis Group
http://taylorandfrancis.com

Shell Structures: Theory and Applications Volume 4 – Pietraszkiewicz & Witkowski (eds)
© 2018 Taylor & Francis Group, London, ISBN 978-1-138-05045-7

Acknowledgments

We are grateful for the financial support given by the following institutions:

SOFiSTiK AG, Oberschleißheim, Germany
Pomorska Okręgowa Izba Inżynierów Budownictwa, Gdańsk, Poland
PORR S.A., Warsaw, Poland
Gotowski BKiP, Bydgoszcz, Poland
Sika Poland Sp. z o.o., Warsaw, Poland
Design Office of Municipal Engineering (BPBK S.A.), Gdańsk, Poland

Taylor & Francis
Taylor & Francis Group
http://taylorandfrancis.com

Shell Structures: Theory and Applications Volume 4 – Pietraszkiewicz & Witkowski (eds)
© 2018 Taylor & Francis Group, London, ISBN 978-1-138-05045-7

Committees

INTERNATIONAL ADVISORY BOARD

W. Pietraszkiewicz (Poland) – Chairman
H. Altenbach (Germany)
M. Amabili (Canada)
J. Awrejcewicz (Poland)
J. Błachut (UK / Poland)
E. Carrera (Italy)
J. Chróścielewski (Poland)
P.G. Ciarlet (Hong Kong, China)
V.A. Eremeyev (Russia / Poland)
J. Górski (Poland)
D.H. Hodges (USA)
Y. Huang (USA)
M. Kleiber (Poland)
P. Kłosowski (Poland)
Z. Kołakowski (Poland)
S.N. Korobeynikov (Russia)
I. Kreja (Poland)
T. Lewiński (Poland)
K. Magnucki (Poland)
G.I. Mikhasev (Belarus)
P. Neff (Germany)
J.N. Reddy (USA)
J.M. Rotter (UK)
E. Ramm (Germany)
S. Shimizu (Japan)
D.J. Steigmann (USA)
F. Tornabene (Italy)
W. Wagner (Germany)
K. Wisniewski (Poland)
W. Witkowski (Poland)
A. Zingoni (UK, South Africa)

ORGANIZING COMMITTEE

Wojciech Witkowski– Chairman,
Jarosław Górski – Vice-Chairman,
Stanisław Burzyński, Tomasz Ferenc – Secretaries,
D. Bruski, K. Daszkiewicz, M. Jasina, R. Kędra, B. Kotarska-Lewandowska, A. Kryczałło, M. Kujawa, J. Lachowicz, H. Małyszczyk, M. Rucka, A. Sabik, M. Skowronek, B. Sobczyk, B. Zima

Taylor & Francis
Taylor & Francis Group
http://taylorandfrancis.com

General lectures

Taylor & Francis
Taylor & Francis Group
http://taylorandfrancis.com

Shell Structures: Theory and Applications Volume 4 – Pietraszkiewicz & Witkowski (eds)
© 2018 Taylor & Francis Group, London, ISBN 978-1-138-05045-7

Computational models for the multifield analysis of laminated shells and related best theory diagrams

E. Carrera & M. Petrolo
MUL^2 Group, Department of Mechanical and Aerospace Engineering,
Politecnico di Torino, Italy

ABSTRACT: This paper presents plate and shell models for multifield problems and proposes methodologies to refine structural models according to given accuracy and computational cost requirements. In multifield problems for multilayered structures, refined models are necessary to deal with many non-classical effects due, for instance, to the presence of large variations of properties among layers. In such research scenario, the Carrera Unified Formulation (CUF) is a well-established framework. Via the CUF, the 3D structural problem is reduced to a 2D or 1D variant. In other words, the 3D unknown variables become 2D or 1D, and expansion functions along the thickness or the cross-section of the structure define the order of the model, or computational cost and its accuracy. The CUF models proved to be able to detect 3D-like accuracies in multifield structural problems with very low computational costs. In the CUF framework, the axiomatic-asymptotic method (AAM) has been recently proposed by the authors to investigate the influence of each unknown variable on the solution of a given problem. Additionally, using the AAM, Best Theory Diagrams (BTD) have been obtained to read the minimum number of terms of a refined model for a given accuracy. The BTD generates guidelines to develop and evaluate structural models. In other words, via the BTD, a trade-off between accuracy and computational cost can be made. In this paper, mechanical, thermal and electrical fields are considered and BTDs are presented for various problems.

1 INTRODUCTION

Many engineering structures require multifield analyses for their proper design. For instance, thermal and mechanical loads and interaction thereof are important for space vehicles and turbine blades. Piezoelectric and mechanical loads are fundamental in smart structures. An accurate structural analysis of such structures requires refined structural models to capture non-classical effects. In particular, the paper presents plate and shell models for multifield analysis and a technique to build the models to fit the given problems precisely.

The refinement process of a plate or shell model, referred to as 2D models, is aimed at the improvement of the accuracy of classical models, such as the Kirchhoff-Love (Kirchhoff 1850, Love 1927) and Reissner-Mindlin theory (Reissner 1945, Mindlin 1951). The examples of refined 2D models are given by Vlasov (1957), Hildebrand, Reissner, & Thomas (1938), and the Zig-Zag model of Lekhnitskii (1968). In the case of multilayered structures, models are usually developed according to two approaches: the Equivalent Single Layer (ESL) and the Layer Wise (LW) schemes. According to the ESL scheme, the number of the unknowns is not affected by the number of layers, while, the LW scheme models each layer of the plate with its displacement unknowns, and, therefore, the number of unknowns of the model is related to the number of layers of the plate (Reddy 1997).

A review of methodologies for thermoelasticity can be found in (Hetnarski & Eslami 2009). The 2D structural models for thermoelasticity have been developed over the last decades for isotropic, anisotropic and heterogeneous structures (Tauchert 1991, Noor & Burton 1992, Murakami 1993, Argyris & Tenek 1997). Particular attention was paid to predictor-corrector procedures, the effect of temperature-dependence of the material properties, and the sensitivity of the thermomechanical response to variations in the material parameters, and non-linear effects.

Electromechanical effects must be considered in piezoelectric structures. Such systems are increasingly used as sensors, actuators and energy harvesters for various applications, including control and health-monitoring. The 2D reference ESL structural models for piezoelectric structures can be found in (Tiersten 1969, Mindlin 1972, Yang & Yu 1993). On the other hand, an LW model for the electric potential coupled with an ESL displacement field can be found in (Mitchell & Reddy 1995).

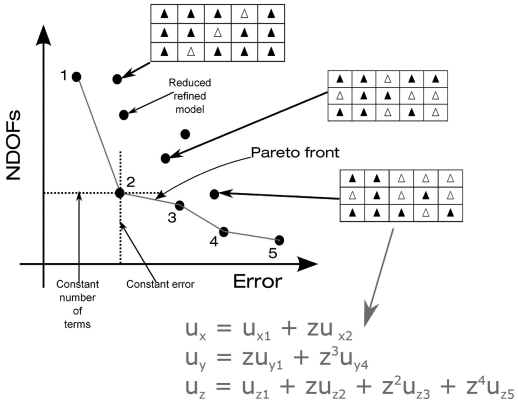

Figure 1. The Best Theory Diagram.

This work makes use of the Carrera Unified Formulation (CUF) to build refined 2D models (Carrera et al. 2014). The CUF introduced a systematic approach to develop any-order structural model via a few fundamental nuclei whose formal expressions do not depend neither on the order of the model nor on the type of expansions adopted to describe the unknown variable fields (Carrera 2003). In particular, ESL, LW and mixed variational formulations can be implemented (Carrera et al. 2011). The CUF has been extensively used for multifield analyses over the recent years. Reference works are those by Carrera (2002) and Ballhause et al. (2005).

In the CUF framework, the axiomatic-asymptotic method (AAM) has been recently proposed by the authors to investigate the influence of each unknown variable on the solution of a given problem (Carrera & Petrolo 2010, Carrera & Petrolo 2011). In the AAM the starting model is used with a full expansion of variables. The influence of each variable, or groups of variables, is evaluated by deactivating it. Only those variables exhibiting an influence are retained and reduced models are built in which the number of unknown variables is less or equal to the starting full model. The method can be iterated to evaluate the influence of characteristic parameter such as thickness or orthotropic ratios, similarly to an asymptotic method. Recently, the AAM has been applied to multifield problems (Cinefra et al. 2015, Carrera et al. 2015). A systematic use of CUF and AAM led to the definition of Best Theory Diagrams (BTD) in which, for a given accuracy and problem, the minimum number of required unknown variables can be read, as shown in Fig. 1. The BTD can be seen as a tool to evaluate the accuracy and the computational efficiency of any given structural model against the best available. The BTD for multifield problems has been recently presented in (Cinefra et al. 2017). This paper is organized as follows: the CUF is introduced in Section 2, governing equation in Section 3, the AAM and BTD in Section 4. The results are presented in Section 5 and Conclusions in Section 6.

2 CARRERA UNIFIED FORMULATION

In the CUF, the displacement field for a 2D model can be written as

$$\mathbf{u}(x,y,z) = F_\tau(z)\mathbf{u}_\tau(x,y) \qquad \tau = 1,\ldots,N+1 \quad (1)$$

where the Einstein notation is assumed on the index τ. $\mathbf{u}$ is the displacement vector $(u_x\, u_y\, u_z)$. F_τ are the so-called thickness expansion functions and $\mathbf{u}_\tau$ is the vector of the generalized unknown displacements. In ESL, F_τ are defined on the overall thickness of the plate, while, in LW, for each k-layer. For ESL, F_τ can be Mc-Laurin expansions of z, defined as $F_\tau = z^{\tau-1}$. In the following, the ESL models are indicated as EDN, in which N is the expansion order. For instance, the ED3 displacement field is

$$\begin{aligned} u_x &= u_{x_1} + z\,u_{x_2} + z^2\,u_{x_3} + z^3\,u_{x_4} \\ u_y &= u_{y_1} + z\,u_{y_2} + z^2\,u_{y_3} + z^3\,u_{y_4} \\ u_z &= u_{z_1} + z\,u_{z_2} + z^2\,u_{z_3} + z^3\,u_{z_4} \end{aligned} \quad (2)$$

The LW models can be obtained via Legendre polynomial expansions in each layer,

$$\begin{aligned} &\mathbf{u}^k = F_t \cdot \mathbf{u}_t^k + F_b \cdot \mathbf{u}_b^k + F_r \cdot \mathbf{u}_r^k = F_\tau \mathbf{u}_\tau^k \\ &\tau = t,b,r \;\; r = 2,3,\ldots,N \quad k = 1,2,\ldots,N_L \end{aligned} \quad (3)$$

where N_L is the number of the layers. Subscripts t and b correspond to the top and bottom surfaces of the layer. Functions F_τ depend on the coordinate ζ_k, $-1 \le \zeta_k \le 1$. F_τ are linear combinations of the Legendre polynomials,

$$\begin{aligned} F_t &= \tfrac{P_0+P_1}{2} \qquad F_b = \tfrac{P_0-P_1}{2} \\ F_r &= P_r - P_{r-2} \qquad r = 2,3,\ldots,N \end{aligned} \quad (4)$$

In the following, the LW models are denoted by the acronym as LDN, where N is the expansion order. For instance, LD3 is

$$\begin{aligned} u_x^k &= F_t\,u_{xt}^k + F_2\,u_{x2}^k + F_3\,u_{x3}^k + F_b\,u_{xb}^k \\ u_y^k &= F_t\,u_{yt}^k + F_2\,u_{y2}^k + F_3\,u_{y3}^k + F_b\,u_{yb}^k \\ u_z^k &= F_t\,u_{zt}^k + F_2\,u_{z2}^k + F_3\,u_{z3}^k + F_b\,u_{zb}^k \end{aligned} \quad (5)$$

The ESL and LW descriptions can be used for multifield variables, such as temperature or potential. For instance, the LW description of the temperature distribution is

$$\begin{aligned} &\theta^k(x,y,z) = F_t \cdot \theta_t^k(x,y) + F_r \cdot \theta_r^k(x,y) + \\ &+F_b \cdot \theta_b^k(x,y) = F_\tau \theta_\tau^k(x,y) \end{aligned} \quad (6)$$

where θ_τ^k are

$$\theta_\tau^k = \overline{\theta}_\tau^k - \theta_e \quad (7)$$

$\overline{\theta}_\tau^k$ is the effective temperature distribution. The temperature distribution can be defined by solving the

conduction equation for a given temperature distribution over the lateral, top and bottom surfaces. The approach proposed in Eq. (6) offers the possibility to impose continuity of the temperature distribution along the thickness direction. In (Carrera 2002), further details on the temperature distribution evaluation can be found. On the other hand the assumed profiles can be used, such as the linear one,

$$\theta_z = \theta_z^0 \frac{2\,z}{h} + \overline{\theta}_0 \tag{8}$$

where h is the total thickness of the plate and the parameters θ_z^0 and $\overline{\theta}_0$ are the imposed top and bottom values.

In an electro-mechanical problem, the potential distribution can be defined as

$$\begin{array}{l} \Phi^k = F_t\Phi_t^k + F_r\Phi_r^k + F_b\Phi_b^k = F_\tau\Phi_\tau^k \\ \tau = t, r, b \;\; r = 2, 3, \ldots, N \end{array} \tag{9}$$

3 CONSTITUTIVE AND GOVERNING EQUATIONS

In this section, a brief overview of some of the constitutive equations adopted for multifield problems are given. For a more comprehensive overview, books from the authors can be referred to (Carrera et al. 2014, Carrera et al. 2011). Linear strain-displacement relations are assumed and strain components are grouped into in-plane (p) and out-of-plane (n), components,

$$\boldsymbol{\epsilon}_p^k = \begin{bmatrix} \epsilon_{xx}^k & \epsilon_{yy}^k & \epsilon_{xy}^k \end{bmatrix}^T \qquad \boldsymbol{\epsilon}_n^k = \begin{bmatrix} \epsilon_{xz}^k & \epsilon_{yz}^k & \epsilon_{zz}^k \end{bmatrix}^T \tag{10}$$

For a pure mechanical case, stress components for a generic layer k can be obtained by means of the Hooke law,

$$\boldsymbol{\sigma}^k = \mathbf{C}^k\boldsymbol{\epsilon}^k \tag{11}$$

The virtual variation of the strain energy is

$$\delta\, L_{int}^k = \sum_{k=1}^{N_L} \int_{V_k} \left(\delta\boldsymbol{\epsilon}_p^k \cdot \boldsymbol{\sigma}_p^k + \delta\boldsymbol{\epsilon}_n^k \cdot \boldsymbol{\sigma}_n^k \right) dV_k =$$

$$\sum_{k=1}^{N_L} \int_{\Omega_k} \int_{A_k} \left(\delta\boldsymbol{\epsilon}_p^k \cdot \boldsymbol{\sigma}_p^k + \delta\boldsymbol{\epsilon}_n^k \cdot \boldsymbol{\sigma}_n^k \right) d\Omega_k\, dz_k \tag{12}$$

In the case of the uncoupled thermo-mechanical analysis, thermal stresses are given by

$$\begin{array}{l} \boldsymbol{\sigma}_{pT}^k = \mathbf{C}_{pp}^k \cdot \boldsymbol{\epsilon}_{pT}^k + \mathbf{C}_{pn}^k \cdot \boldsymbol{\epsilon}_{nT}^k \\ \boldsymbol{\sigma}_{nT}^k = \mathbf{C}_{pn}^k \cdot \boldsymbol{\epsilon}_{pT}^k + \mathbf{C}_{nn}^k \cdot \boldsymbol{\epsilon}_{nT}^k \end{array} \tag{13}$$

Applying the thermal expansion coefficient vector α,

$$\begin{array}{l} \boldsymbol{\epsilon}_{pT}^k = \left\{ \alpha_1^k,\ \alpha_2^k,\ 0 \right\} \theta^k(x,y,z) = \boldsymbol{\alpha}_p^k \theta^k \\ \boldsymbol{\epsilon}_{nT}^k = \left\{ 0,\quad 0,\quad \alpha_3^k \right\} \theta^k(x,y,z) = \boldsymbol{\alpha}_n^k \theta^k \end{array} \tag{14}$$

where $\theta^k(x,y,z)$ is the relative temperature distribution in a generic k layer referred to a reference temperature θ_e. The virtual variation of the strain energy is

$$\sum_{k=1}^{N_l} \int_{\Omega_k} \int_{A_k} \left(\delta\boldsymbol{\epsilon}_p^{k^T} \boldsymbol{\sigma}_p^k + \delta\boldsymbol{\epsilon}_n^{k^T} \boldsymbol{\sigma}_n^k \right) dz_k\, d\Omega_k \tag{15}$$

where stresses $\boldsymbol{\sigma}_p$ and $\boldsymbol{\sigma}_n$ are considered as the sum of the mechanical (H) and thermal (T) contributions,

$$\begin{array}{l} \boldsymbol{\sigma}_p = \boldsymbol{\sigma}_{pH}^k - \boldsymbol{\sigma}_{pT}^k \\ \boldsymbol{\sigma}_n = \boldsymbol{\sigma}_{nH}^k - \boldsymbol{\sigma}_{nT}^k \end{array} \tag{16}$$

The constitutive equations for piezoelectric materials are

$$\begin{array}{l} \boldsymbol{\sigma}^k = \mathbf{C}^k\boldsymbol{\epsilon}^k - \mathbf{e}^{k^T}\mathbf{E}^k \\ \tilde{\mathbf{D}}^k = \mathbf{e}^k\boldsymbol{\epsilon}^k + \boldsymbol{\varepsilon}^k\mathbf{E}^k \end{array} \tag{17}$$

where $\tilde{\mathbf{D}}^k$ is the dielectric displacement and $\mathbf{E}^k$ is the electric field. $\mathbf{e}^k$ is the matrix of the piezoelectric constants,

$$\mathbf{e}^k = \begin{bmatrix} 0 & 0 & 0 & e_{14}^k & e_{15}^k & 0 \\ 0 & 0 & 0 & e_{24}^k & e_{25}^k & 0 \\ e_{31}^k & e_{32}^k & e_{36}^k & 0 & 0 & e_{33}^k \end{bmatrix} \tag{18}$$

and $\boldsymbol{\varepsilon}^k$ is the matrix of the permittivity coefficients of the k-layer,

$$\boldsymbol{\varepsilon}^k = \begin{bmatrix} \varepsilon_{11}^k & \varepsilon_{12}^k & 0 \\ \varepsilon_{21}^k & \varepsilon_{22}^k & 0 \\ 0 & 0 & \varepsilon_{33}^k \end{bmatrix} \tag{19}$$

Introducing the usual in-plane (p) and out-of-plane (n) grouping,

$$\begin{array}{l} \boldsymbol{\sigma}_p^k = \mathbf{C}_{pp}\boldsymbol{\epsilon}_{pp}^k + \mathbf{C}_{pn}\boldsymbol{\epsilon}_{pn}^k - \mathbf{e}_p^{k^T}\mathbf{E}^k \\ \\ \boldsymbol{\sigma}_n^k = \mathbf{C}_{pn}^T\boldsymbol{\epsilon}_{pp}^k + \mathbf{C}_{nn}\boldsymbol{\epsilon}_{pn}^k - \mathbf{e}_n^{k^T}\mathbf{E}^k \\ \\ \tilde{\mathbf{D}}^k = \mathbf{e}_p^k\boldsymbol{\epsilon}_p^k + \mathbf{e}_n^k\boldsymbol{\epsilon}_n^k + \boldsymbol{\varepsilon}^k\mathbf{E}^k \end{array} \tag{20}$$

The electric field $\mathbf{E}^k$ can be derived from the Maxwell equations,

$$\mathbf{E}^k = \mathbf{D}_e\Phi^k \tag{21}$$

where Φ^k is the electric potential. The virtual variation of the strain energy is

$$\sum_{k=1}^{N_L} \int_{V_k} \left(\delta\boldsymbol{\epsilon}_p^{k^T} \boldsymbol{\sigma}_p^k + \delta\boldsymbol{\epsilon}_n^{k^T} \boldsymbol{\sigma}_n^k - \delta\mathbf{E}^{k^T}\ \tilde{\mathbf{D}}^k \right) dV_k \tag{22}$$

The governing equations are obtained substituting the geometrical relations, the constitutive equations and the variable assumptions via CUF in the variational

statements. The derivation is herein omitted for the sake of brevity; details can be found in the already mentioned CUF works and books.

The governing equations in the case of pure-mechanical analysis can be written as

$$\delta \mathbf{u}_s^{kT} \; : \; \mathbf{K}_d^{k\tau s} \mathbf{u}_\tau^k = \mathbf{P}_{d\tau}^\tau \tag{23}$$

and the boundary conditions on the edge Γ^k as

$$\delta \mathbf{u}_s^{kT} \; : \; \mathbf{u}_k^\tau = \overline{\mathbf{u}}_k^\tau \quad \text{or} \quad \mathbf{\Pi}_d^{k\tau s} \mathbf{u}_\tau^k = \mathbf{\Pi}_d^{k\tau s} \overline{\mathbf{u}}_\tau^k \tag{24}$$

where $\mathbf{P}_{d\tau}^\tau$ is the external load. The fundamental nucleus of the stiffness matrix, $\mathbf{K}_d^{\tau s}$, is assembled through the indexes τ and s, which consider the order of the expansion in z for the displacements. $\mathbf{\Pi}_d^{k\tau s}$ is the fundamental nucleus of the boundary conditions deriving from the integration by parts of the PVD. The explicit form of the fundamental nuclei can be found in (Carrera 2003).

The governing equations for the thermo-mechanical problem, that are

$$\delta \mathbf{u}_s^{kT} \; : \; \mathbf{K}_{uu}^{k\tau s} \mathbf{u}_\tau^k = -\mathbf{K}_{u\theta}^{k\tau s} \theta + \mathbf{p}_{us}^k \tag{25}$$

with the related boundary conditions are

$$\delta \mathbf{u}_s^{kT} \; : \; \mathbf{u}_k^\tau = \overline{\mathbf{u}}_k^\tau \quad \text{or} \quad \mathbf{\Pi}_{uu}^{k\tau s} \mathbf{u}_\tau^k = \mathbf{\Pi}_{uu}^{k\tau s} \overline{\mathbf{u}}_\tau^k \tag{26}$$

Temperature is considered an external load and it is assigned. The definition of the fundamental nuclei $\mathbf{K}_{uu}^{k\tau s}$, $\mathbf{K}_{u\theta}^{k\tau s}$ and $\mathbf{\Pi}_{uu}^{k\tau s}$ can be found in (Carrera & Brischetto 2010).

The governing equations for the electro-mechanical problem are:

$$\begin{aligned} \delta \, \mathbf{u}_k^s : \quad & \mathbf{K}_{uu}^{k\tau s} \mathbf{u}_\tau^k + \mathbf{K}_{ue}^{k\tau s} \mathbf{\Phi}_\tau^k = \mathbf{p}_{ms}^k \\ \delta \, \mathbf{\Phi}_k^s : \quad & \mathbf{K}_{eu}^{k\tau s} \mathbf{u}_\tau^k + \mathbf{K}_{ee}^{k\tau s} \mathbf{\Phi}_\tau^k = \mathbf{p}_{es}^k \end{aligned} \tag{27}$$

with the boundary conditions,

$$\begin{aligned} &\delta \, \mathbf{u}_k^s : \; \mathbf{u}_k^\tau = \overline{\mathbf{u}}_k^\tau \quad \text{or} \\ &\quad \mathbf{\Pi}_{uu}^{k\tau s} \mathbf{u}_\tau^k + \mathbf{\Pi}_{ue}^{k\tau s} \mathbf{\Phi}_\tau^k = \mathbf{\Pi}_{uu}^{k\tau s} \overline{\mathbf{u}}_\tau^k + \mathbf{\Pi}_{ue}^{k\tau s} \overline{\mathbf{\Phi}}_\tau^k \\ &\delta \, \mathbf{\Phi}_k^s : \; \mathbf{\Phi}_k^\tau = \overline{\mathbf{\Phi}}_k^\tau \quad \text{or} \\ &\quad \mathbf{\Pi}_{eu}^{k\tau s} \mathbf{u}_\tau^k + \mathbf{\Pi}_{ee}^{k\tau s} \mathbf{\Phi}_\tau^k = \mathbf{\Pi}_{eu}^{k\tau s} \overline{\mathbf{u}}_\tau^k + \mathbf{\Pi}_{ee}^{k\tau s} \overline{\mathbf{\Phi}}_\tau^k \end{aligned}$$

The definition of the fundamental nuclei $\mathbf{K}_{uu}^{k\tau s}$, $\mathbf{K}_{ue}^{k\tau s}$, $\mathbf{K}_{eu}^{k\tau s}$, $\mathbf{K}_{ee}^{k\tau s}$, $\mathbf{\Pi}_{uu}^{k\tau s}$, $\mathbf{\Pi}_{ue}^{k\tau s}$, $\mathbf{\Pi}_{eu}^{k\tau s}$ and $\mathbf{\Pi}_{ee}^{k\tau s}$ can be found in (Ballhause et al. 2005).

In the CUF, the adoption of the fundamental nucleus to assemble the problem matrices allows us set the order and the type of the expansion as an input of the analysis. In other words, the theory of structures is an input of the analysis.

Table 1. ED4 model with u_{y_3} inactive.

z^0	z^1	z^2	z^3	z^4
▲	▲	▲	▲	▲
▲	▲	△	▲	▲
▲	▲	▲	▲	▲

4 THE AXIOMATIC/ASYMPTOTIC METHOD AND BEST THEORY DIAGRAMS

In the CUF framework, the axiomatic/asymptotic method (AAM) has been recently developed to evaluate the influence of an unknown variable on a given structural problem as we vary the problem characteristics, e.g. thickness, orthotropic ratio, stacking sequence, etc. Also, the AAM leads to the definition of reduced models with a lower computational cost than full models but with the same accuracy (Carrera & Petrolo 2010, Carrera & Petrolo 2011). A typical AAM analysis consists of the following steps:

1. Parameters, such as the geometry, BC, loadings, materials and layer layouts, are fixed.
2. A starting theory is fixed (axiomatic part). That is, the displacement field is defined; usually a theory which provides 3D-like solutions is chosen and a reference solution is defined.
3. The CUF is used to generate the governing equations for the theories considered.
4. The effectiveness of each term of the adopted expansion is evaluated by measuring the error due to its deactivation.
5. The most suitable structural model for a given structural problem is then obtained discarding the non-effective displacement variables.

A graphical notation is introduced to show the results. It consists of a table with three lines, and columns equal to the number of the variables used in the expansion. For example, if an ED4 model is considered with u_{y_3} deactivated, the displacement field is

$$\begin{aligned} u_x = \; & u_{x_1} + z\, u_{x_2} + z^2\, u_{x_3} + z^3\, u_{x_4} + z^4\, u_{x_5} \\ u_y = \; & u_{y_1} + z\, u_{y_2} + \quad\; + z^3\, u_{y_4} + z^4\, u_{y_5} \\ u_z = \; & u_{z_1} + z\, u_{z_2} + z^2\, u_{z_3} + z^3\, u_{z_4} + z^4\, u_{z_5} \end{aligned} \tag{28}$$

Such a displacement field is depicted by Table 1. The use of the AAM can be extended to all the possible combinations of active/inactive variables of a given, starting theory. Each reduced model can be related to the number of the active terms and its error computed on a reference solution as reported in Fig. 1. The error values are reported on the abscissa, and the number of active terms is reported on the ordinate. Each black dot represents a reduced refined model and its position on the Cartesian plane is defined considering its error and the number of the active terms. Also, the representation of the active/non-active terms is reported for

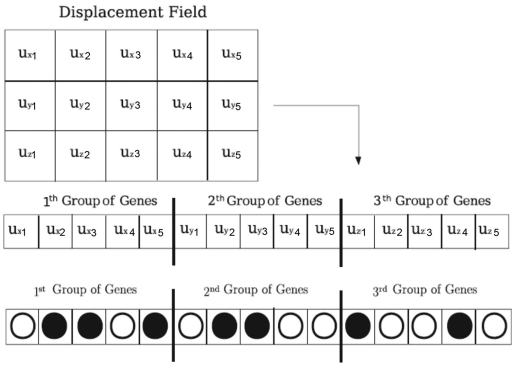

Figure 2. Generalized variables as genes in a genetic algorithm.

some reduced models. Among all the models, it is possible to note that some of them present the lowest error for a given number of active terms. These models are labeled as 1, 2, 3, 4, 5, they represent a Pareto front for the considered problems. The Pareto front is defined in this work as the Best Theory Diagram. This curve can be constructed for several problems, for example considering several types of materials, geometries and boundary conditions. Moreover, the information reported in a BTD makes it possible to evaluate the minimum number of terms, N_{min}, used to achieve a desired accuracy.

The BTD can be obtained via genetic algorithms in which each structural theory is considered an individual. The genes are the terms of the expansion, and each gene can be active or not active as in Fig. 2. Therefore, each individual is described by the number of active terms and its error computed on a reference solution. Through these two parameters, it is possible to apply the dominance rule in order to evaluate the individual fitness. For each individual copies are created according to its dominance, next, some mutations are applied to vary the set of new individuals. The purpose of this analysis is to find the individuals which belong to the Pareto front, that is the subset of individuals not dominated by the others.

5 RESULTS

First, a simply-supported multilayered plate is considered under a transverse pressure distribution, a temperature distribution and an electric potential distribution, separately. For the mechanical case, the pressure distribution is

$$p_z = p_z^0 \sin\left(\frac{m\,\pi}{a}\,x\right) \sin\left(\frac{n\,\pi}{b}\,y\right) \tag{29}$$

where m and n are equal to 1, the pressure distribution is applied to the top surface of the plate, and $a = b = 1$. For the thermal case, temperature distribution defined as in

$$\theta_\tau^k = \hat{\theta}_\tau^k \sin\left(\frac{m\pi x_k}{a_k}\right) \sin\left(\frac{n\pi y_k}{b_k}\right) \tag{30}$$

and Eq. (8), with (t_{top}, t_{bot}) equal to 1 and -1, respectively. For the piezoelectric case, two different configurations are considered, the sensor and actuator configurations. In the sensor case, a transverse pressure is applied to the top surface of the plate and the potential distribution is evaluated. The potential at the top and bottom is set to zero. In the actuator case, a potential distribution is applied to the plate, and the value of the potential is set to 1 V at the top and to 0 V at the bottom. In the sensor case, the pressure is assumed as in Eq. (29), while, in the actuator case, the potential distribution is assumed as

$$\Phi = \overline{\Phi} \sin\left(\frac{m\,\pi}{a}\,x\right) \sin\left(\frac{n\,\pi}{b}\,y\right) \tag{31}$$

where $m = n = 1$ and $\overline{\Phi}$ is set equal to 1. The material properties for the mechanical and thermal cases are $E_L/E_T = 25$, $G_{LT}/E_T = G_{TT}/E_T = 0.5$, $G_{Lz}/E_T = 0.2$, $\nu = 0.25$ and $\alpha_L/\alpha_T = 1125$, where E is the Young's modulus, G the shear modulus, ν the Poisson's ratio and α the coefficient of thermal expansion. Symbols L and T denote the directions parallel and transverse to the composite fibers, respectively. For the piezoelectric case, the material properties of the laminated layers are: $E_1 = 132.38 \times 10^9$ Pa, $E_2 = E_3 = 10.756 \times 10^9$ Pa, $G_{12} = G_{13} = 5.6537 \times 10^9$ Pa, $G_{23} = 3.606 \times 10^9$ Pa, $\nu_{12} = \nu_{13} = 0.24$, $\nu_{23} = 0.49$, $\varepsilon_{11} = 3.098966 \times 10^{-11}$ C/Vm, $\varepsilon_{22} = \varepsilon_{33} = 2.6562563 \times 10^{-11}$ C/Vm. The thickness of each layer is equal to $h = 0.4 \cdot h_{\text{TOT}}$. The piezoelectric layers are made of PZT-4, their properties are $E_1 = E_2 = 81.3 \times 10^9$ Pa, $E_3 = 64.5 \times 10^9$ Pa, $\nu_{12} = 0.329$, $\nu_{13} = \nu_{23} = 0.432$, $G_{44} = G_{55} = 25.6 \times 10^9$ Pa, $G_{66} = 30.6 \times 10^9$ Pa, $e_{31} = e_{32} = -5.20$ C/m^2, $e_{33} = 15.08$ C/m^2, $e_{24} = e_{15} = 12.72$ C/m^2, $\varepsilon_{11}/\varepsilon_0 = \varepsilon_{22}/\varepsilon_0 = 1475$, $\varepsilon_{33}/\varepsilon_0 = 1300$ ($\varepsilon_0 = 8.854 \times 10^{-12}$ C/Vm). The thickness of each layer is equal to $h = 0.1 \cdot h_{\text{TOT}}$. The BTDs reported in this work are based on the solution computed using the LD4 model. In fact, the LD4 proved to agree excellently with the elastic solutions (Carrera 2003, Carrera 2002, Ballhause et al. 2005).

The ESL approach is considered, and the BTDs for the ED4 model are given in Figs. 3 and 4 for the thin and thick geometry, respectively. The results suggest that the reduced refined models for the piezoelectric case show a higher computational cost than the reduced models for the mechanical and thermal cases, since the variables of the electric potential are retained. Models located on the BTD for both thermal and mechanical cases detect the same accuracy when a thin plate is considered, while the BTDs for the piezoelectric case present a significant difference between the sensor and actuator configuration. Since the reference solution is obtained with an LD4 model,

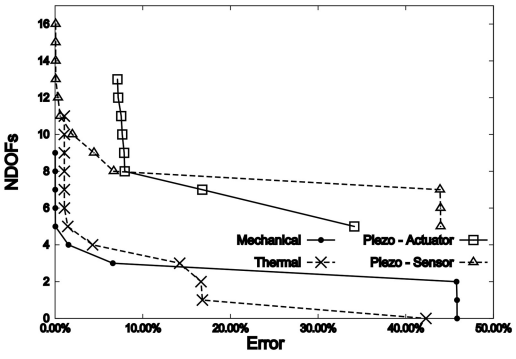

Figure 3. BTDs for $a/h = 100$.

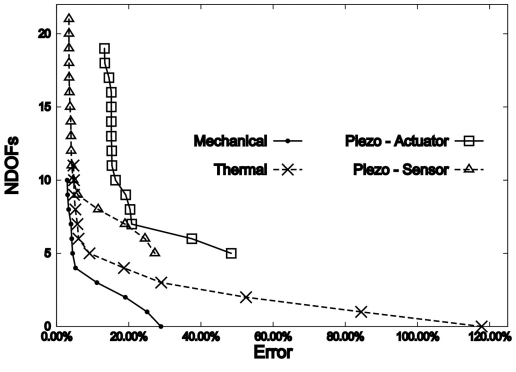

Figure 4. BTDs for $a/h = 4$.

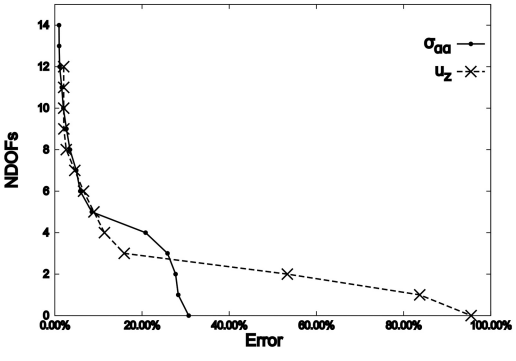

Figure 5. BTD for the asymmetric composite shells, $R_\beta/h = 4$.

the minimum errors are larger than zero. In fact, the LD4 offers a better accuracy than ED4.

Next, a composite shell is considered under a pure mechanical load, see Eq. 29. The material properties are $E_L/E_T = 25$, $\nu = 0.25$, $G_{LT}/E_T = G_{TT}/E_T = 0.5$, $G_{Lz}/E_T = 0.2$ and the dimensions of the shell are $a = 4R_\beta$ and $b = 2\pi R_\beta$. A $0°/90°$ stacking sequence was considered. Figure 5 shows the BTD for stress and displacement components. Significant differences in the BTD for different outputs are observable. Table 2 shows some of the BTD models. In this case, the FSDT is a BTD.

Table 2. BTDs for the asymmetric composite shell, $\sigma_{\alpha\alpha}$

$R_\beta/h = 100$	
$M_e/M = 9/15$	
▲ ▲ △ △ △	
▲ ▲ ▲ ▲ △	
▲ ▲ ▲ △ △	
Error	$2.6671\,\%$
$M_e/M = 5/15$	
▲ ▲ △ △ △	
▲ ▲ △ △ △	
▲ △ △ △ △	
Error	$8.4968\,\%$

6 CONCLUSIONS

This paper presents the latest advances in the framework of the Carrera Unified Formulation (CUF). In particular, multifield problems for multilayered plates and shells have been addressed. The CUF is an established formulation to develop refined structural models via expansion functions. The order and the type of the expansions are free parameters of the analysis. In particular, Equivalent Single Layer (ESL) and Layer-Wise (LW) approaches can be handled straightforwardly.

In this work, a brief overview of the Axiomatic/Asymptotic Method (AAM) has been given. The AAM has been recently developed in the CUF framework and has two main capabilities,

- A starting structural model is set, and the influence of each unknown variable on a given structural problem is quantified as the problem characteristics vary (e.g. thickness, orthotropic ratio, stacking sequence, etc.). In other words, starting from an axiomatic approach, asymptotic-like results can be obtained.
- Retrieving only the terms affecting the solution, reduced models are built as accurate as the full models but computationally more efficient.

The systematic use of the AAM has led to the introduction of the Best Theory Diagram (BTD). A 'best theory' is the one that, given a number of unknown variables, provides the best accuracy or, for a given accuracy, results in the minimum number of unknown variables. In the BTD, all the best structural models can be read. The BTD can be considered as the Pareto Front of an optimization problem and provides guidelines to develop structural models. In fact, the BTD provides the boundary of the trade-off between accuracy and computational costs. In other words, accuracy cannot be increased and computational cost lowered better than the BTD.

The results show that the combined use of CUF and AAM provides insights related to the decision making in structural model choices and developments.

In particular, the reduced models greatly increase the computational efficiency in the LW case. Also, the use of genetic algorithms to obtain the BTD is a powerful strategy to obtain structural guidelines for any problem.

REFERENCES

Argyris, J. & Tenek, L. (1997). Recent advances in computational thermostructural analysis of composite plates and shells with strong nonlinearities. *Applied Mechanics Reviews 50*(5), 285–306.

Ballhause, D., D'Ottavio, M., Kroplin, B. & E. Carrera (2005). A unified formulation to assess multilayered theories for piezoelectric plates. *Computer & Structures 83*, 1217–1235.

Carrera, E. (2002). Temperature profile influence on layered plates response considering classical and advanced theories. *AIAA Journal 40*(9), 1885–1896.

Carrera, E. (2003). Theories and finite elements for multilayered plates and shells: A unified compact formulation with numerical assessment and benchmarking. *Archives of Computational Methods in Engineering 10*(3), 215–296.

Carrera, E. & Brischetto, S. (2010). Coupled thermomechanical analysis of one-layered and multilayered plates. *Composite Structures 92*(1–2).

Carrera, E., Brischetto, S. & Nali, P. (2011). *Plates and Shells for Smart Structures: Classical and Advanced Theories for Modeling and Analysis*. John Wiley & Sons.

Carrera, E., Cinefra, M., Lamberti, A. & Zenkour, A. (2015). Axiomatic/asymptotic evaluation of refined plate models for thermomechanical analysis. *Journal of Thermal Stress 38*, 165–187. doi: 10.1080/01495739.2014.976141.

Carrera, E., Cinefra, M., Petrolo, M. & Zappino, E. (2014). *Finite Element Analysis of Structures through Unified Formulation*. John Wiley & Sons.

Carrera, E. & Petrolo, M. (2010). Guidelines and recommendation to contruct theories for metallic and composite plates. *AIAA Journal 48*(12), 2852–2866. doi: 10.2514/1.J050316.

Carrera, E. & Petrolo, M. (2011). On the effectiveness of higher-order terms in refined beam theories. *Journal of Applied Mechanics 78*. doi: 10.1115/1.4002207.

Cinefra, M., Carrera, E., Lamberti, A. & Petrolo, M. (2017). Best theory diagrams for multilayered plates considering multifield analysis. *Journal of Intelligent Material Systems and Structures* First published doi: 10.1177/1045389X16679018.

Cinefra, M., Lamberti, A., Zenkour, A. & Carrera, E. (2015). Axiomatic/asymptotic technique applied to refined theories for piezoelectric plates. *Mechanics of Advanced Materials and Structures 22*(1–2), 107–124. doi: 10.1080/15376494.2014.908043.

Hetnarski, R. B. & Eslami, M. R. (2009). *Thermal Stresses – Advanced Theory and Applications*. Springer.

Hildebrand, F. B., Reissner, E. & Thomas, G. B. (1938). Notes in the foundations of the theory of small displacement of orthotropic shells. Technical report, NASA.

Kirchhoff, G. (1850). Uber das gleichgewicht und die bewegung einer elastischen scheibe. *Journal fur reins und angewandte Mathematik 40*, 51–88.

Lekhnitskii, G. S. (1968). *Anisotropic Plates*. Gordon and Breach Science Publishers.

Love, A. E. H. (1927). *The Mathematical Theory of Elasticity*. Cambridge University Press.

Mindlin, R. (1972). High frequency vibrations of piezoelectric crystal plates. *International Journal of Solids and Structures 8*, 895–906.

Mindlin, R. D. (1951). Influence of rotatory inertia and shear in flexural motions of isotropic elastic plates. *Journal of Applied Mechanics 18*, 1031–1036.

Mitchell, J. & Reddy, J. N. (1995). A refined hybrid plate theory for composite laminates with piezoelectric laminae. *International Journal of Solids and Structures 32*(16), 2345–2367.

Murakami, H. (1993). Assessment of plate theories for treating the thermomechanical response of layered plates. *Composites Engineering 3*(2), 137–149.

Noor, A. K. & Burton, W. S. (1992). Computational models for high-temperature multilayered composite plates and shells. *Applied Mechanics Reviews 12*(10), 419–446.

Reddy, J. N. (1997). *Mechanics of Laminated Plates, Theory and Analysis*. CRC Press.

Reissner, E. (1945). The effect of transverse shear deformation on the bending of elastic plates. *Journal of Applied Mechanics 12*, 69–76.

Tauchert, T. R. (1991). Thermally induced flexure, buckling, and vibration of plates. *Applied Mechanics Reviews 44*(8), 347–360.

Tiersten, H. F. (1969). *Linear Piezoelectric Plate Vibrations*. Plenum Press.

Vlasov, B. F. (1957). On the equations of bending of plates. *Doklady Akademii Nauk Azerbaidzhanskoi SSR 3*, 955–979.

Yang, J. & Yu, J. (1993). Equations for a laminated piezoelectric plate. *Archives of Mechanics 45*, 653–664.

Taylor & Francis
Taylor & Francis Group
http://taylorandfrancis.com

Shell Structures: Theory and Applications Volume 4 – Pietraszkiewicz & Witkowski (eds)
© 2018 Taylor & Francis Group, London, ISBN 978-1-138-05045-7

Micro/nanoscale assembly of three-dimensional shell/ribbon architectures by compressive buckling

H. Fu & Y. Zhang
Center for Mechanics and Materials, AML, Department of Engineering Mechanics, Tsinghua University, Beijing, China

ABSTRACT: Assembly of three-dimensional (3D) mesostructures in advanced materials opens up many new application opportunities across a broad range of areas. Mechanically-guided assembly that replies on controlled, compressive buckling of 2D precursors represents an emerging method of great promise, due to the versatile applicability, not only to a diverse set of materials (from soft polymer to plastic metal and brittle inorganic semiconductors), but to a broad range of length scales (from submicrometer to centimeter dimensions). This paper presents a short review on various key aspects of this approach, including the basic principle, mechanics-inspired design concepts, and theoretical modeling of the assembly process. In particular, the kirigami/origami inspired designs, releasable multi-layer designs, and engineered substrate designs, are discussed in detail.

1 INTRODUCTION

Three-dimensional micro/nano-structures are of increasing interest, owing to their widespread applications in a variety of areas, from biomedical sensing devices (Feiner et al., 2016, Leong et al., 2009, Sidorenko et al., 2007, Tian et al., 2012), to microelectromechanical components (Zhu & Chang, 2015), to energy storage systems (Yoo et al., 2015, Song et al., 2014, Wu et al., 2013, Zhang et al., 2011), to metamaterials (Schaedler et al., 2011, Valentine et al., 2008, Zheng et al., 2014), to electronics (Ahn et al., 2009, Huang et al., 2012, Xu et al., 2015) and to photonics and optoelectronics (Braun, 2014, Fan et al., 2009, Lee et al., 2014). Various fabrication approaches were developed to form complex 3D structures at different scales, such as those based on 3D printing/writing (Gratson et al., 2004, Lewis et al., 2006, Lewis, 2006, Ladd et al., 2013a), templated growth (Klein et al., 2007, Kim et al., 2012, Zhu & Li, 2014, Zhu & Li, 2013) and fluidic self-assembly (Zheng & Jacobs, 2005, Crane et al., 2013). However, these approaches are typically incompatible with the established planar device technologies such as lithographic techniques, and generally cannot be used directly with many advanced materials (e.g., device-grade inorganic semiconductors like silicon and GaAs) (Lewis et al., 2006, Lewis, 2006, Ladd et al., 2013b, Gratson et al., 2004, Fischer & Wegener, 2013, Arpin et al., 2010). Other approaches that rely on origami-inspired reconfigurable design (Na et al., 2015, Filipov et al., 2016, Xia et al., 2016, Filipov et al., 2015), thin-film residual stresses (Schmidt & Eberl, 2001, Pandey et al., 2013, Xu et al., 2009, Li, 2008, Huang et al., 2012, Wei et al., 2014, Schmidt et al., 2002) and capillary forces (Li et al., 2010, Py et al., 2007, Guo et al., 2009), avoid some of these limitations and hold great potential in microelectronics applications. However, these approaches can only provide access to limited class of geometries such as polyhedrons, tubes and variants of these; and the latter two are, in most cases, irreversible and have limited control over critical parameters such as the folding angle (Arora et al., 2006, Randhawa et al., 2008, Leong et al., 2009, Pandey et al., 2011, Li, 2011, Huang et al., 2011, Bishop et al., 2012).

Recently, a conceptually different approach that exploits controlled, compressive buckling was developed to achieve deterministic assembly of 3D mesostructures from patterned 2D films (Yan et al., 2016a, Yan et al., 2016b, Xu et al., 2015, Nan et al., 2016, Zhang et al., 2015, Shi et al., 2017). Here, thin 2D precursors are fabricated by well-established techniques of semiconductor processing, followed by selective bonding onto a prestretched elastomer at lithographically defined locations. Release of the prestrain in the elastomer provides compressive forces that induce 2D-3D transformation of precursors, in terms of spatial translations/rotations and bending/twisting deformations (Figure 1). Due to the elastic nature of the assembly scheme, the resulting 3D configurations can be controlled actively, in a continuous and reversible manner. This mechanically-guided assembly method applies to a broad set of materials from soft polymer to brittle inorganic semiconductors, over length scales from submicrometer to centimeter dimensions. Moreover, it is compatible with the state-of-art planar technologies, and is capable of forming multiple 3D structures in parallel, thereby providing

an efficient route to developments of functional 3D devices, such as tunable optical transmission window (Zhang et al., 2015), microconcave mirror (Nan et al., 2016), tunable inductor (Xu et al., 2015) and 3D NFC device (Yan et al., 2016a). In addition, the 3D mesostructures can serve as vibrational platforms with tunable resonant frequencies and improved bandwidth, which hold potentials for application in 3D MEMS (Ning et al., 2017).

This review summarizes a set of design concepts for this mechanically-guided 3D assembly, to provide access to four representative classes of topologies, including open-mesh, filamentary networks (Xu et al., 2015), kirigami-inspired membrane architectures (Zhang et al., 2015), origami-inspired folding structures (Yan et al., 2016b), and dense, multilayer frameworks (Yan et al., 2016a). Quantitative mechanics modeling serves as a tool to guide the selections of 2D precursors and prestrains to form desired 3D geometries. For a certain class of 2D precursors with representative serpentine layout, an analytical model (Liu et al., 2016) is discussed, which reveals the underlying relations between the 3D configurations and fabrication parameters.

2 DESIGN CONCEPTS FOR MECHANICALLY-GUIDED 3D ASSEMBLY

2.1 *Assembly of open-mesh, filamentary networks*

To form open-mesh, filamentary networks through this assembly scheme, the 2D precursors are usually composed of a collection of ribbons with large width to thickness ratio (w/t). As such, the out-of-plane bending stiffness ($\propto wt^3$) is much smaller than the in-plane value ($\propto w^3t$). Upon release of prestrain in the substrate, lateral buckling occurs in the 2D precursors to reduce the strain energy. In specific, the non-bonded regions undergo coordinated translational and rotational motions as well as bending/twisting deformations, leading to the formation of open-mesh, filamentary networks (Xu et al., 2015) (Figure 1). Figure 2a and 2b shows two representative examples dominated by bending and twisting deformations, respectively. This idea can also be extended to build multi-level constructions through multiple, hierarchical levels of buckling. An example appears in Figure 2c. Here, three ribbons at the center connect the precursor structures at regions where the assembly process would otherwise yield the maximum out-of-plane displacements. During the 2D-3D transformation, these ribbons undergo an additional level of buckling to form elevated "second floor" and "third floor" suspended above the reach of buckling that represents the "first floor". In all of these examples, the finite element analyses (FEA) give accurate predictions of the final 3D geometries, as evidenced by the remarkable agreement with the experiments. In addition, FEA can be adopted in the optimization of layouts of 2D precursors to keep the maximum material strains below the fracture threshold.

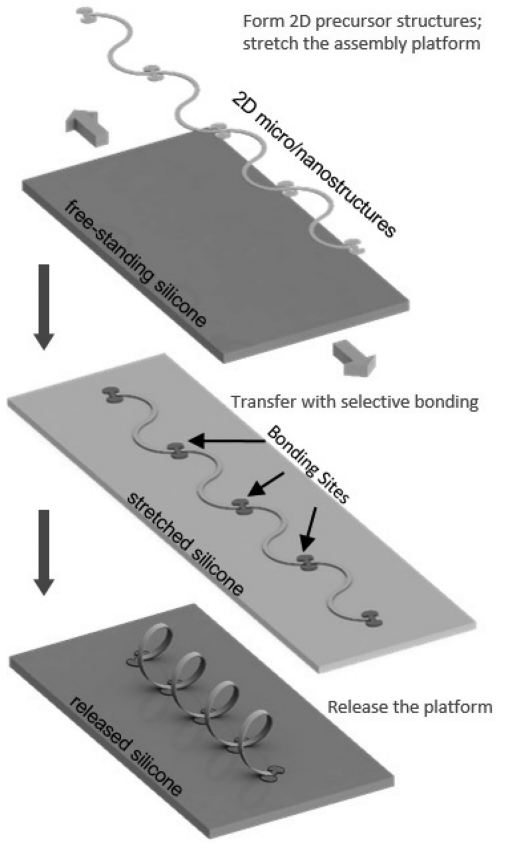

Figure 1. Schematic illustration of the mechanically-guided 3D assembly process. From the top to the bottom: forming 2D micro/nanostructures using lithographic and etching techniques, transferring these structures to a stretched silicone elastomer with bonding at selected sites, and releasing the elastomer to form 3D mesostructures. Adapted with permission from Reference (Yan et al., 2017), Copyright 2017, Elsevier.

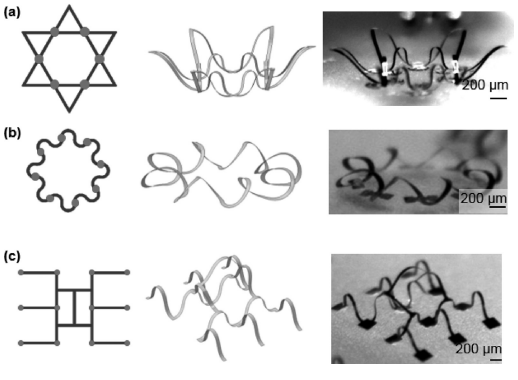

Figure 2. 2D precursors, FEA predictions, and optical micrographs for (a) two-layer flower, (b) circular helix, and (c) triple-level 3D mesostructure. Adapted with permission from Reference (Xu et al., 2015), Copyright 2015, American Association for the Advancement of Science.

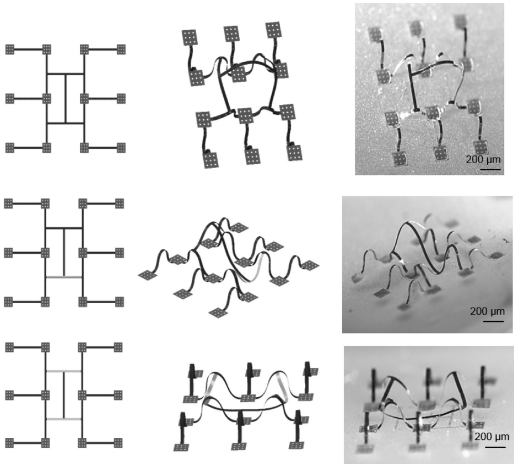

Figure 3. 2D precursors, FEA predictions and optical images for triple-floor structures made of SiNx and bilayers of gold and polymer (SU8). Adapted with permission from Reference (Fu et al., 2017), Copyright 2017, Wiley.

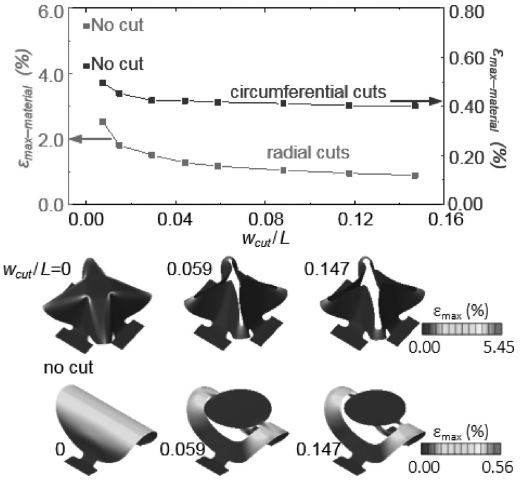

Figure 4. Maximum material strain as a function of the dimensionless widths of cuts in membranes with $t/L = 0.0011$ and $l_{cut}/L = 1.68$ (for circumferential cuts) or 0.76 (for radial cuts), under a compressive strain of 50%, and the associated strain distributions. Reproduced with permission from Reference (Zhang et al., 2015), Copyright 2015, National Academy of Sciences.

The above design concept can be combined with the residual-stress strategy to broaden the accessible range of 3D geometries. By fabricating a thin film (e.g., SiNx layer) with well-defined residual stress (Yu et al., 2015, Froeter et al., 2013), and adhering it to the 2D precursor at strategically designed regions, higher order buckling mode can be achieved upon release of elastomer. Here, the stress-controlling layers serve as an external perturbation to select desired buckling modes whose strain energies are comparable to that of the first-order mode. Figure 3 presents FEA predictions and experimental results for three complex mesostructures in SU8 (blue), which have similar 2D presursors with that in Figure 1c, but incorporates SiNx layer (indigo) in some local regions. With the addition of these SiNx layers, the central ribbon can either deform in an asymmetric manner (Figure 3, middle) or pop down (Figure 3, bottom), different from the original mode (Figure 3, top). In addition to mode selection, the stress-controlling layer also can eliminate near degeneracies that sometimes occur between the lowest order mode and other modes of complex 3D configurations, thereby enhancing the yields in realizing targeted outcomes.

2.2 *Assembly of kirigami-inspired membrane architectures*

Different from the filamentary structures, membranes are more likely to suffer from mechanical failure in local region during the compressive buckling. Specifically, 2D precursors without carefully placed cuts tend to undergo sharp, localized, 'kink' deformations, due to the lateral constraints imposed by the strong bonding regions. The resulting stress concentration can potentially lead to fracture of the constituent materials. To eliminate this type of localized deformations, the kirigami-inspired concepts were introduced, which involves precisely engineered cuts to guide the deformations during assembly (Zhang et al., 2015). Figure 4 depicts the maximum strain level across two representative membrane structures with different ratios (w_{cut}/L) of cut width to overall dimension, under a compressive strain of 50%. Here, the introduction of cuts can dramatically relieve the strain concentrations, as shown by the reduced maximum strain with increasing w_{cut}/L. This figure also suggests that the locations and patterns of cuts play critical roles in decreasing the local strain.

In addition to strain reduction as discussed above, the kirigami-inspired concepts afford great versatility in the design of 3D structures. Figure 5 demonstrates a series of 3D nanomembrane structures formed with silicon (300 nm)/polyimide (PI, 300 nm) bilayers, where the differences arise only from the locations and patterns of cuts. Such capabilities in diversifying the variety of 3D membrane geometries broaden the range of applications for this mechanically-guided 3D assembly.

2.3 *Assembly of origami-inspired folding structures*

During the process of compressive buckling, both the filamentary networks and kirigami-inspired membrane architectures undergo relative continuous and global deformations in terms of bending and/or twisting. However, these layouts do not allow well-controlled, localized folding deformations that are essential to the notion of origami. As a solution, a strategy relying on a spatial variation of thickness in

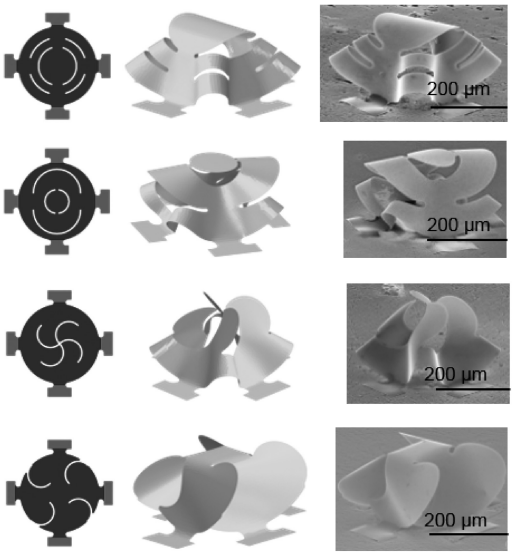

Figure 5. 2D precursors, FEA predictions, and SEM images for four 3D membrane mesostructures. Adapted with permission from Reference (Zhang et al., 2015), Copyright 2015, National Academy of Sciences.

the 2D precursor (Yan et al., 2016b) was proposed. This concept is illustrated using a straight ribbon with engineered creases as an example, as shown in Figure 6a–6c. This ribbon (length L, excluding the bonding locations) consists of five segments (Figure 6a), two (with length L_1 and thickness t_1) of which are thicker than the other three (with length L_2 and thickness t_2). As the thickness ratio (t_2/t_1) decreases (e.g., $<1/3$), the radius of curvature in the thin segments decreases. The deformations of thick segments are negligible, due to its bending stiffness that is much larger than that of creases. The thin segments also tend to accommodate the compression via folding for relatively small length ratios (L_2/L) (e.g., <0.1). These results indicate that both small thickness ratio ($t_2/t_1 < 1/3$) and small length ratio ($L_2/L < 0.1$) are essential for creating sharp creases at the thinner segments.

As most of the deformations are localized at the creases in the buckling process, it is of importance to predict the strain level in the creases to avoid mechanical failure. A scaling law for the maximum strain (ε_m) is established as $\varepsilon_m = F(\varepsilon_{pre})t_2/L_2$, in which ε_{pre} is the prestrain and $F(\varepsilon_{pre})$ denotes a function that can be determined from FEA. According to this scaling law, reductions in the crease thickness (t_2) and increases in the crease length (L_2) can well reduce the maximum strains.

Figure 6d provides a representative origami mesostructure achieved with this strategy. It consists of a hollow square (bilayer of silicon/SU8), with creases (grey) located radially. After releasing the prestrain in the elastomer, a windmill structure

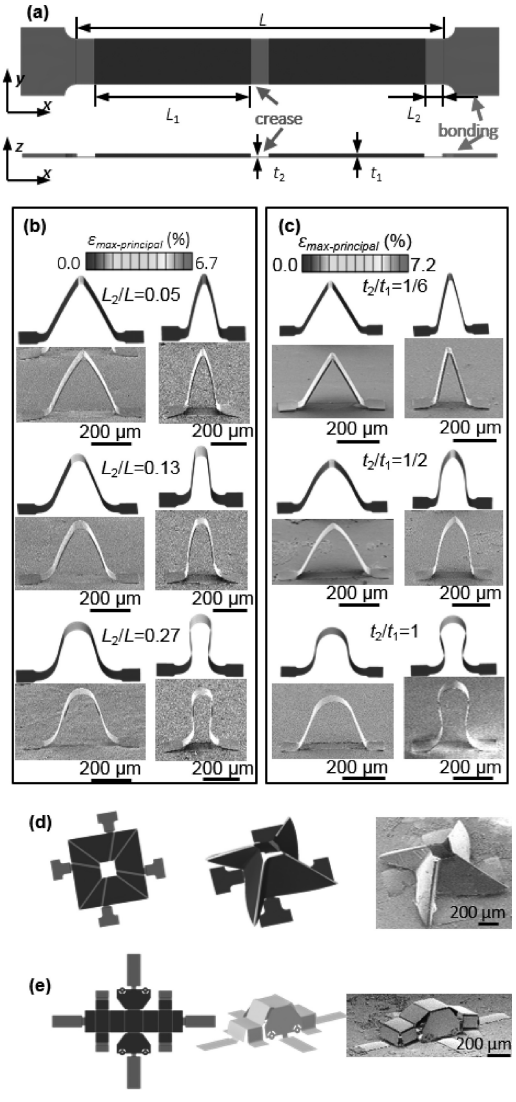

Figure 6. Top and cross-sectional views of a straight ribbon with two different thicknesses (a); and FEA results and corresponding SEM images of deformed mesostructures under two different levels (60% and 160%) of prestrain, for the non-uniform ribbons with (b) fixed thickness ratio ($t_2/t_1 = 1/4$) and three different length ratios (L_2/L), or with (c) fixed length ratio ($L_2/L = 0.05$) and three different thickness ratios (t_2/t_1). 2D precursors, FEA predictions, and SEM images of Origami assembly of 3D mesostructures from corresponding 2D membranes. (d) a windmill mesostructure and (e) a car mesostructure formed with biaxial prestrain. Adapted with permission from Reference (Yan et al., 2016b), Copyright 2016, Wiley.

is formed. This design concept can be extended to achieve 3D structures with hierarchical forms of folding. Figure 6e shows a complex mesostructure (bilayer of gold/SU8) that resembles a car, with carefully selected non-equal biaxial prestrains ($\varepsilon_{x\text{-}pre} = 33\%$ and

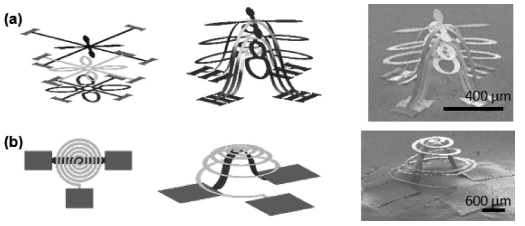

Figure 7. Multilayer 2D precursors, FEA predictions, and SEM images of the assembled 3D structure formed with the use of biaxial prestrain in the substrate. (a) a tree mesostructure; (b) a spire mesostructure. Adapted with permission from Reference (Yan et al., 2016a), Copyright 2016, American Association for the Advancement of Science.

$\varepsilon_{\text{y-pre}} = 53\%$). FEA predictions agree well with the SEM images for both of the examples.

2.4 *Assembly of dense, multilayer frameworks*

The mesostructures described in the previous sections result from 3D transformation of single-layer 2D precursor. The intrinsic nature of the buckling processes (for example, proportional dependence of maximum strain on precursor thickness) in these cases sets limitations to the range of realizable 3D mesostructures, primarily in the form of open-layout geometries with largely hollow interior regions. The strategy through use of releasable, multilayered 2D precursors provides a solution (Yan et al., 2016a). In addition, this strategy enables formation of 3D mesostructures with geometries inaccessible previously, such as those with local force actuators and structural support.

In this approach, 2D precursors with different shapes and materials are transfer printed onto the substrate in a layer-by-layer fashion, with selective bonding sites in the underlying layers or in the substrate. The resulting multilayered 2D presursor enables the formation of 3D overlapping, nested mesostructures by compressive buckling. Figure 7a shows a representative example in SU8 that resembles a tree. Here, each layer assembles independently, without mechanical interactions with other layers. Tailored interactions between multiple layers are also possible with appropriate designs. Figure 7b presents a spire-shaped 3D bilayer mesostructure in polyimide (PI). Here, the bottom-layer ribbon buckles upon compression, which drives the transformation of the top-layer coil into 3D spires.

2.5 *Assembly of 3D structures with engineered substrate*

The aforementioned design concepts focus on the 2D precursors, while the assembly platform can provide only spatially uniform compression. By exploiting an elastomer substrate with engineered variations in the thickness (Nan et al., 2016), a spatially non-uniform compression can be achieved in a precise manner. With this design, the stretching uniformly applied to

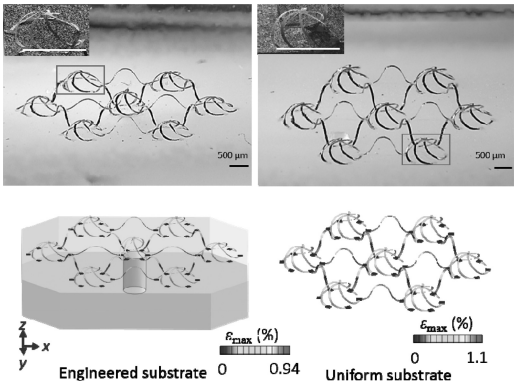

Figure 8. Optical images of 3D structures (top), and corresponding FEA results, including illustrations of the substrate geometries (bottom; only the central part of substrate is shown). The insets show magnified SEM views of the regions identified with red boxes in each optical image. Experimental and FEA results of 3D structures formed using the same 2D precursors but with uniform substrates are on the right. Reproduced with permission from Reference (Nan et al., 2016), Copyright 2016, Wiley.

the edges of the substrate lead to spatial patterns of strain that correlate to the variations in thickness, with larger strains in thinner regions. Upon release of the prestrain, the compressive forces vary spatially in a corresponding manner, thereby leading to the formation of non-uniform 3D structures.

To provide a precise control over the compressive forces, a detailed numerical model is built for the uniaxially stretched engineered substrate. Based on the parametric study of three key parameters (i.e., applied strain, thickness ratio ($t_{\max}/t_{\min}$) and the geometry of the thickness variation), an inverse design approach is established to allow selection of profiles in thickness to offer desired strain distributions for different stretching levels. In this approach, an initial trial solution is determined by assuming a constant tangent modulus, where the thickness distribution is roughly inversely proportional to the target strain distribution. FEA then takes into account the local strain levels to refine the substrate geometry, which serves as an input to the model to update the strain-dependent tangent modulus.

Repeated iteration of this process yields an optimized substrate geometry that renders the desired strain profile. This idea can also be extended to the biaxially stretched substrate, and the experiment results of strain distribution agree well with the FEA predictions. This design concept enables both the gradual and dramatic geometrical changes in mechanically-guided 3D mesostructures. Figure 8 shows an array of radially oriented ribbons in gold (40 nm)/SU8 (7 μm) bilayers, formed by engineered substrate and uniform substrate, respectively. In this mesostructure, the central unit is subject to larger deformations than the surrounding counterparts, due to the presence of an aligned hole (diameter = 1.2 mm) through the substrates. In this case, the hole region

(e.g., zero thickness) has zero stiffness, leading to large radial and circumferential deformations upon uniform biaxial stretching.

3 THEORETICAL MODELING FOR MECHANICALLY-GUIDED FORMATION OF 3D HELICAL MESOSTRUCTURES

Due to the complicated deformation mechanisms, it is very challenging to develop analytic models that predict accurately the process of mechanically-guided assembly for complex 2D precursors (Fan et al., 2017). Partly as a result, the underlying relations between the 3D configurations, fracture-induced failure, and fabrication related parameters (e.g., prestrain level, the geometric parameters of 2D precursors) remain unclear. To present a systematic investigation of buckling behavior in 3D mesostructure, an analytic model of compressive buckling was formulated for simple 2D precursors in serpentine layouts (Liu et al., 2016). This study sheds light on scaling laws for general 3D filamentary structures.

In this model, the displacements and the twist angle of resulting helical mesostructures are characterized by a set of functions with dimensionless parameters, carefully selected to fit the boundary conditions. These dimensionless parameters are determined based on the minimization of total energy. As a result, analytic solutions are obtained for the key physical quantities, including displacement, curvature and maximum strain. According to the analytic solutions, the maximum strain has a square root dependence on the applied strain, and a proportional dependence on the normalized thickness (t/R), where R is the radius of the arc in 2D precursor. These analytic solutions exhibit reasonable agreement with the FEA and experiments, thereby providing guidelines for choosing various design parameters to avoid the brittle fracture or plastic yield during the assembly process.

4 SUMMARY

Developments in the mechanics and materials strategies described above establish the mechanically-guided assembly through compressive buckling as a promising route to 3D mesostructures in advanced materials. An intriguing feature is its versatile applicability, not only to a wide range of length scales, but to a broad set of material classes. As such, many new applications are possible with this assembly approach, as demonstrated in the developments of tunable electromagnetic components and new biomedical devices. Many opportunities still exist in this young area. For example, developments of finite-deformation models with appropriate assumptions to enable predictions of buckling process are needed for an efficient 3D design. Extension of the current scheme to assembly of 3D structures with lateral sizes in the nanoscale regime also represents a promising direction to explore.

REFERENCES

Ahn, B. Y., Duoss, E. B., Motala, M. J., Guo, X., Park, S.-I., Xiong, Y., Yoon, J., Nuzzo, R. G., Rogers, J. A. & Lewis, J. A. (2009) Omnidirectional Printing of Flexible, Stretchable, and Spanning Silver Microelectrodes. *Science*, 323, 1590–1593.

Arora, W. J., Nichol, A. J., Smith, H. I. & Barbastathis, G. (2006) Membrane folding to achieve three-dimensional nanostructures: Nanopatterned silicon nitride folded with stressed chromium hinges. *Applied Physics Letters*, 88, 053108.

Arpin, K. A., Mihi, A., Johnson, H. T., Baca, A. J., Rogers, J. A., Lewis, J. A. & Braun, P. V. (2010) Multidimensional Architectures for Functional Optical Devices. *Advanced Materials*, 22, 1084–1101.

Bishop, D., Pardo, F., Bolle, C., Giles, R. & Aksyuk, V. (2012) Silicon Micro-Machines for Fun and Profit. *Journal of Low Temperature Physics*, 169, 386–399.

Braun, P. V. (2014) Materials Chemistry in 3D Templates for Functional Photonics. *Chemistry of Materials*, 26, 277–286.

Crane, N. B., Onen, O., Carballo, J., Ni, Q. & Guldiken, R. (2013) Fluidic assembly at the microscale: progress and prospects. *Microfluidics and Nanofluidics*, 14, 383–419.

Fan, Z., Razavi, H., Do, J.-W., Moriwaki, A., Ergen, O., Chueh, Y.-L., Leu, P. W., Ho, J. C., Takahashi, T., Reichertz, L. A., Neale, S., Yu, K., Wu, M., Ager, J. W. & Javey, A. (2009) Three-dimensional nanopillar-array photovoltaics on low-cost and flexible substrates. *Nature Materials*, 8, 648–653.

Fan, Z., Wu, J., Ma, Q., Liu, Y., Su, Y. & Hwang, K.-C. (2017) Post-Buckling Analysis of Curved Beams. *Journal of Applied Mechanics*, 84, 031007.

Feiner, R., Engel, L., Fleischer, S., Malki, M., Gal, I., Shapira, A., Shacham-Diamand, Y. & Dvir, T. (2016) Engineered hybrid cardiac patches with multifunctional electronics for online monitoring and regulation of tissue function. *Nature Materials*, 15, 679–685.

Filipov, E. T., Paulino, G. H. & Tachi, T. (2016) Origami tubes with reconfigurable polygonal cross-sections. *Proceedings of the Royal Society A: Mathematical, Physical and Engineering Sciences*, 472, 20150607.

Filipov, E. T., Tachi, T. & Paulino, G. H. (2015) Origami tubes assembled into stiff, yet reconfigurable structures and metamaterials. *Proceedings of the National Academy of Sciences of the United States of America*, 112, 12321–12326.

Fischer, J. & Wegener, M. (2013) Three-dimensional optical laser lithography beyond the diffraction limit. *Laser & Photonics Reviews*, 7, 22–44.

Froeter, P., Yu, X., Huang, W., Du, F., Li, M., Chun, I., Kim, S. H., Hsia, K. J., Rogers, J. A. & Li, X. (2013) 3D hierarchical architectures based on self-rolled-up silicon nitride membranes. *Nanotechnology*, 24, 475301.

Fu, H., Nan, K., Froeter, P., Huang, W., Liu, Y., Wang, Y., Wang, J., Yan, Z., Luan, H., Guo, X., Zhang, Y., Jiang, C., Li, L., Alison, C. D., Li, X., Huang, Y., Zhang, Y. & John, A. R. (2017) Mechanically-guided deterministic assembly of 3D mesostructures assisted by residual stresses. *Small*. (accepted)

Gratson, G. M., Xu, M. J. & Lewis, J. A. (2004) Microperiodic structures – Direct writing of three-dimensional webs. *Nature*, 428, 386–386.

Guo, X. Y., Li, H., Ahn, B. Y., Duoss, E. B., Hsia, K. J., Lewis, J. A. & Nuzzo, R. G. (2009) Two- and three-dimensional folding of thin film single-crystalline silicon for photovoltaic power applications. *Proceedings of the National*

Academy of Sciences of the United States of America, 106, 20149–20154.

Huang, M. H., Cavallo, F., Liu, F. & Lagally, M. G. (2011) Nanomechanical architecture of semiconductor nanomembranes. *Nanoscale*, 3, 96–120.

Huang, W., Yu, X., Froeter, P., Xu, R., Ferreira, P. & Li, X. (2012) On-chip inductors with self-rolled-up SiNx nanomembrane tubes: a novel design platform for extreme miniaturization. *Nano letters*, 12, 6283–6288.

Kim, J., Hanna, J. A., Byun, M., Santangelo, C. D. & Hayward, R. C. (2012) Designing Responsive Buckled Surfaces by Halftone Gel Lithography. *Science*, 335, 1201–1205.

Klein, Y., Efrati, E. & Sharon, E. (2007) Shaping of elastic sheets by prescription of non-Euclidean metrics. *Science*, 315, 1116–1120.

Ladd, C., So, J.-H., Muth, J. & Dickey, M. D. (2013a) 3D Printing of Free Standing Liquid Metal Microstructures. *Advanced Materials*, 25, 5081–5085.

Ladd, C., So, J. H., Muth, J. & Dickey, M. D. (2013b) 3D Printing of Free Standing Liquid Metal Microstructures. *Advanced Materials*, 25, 5081–5085.

Lee, J.-H., Koh, C. Y., Singer, J. P., Jeon, S.-J., Maldovan, M., Stein, O. & Thomas, E. L. (2014) 25th Anniversary Article: Ordered Polymer Structures for the Engineering of Photons and Phonons. *Advanced Materials*, 26, 532–568.

Leong, T. G., Randall, C. L., Benson, B. R., Bassik, N., Stern, G. M. & Gracias, D. H. (2009) Tetherless thermobiochemically actuated microgrippers. *Proceedings of the National Academy of Sciences of the United States of America*, 106, 703–708.

Lewis, J. A. (2006) Direct ink writing of 3D functional materials. *Advanced Functional Materials*, 16, 2193–2204.

Lewis, J. A., Smay, J. E., Stuecker, J. & Cesarano, J., Iii (2006) Direct ink writing of three-dimensional ceramic structures. *Journal of the American Ceramic Society*, 89, 3599–3609.

Li, H., Guo, X., Nuzzo, R. G. & Jimmy Hsia, K. (2010) Capillary induced self-assembly of thin foils into 3Dstructures. *Journal of the Mechanics and Physics of Solids*, 58, 2033–2042.

Li, X. (2008) Strain induced semiconductor nanotubes: from formation process to device applications. *Journal of Physics D: Applied Physics*, 41, 193001.

Li, X. (2011) Self-rolled-up microtube ring resonators: a review of geometrical and resonant properties. *Advances in Optics and Photonics*, 3, 366.

Liu, Y., Yan, Z., Lin, Q., Guo, X., Han, M., Nan, K., Hwang, K. C., Huang, Y., Zhang, Y. & Rogers, J. A. (2016) Guided Formation of 3D Helical Mesostructures by Mechanical Buckling: Analytical Modeling and Experimental Validation. *Advanced functional materials*, 26, 2909–2918.

Na, J. H., Evans, A. A., Bae, J., Chiappelli, M. C., Santangelo, C. D., Lang, R. J., Hull, T. C. & Hayward, R. C. (2015) Programming reversibly self-folding origami with micropatterned photo-crosslinkable polymer trilayers. *Adv Mater*, 27, 79–85.

Nan, K., Luan, H., Yan, Z., Ning, X., Wang, Y., Wang, A., Wang, J., Han, M., Chang, M., Li, K., Zhang, Y., Huang, W., Xue, Y., Huang, Y., Zhang, Y. & Rogers, J. A. (2016) Engineered Elastomer Substrates for Guided Assembly of Complex 3D Mesostructures by Spatially Nonuniform Compressive Buckling. *Advanced Functional Materials*, 27, 1604281.

Ning, X., Wang, H., Yu, X., Soares, J. a. N. T., Yan, Z., Nan, K., Velarde, G., Xue, Y., Sun, R., Dong, Q., Luan, H., Lee, C. M., Chempakasseril, A., Han, M., Wang, Y., Li, L., Huang, Y., Zhang, Y. & Rogers, J. A. (2017) 3D Tunable, Multiscale, and Multistable Vibrational Micro-Platforms Assembled by Compressive Buckling. *Advanced Functional Materials*, 1605914.

Pandey, S., Ewing, M., Kunas, A., Nguyen, N., Gracias, D. H. & Menon, G. (2011) Algorithmic design of self-folding polyhedra. *Proceedings of the National Academy of Sciences of the United States of America*, 108, 19885–19890.

Pandey, S., Gultepe, E. & Gracias, D. H. (2013) Origami inspired self-assembly of patterned and reconfigurable particles. *Journal of visualized experiments: JoVE*, e50022.

Py, C., Reverdy, P., Doppler, L., Bico, J., Roman, B. & Baroud, C. N. (2007) Capillary origami: spontaneous wrapping of a droplet with an elastic sheet. *Physical review letters*, 98, 156103.

Randhawa, J. S., Leong, T. G., Bassik, N., Benson, B. R., Jochmans, M. T. & Gracias, D. H. (2008) Pick-and-Place Using Chemically Actuated Microgrippers. *Journal of the American Chemical Society*, 130, 17238–17239.

Schaedler, T. A., Jacobsen, A. J., Torrents, A., Sorensen, A. E., Lian, J., Greer, J. R., Valdevit, L. & Carter, W. B. (2011) Ultralight Metallic Microlattices. *Science*, 334, 962–965.

Schmidt, O. G., Deneke, C., Manz, Y. M. & Muller, C. (2002) Semiconductor tubes, rods and rings of nanometer and micrometer dimension. *Physica E: Low-Dimensional Systems and Nanostructures*, 13, 969–973.

Schmidt, O. G. & Eberl, K. (2001) Nanotechnology – Thin solid films roll up into nanotubes. *Nature*, 410, 168–168.

Shi, Y., Zhang, F., Nan, K., Wang, X., Wang, J., Zhang, Y., Zhang, Y., Luan, H., Hwang, K.-C., Huang, Y., Rogers, J. A. & Zhang, Y. (2017) Plasticity-induced origami for assembly of three dimensional metallic structures guided by compressive buckling. *Extreme Mechanics Letters*, 11, 105–110.

Sidorenko, A., Krupenkin, T., Taylor, A., Fratzl, P. & Aizenberg, J. (2007) Reversible switching of hydrogel-actuated nanostructures into complex micropatterns. *Science*, 315, 487–490.

Song, Z., Ma, T., Tang, R., Cheng, Q., Wang, X., Krishnaraju, D., Panat, R., Chan, C. K., Yu, H. & Jiang, H. (2014) Origami lithium-ion batteries. *Nature Communications*, 5, 3140.

Tian, B., Liu, J., Dvir, T., Jin, L., Tsui, J. H., Qing, Q., Suo, Z., Langer, R., Kohane, D. S. & Lieber, C. M. (2012) Macroporous nanowire nanoelectronic scaffolds for synthetic tissues. *Nature Materials*, 11, 986–994.

Valentine, J., Zhang, S., Zentgraf, T., Ulin-Avila, E., Genov, D. A., Bartal, G. & Zhang, X. (2008) Three-dimensional optical metamaterial with a negative refractive index. *Nature*, 455, 376–U32.

Wei, Z., Jia, Z., Athas, J., Wang, C., Raghavan, S. R., Li, T. & Nie, Z. (2014) Hybrid hydrogel sheets that undergo pre-programmed shape transformations. *Soft Matter*, 10, 8157–8162.

Wu, H., Yu, G., Pan, L., Liu, N., Mcdowell, M. T., Bao, Z. & Cui, Y. (2013) Stable Li-ion battery anodes by in-situ polymerization of conducting hydrogel to conformally coat silicon nanoparticles. *Nature Communications*, 4, 1943.

Xia, Y., Cedillo-Servin, G., Kamien, R. D. & Yang, S. (2016) Guided Folding of Nematic Liquid Crystal Elastomer Sheets into 3D via Patterned 1D Microchannels. *Advanced Materials*, 28, 9637–9643.

Xu, S., Yan, Z., Jang, K.-I., Huang, W., Fu, H., Kim, J., Wei, Z., Flavin, M., Mccracken, J., Wang, R., Badea, A., Liu, Y., Xiao, D., Zhou, G., Lee, J., Chung, H. U., Cheng, H., Ren, W., Banks, A., Li, X., Paik, U., Nuzzo, R. G., Huang, Y., Zhang, Y. & Rogers, J. A. (2015) Assembly

of micro/nanomaterials into complex, three-dimensional architectures by compressive buckling. *Science*, 347, 154–159.

Xu, X., Zhang, H., Zhang, L., Wang, Z., Jiang, Y. & Wu, Z. (2009) Stress Engineering of SiNx Films for Modifying Optical and Mechanical Properties. *Journal of Physical Chemistry C*, 113, 4634–4640.

Yan, Z., Han, M., Yang, Y., Nan, K., Luan, H., Luo, Y., Zhang, Y., Huang, Y. & Rogers, J. A. (2017) Deterministic assembly of 3D mesostructures in advanced materials via compressive buckling: A short review of recent progress. *Extreme Mechanics Letters*, 11, 96–104.

Yan, Z., Zhang, F., Liu, F., Han, M., Ou, D., Liu, Y., Lin, Q., Guo, X., Fu, H., Xie, Z., Gao, M., Huang, Y., Kim, J., Qiu, Y., Nan, K., Kim, J., Gutruf, P., Luo, H., Zhao, A., Hwang, K.-C., Huang, Y., Zhang, Y. & Rogers, J. A. (2016a) Mechanical assembly of complex, 3D mesostructures from releasable multilayers of advanced materials. *Science Advances*, 2, e1601014.

Yan, Z., Zhang, F., Wang, J., Liu, F., Guo, X., Nan, K., Lin, Q., Gao, M., Xiao, D., Shi, Y., Qiu, Y., Luan, H., Kim, J. H., Wang, Y., Luo, H., Han, M., Huang, Y., Zhang, Y. & Rogers, J. A. (2016b) Controlled mechanical buckling for origami-inspired construction of 3D microstructures in advanced materials. *Advanced functional materials*, 26, 2629–2639.

Yoo, H. G., Byun, M., Jeong, C. K. & Lee, K. J. (2015) Performance Enhancement of Electronic and Energy Devices via Block Copolymer Self-Assembly. *Advanced Materials*, 27, 3982–3998.

Yu, X., Huang, W., Li, M., Comberiate, T. M., Gong, S., Schutt-Aine, J. E. & Li, X. (2015) Ultra-Small, High-Frequency, and Substrate-Immune Microtube Inductors Transformed from 2D to 3D. *Scientific Reports*, 5.

Zhang, H., Yu, X. & Braun, P. V. (2011) Three-dimensional bicontinuous ultrafast-charge and -discharge bulk battery electrodes. *Nature Nanotechnology*, 6, 277–281.

Zhang, Y., Yan, Z., Nan, K., Xiao, D., Liu, Y., Luan, H., Fu, H., Wang, X., Yang, Q., Wang, J., Ren, W., Si, H., Liu, F., Yang, L., Li, H., Wang, J., Guo, X., Luo, H., Wang, L., Huang, Y. & Rogers, J. A. (2015) A mechanically driven form of Kirigami as a route to 3D mesostructures in micro/nanomembranes. *Proceedings of the National Academy of Sciences of the United States of America*, 112, 11757–11764.

Zheng, W. & Jacobs, H. O. (2005) Fabrication of multi-component microsystems by directed three-dimensional self-assembly. *Advanced Functional Materials*, 15, 732–738.

Zheng, X., Lee, H., Weisgraber, T. H., Shusteff, M., Deotte, J., Duoss, E. B., Kuntz, J. D., Biener, M. M., Ge, Q., Jackson, J. A., Kucheyev, S. O., Fang, N. X. & Spadaccini, C. M. (2014) Ultralight, Ultrastiff Mechanical Metamaterials. *Science*, 344, 1373–1377.

Zhu, S. & Li, T. (2013) Hydrogenation enabled scrolling of graphene. *Journal of Physics D-Applied Physics*, 46, 075301.

Zhu, S. & Li, T. (2014) Hydrogenation-Assisted Graphene Origami and Its Application in Programmable Molecular Mass Uptake, Storage, and Release. *Acs Nano*, 8, 2864–2872.

Zhu, Y. & Chang, T.-H. (2015) A review of microelectromechanical systems for nanoscale mechanical characterization. *Journal of Micromechanics and Microengineering*, 25, 093001.

Shell Structures: Theory and Applications Volume 4 – Pietraszkiewicz & Witkowski (eds)
© 2018 Taylor & Francis Group, London, ISBN 978-1-138-05045-7

Topology and material optimization of plates and shells

T. Lewiński, S. Czarnecki, R. Czubacki & T. Sokół
Warsaw University of Technology, Warsaw, Poland

ABSTRACT: The paper deals with the problem of compliance minimization of thin transversely homogeneous shells and plates within the framework of the *free material design*. The elastic moduli are design variables, while the isoperimetric condition is expressed by the integral of the trace of Hooke's tensor. The optimum design problems, in various settings, are reduced to the two mutually dual auxiliary problems similar to those known from Michell's theory of structures of minimal weight. Like Michell's structures, the optimal shells are cut out from the design domain by the procedure of solving the auxiliary problems. The method proposed solves simultaneously two problems: optimal material layout and optimal shape of the structure, without any restrictions on the number of holes emerging in the optimal design.

1 INTRODUCTION

The *compliance*, denoted as $\wp$ in the paper, is the most important notion of the theory of optimization of structural topology. It is defined as the work of the load, or the value of the virtual work on the displacement field caused by the same load. On the other hand $(1/2)\wp$ is equal to the minimum value of the complementary energy over the trial stress fields taken from the set $\Sigma(\Omega)$ of statically admissible stresses. The latter formula is crucial for the present treatment. In some rare cases the set $\Sigma(\Omega)$ consists of a single element, which makes the minimization operation trivial. The fundamental optimization problem (P):

from a given amount of an elastic material make up the least compliant structure which transmits a given load to the given support domain

turns out to be badly posed. The solution should be looked for in the class of structures made of composites whose anisotropic properties are determined by the material layout within the representative volume elements. These properties vary within the design domain, thus making the structure simultaneously inhomogeneous and anisotropic. Thus, the initial problem of structural optimization transforms into the optimum design problem of composites of unknown and inhomogeneous porosity. The shape design assumes the form of a *generalized shape design*, see Cherkaev (2000), Allaire (2002, Sec. 4.1.3). In its generalized form, the problem (P) reads

$$\min_{\substack{m\in L^\infty(\Omega;\,[0,1])\\ \int_\Omega m dx = V}} J(m) \tag{1}$$

where m stands for the volume fraction and

$$J(m) = \min_{\boldsymbol{\tau}\in\Sigma(\Omega)} \int_\Omega U^*(\boldsymbol{\tau}, m) dx \tag{2}$$

while $\boldsymbol{\tau}, U^*, \Sigma(\Omega))$ depend on the formulation. This generalized form is constructed by the method called: *relaxation by homogenization*.

In the case of in-plane loaded plates the field $\boldsymbol{\tau}$ represents in-plane resultants $\mathbf{N}$ of stresses, the potential $U^*(\boldsymbol{\tau}, m)$ being known, see (Cherkaev 2000, Allaire 2002) and Lewiński (2004b, Eq. 34). Locally, the field $\boldsymbol{\tau}$ belongs to the set E^2_s of symmetric tensors of 2nd rank. This problem will be called (P_1).

In the case of bending plates $\boldsymbol{\tau}$ represents the couple resultants (or moments) $\mathbf{M}$, $\Sigma(\Omega)$ being the set of statically admissible moments compatible with the transverse load; the potential U^* can be found in Cherkaev (2000), see (Lewiński & Telega 2000, Eq. 26.7.12). This problem will be called (P_2).

In the case of plates simultaneously loaded in-plane and out of plane the fields $\boldsymbol{\tau}$ are pairs $(\mathbf{N}, \mathbf{M})$; the set $\Sigma(\Omega)$ comprises all the pairs $(\mathbf{N}, \mathbf{M})$ which satisfy the equilibrium equations, along with static boundary conditions. The explicit form of the potential U^* is still unknown; its approximation has been constructed by Dzierżanowski (2012) thus making it possible to pose and solve this problem, called (P_3) in the sequel.

It seems that the problem (1, 2) can be put in the form

$$\min_{\boldsymbol{\tau}\in\Sigma(\Omega)} \int_\Omega F_V(\boldsymbol{\tau}) dx \tag{3}$$

yet the explicit form of $F_V(\boldsymbol{\tau})$ in problems (P_1), (P_2) is highly complex, while in problem (P_3) is

still unknown. The passage from (1, 2) to (3) means performing minimization of $U^*(\boldsymbol{\tau}, m)$ over m with additional constraints: $0 \le m \le 1$, which make the operation complicated. Thus, due to complex form of $F_V(\boldsymbol{\tau})$ in problems (P_1)–(P_3) one can assume that the problems considered cannot be effectively put in the form (3). Let us remind here that the fundamental problem (P_{M}) by Michell (1904):

in a given design domain construct the lightest structure, stressed up to a given limit, capable of transmitting the given load to the given support domain.

can be put in the form

$$\min_{\boldsymbol{\tau} \in \Sigma(\Omega)} \int_{\Omega} d\varrho_M(\boldsymbol{\tau}) \tag{4}$$

where

$$\varrho_M(\boldsymbol{\tau}) = \sum_{i=1}^{n} |\lambda_i(\boldsymbol{\tau})| \tag{5}$$

and $\lambda_i(\boldsymbol{\tau})$ are eigenvalues of $\boldsymbol{\tau}$ while n is the dimension of the space $\mathbb{R}^n$ in which the design domain is defined. In regular cases: $d\varrho_{\mathrm{M}} = \varrho_{\mathrm{M}} dx$, dx being Lebesgue measure. The formulation (4, 5) can be found in Rozvany (1976) for the problem (P_2) and in Strang & Kohn (1983) for problem (P_1), cf. Bouchitté et al. (2008) for the contemporary and complete setting.

The role of problem (4) is fundamental. It occurs that the shape of the optimal structure is given by the support of the measure ϱ_{M}. The integrand $\varrho_{\mathrm{M}}(\boldsymbol{\tau})$ grows linearly; consequently the minimizer $\hat{\boldsymbol{\tau}}$ may vanish on a subdomain of the design domain. Thus, the problem (4) delivers a tool for cutting out the material domain Ω_m from the design domain Ω. The material domain Ω_m may be multiconnected. This process of cutting out the material domain from the design domain is cleared up in Fig. 1 concerning an illustrative planar Michell problem.

The field $\rho_{\mathrm{M}}(\boldsymbol{\tau})$ determines a fibrous microstructure of the optimal design. Due to the presence of the point loads the optimal structure becomes strengthened by ribs along some of its boundaries, interacting with the fibrous interior. We note that the boundary of the optimal structure is sharp, even when the boundary is not reinforced by a rib.

The possibility of reducing the initial optimization problem to an auxiliary problem can be viewed as the condition of its correctness. Note, that the relaxation by homogenization method leads to (4) only theoretically; the integrand cannot be expressed explicitly. Thus, it is helpful to propose alternative methods delivering explicit forms of problem (4). Let us emphasize here that the recently developed versions of the *Free Material Design* (FMD) satisfy this requirement. The aim of the paper is to specify and discuss these methods for optimum design of plates and shells.

The origin of FMD can be found in Bendsøe et al. (1994). The problem posed there will be named

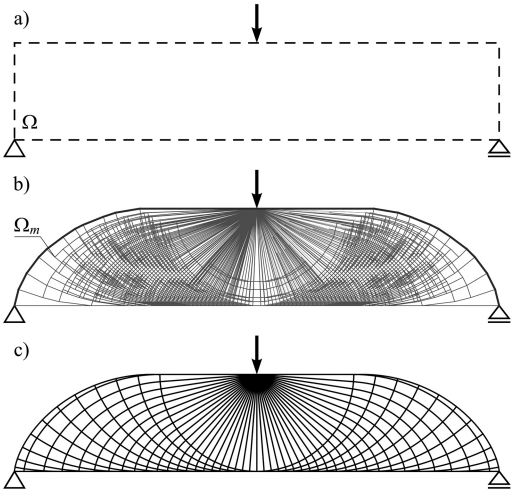

Figure 1. a) problem formulation; b) solution to the Michell's problem found by T. Sokół by the ground structure method, see Sokół (2011); c) a sketch of the analytical solution.

anisotropic material design (AMD), since no restrictions on anisotropy have been imposed there. The merit function is the compliance, while all the elastic moduli (viz. components of Hooke's tensor $\mathbf{C}$) are design variables. The tensor $\mathbf{C}$ is subject to the condition of positive semi-definiteness (to be written symbolically as $\mathbf{C} \ge \mathbf{0}$) and to the known symmetry conditions characteristic for Hooke's tensors, reflected in the requirement: $\mathbf{C} \in \mathbb{E}^4_s$. The isoperimetric condition is assumed in the form

$$\int_{\Omega} \operatorname{tr} \mathbf{C} dx = \Lambda \tag{6}$$

where $\operatorname{tr} \mathbf{C}$ is the sum of eigenvalues of $\mathbf{C}$. Let us stress that in the AMD problem the tensor $\mathbf{C}$ is constrained only by the conditions mentioned above. Let us formulate the *anisotropic material design* problem $(\mathrm{P}_{\mathrm{AMD}})$:

find the least compliant elastic anisotropic body whose moduli constitute a positive semidefinite Hooke tensor field $\mathbf{C}$ *satisfying the isoperimetric condition (6).*

It turns out that the problem above leads to the auxiliary problem of type (4) with the integrand expressed by the Euclidean norm: $\varrho(\boldsymbol{\tau}) = ||\boldsymbol{\tau}||$, $||\boldsymbol{\tau}|| = \sqrt{\boldsymbol{\tau} \cdot \boldsymbol{\tau}}$. Having found the minimizer $\hat{\boldsymbol{\tau}}$ one can construct the optimal tensor $\hat{\mathbf{C}}$, cf. Czarnecki & Lewiński (2014). The optimal tensor $\hat{\mathbf{C}}$ shows only one non-zero eigenvalue; the solution is highly singular. Optimal anisotropy is ideally made up for the given load and is incapable to resist to any other load. Tensor $\hat{\mathbf{C}}$ is determined only there, where $\hat{\boldsymbol{\tau}}$ is non-zero. The domain where $\hat{\boldsymbol{\tau}}$ is zero is cut out; this domain is empty or non-material.

A natural variant of FMD is the *cubic material design* (CMD) in which tensor $\mathbf{C}$ is a priori subject

to the condition of cubic symmetry. Such symmetry is characteristic for many crystalline bodies. The isoperimetric condition (6) is kept unchanged. The minimization operation leads to the auxiliary problem of type (4) with the integrand

$$\varrho_\gamma(\boldsymbol{\tau}) = \left|\frac{\operatorname{tr}\boldsymbol{\tau}}{\sqrt{n}}\right| + \gamma||\operatorname{dev}\boldsymbol{\tau}|| \tag{7}$$

In the 3D case $n=3$ and $\gamma=\sqrt{2}$. In any case of load and design domain one of the eigenvalues of $\mathbf{C}$, of multiplicity equal 3, vanishes, see Czubacki & Lewiński (2015).

The next natural alternative is assuming isotropy. In the IMD version the *isotropic material design* problem ($\mathrm{P_{IMD}}$) reads:

construct the least compliant body made of isotropic material characterized by the non-negative bulk modulus $k(x)$ and the non-negative shear modulus $\mu(x)$ satisfying the isoperimetric condition (6).

Thus, the fields k,μ are the only design variables. In the case of isotropy the eigenvalues of $\mathbf{C}$ are: $(3k, 2\mu, 2\mu, 2\mu, 2\mu, 2\mu)$, hence $\operatorname{tr}\mathbf{C} = 3k + 10\mu$. One can prove that the IMD problem reduces to (4) with the integrand $\varrho_{\sqrt{5}}(\boldsymbol{\tau})$. The problem (4), with this norm, determines a minimizer $\hat{\boldsymbol{\tau}}$. This field establishes the optimal isotropic moduli $\hat{k}$ and $\hat{\mu}$; $\hat{k}$ is proportional to $|\operatorname{tr}\hat{\boldsymbol{\tau}}|$ and $\hat{\mu}$ is proportional to $||\operatorname{dev}(\hat{\boldsymbol{\tau}})||$, see (Czarnecki 2015 and Czarnecki & Wawruch 2015).

The simplest version of FMD is YMD: designing the Young modulus $E(x)$, keeping the Poisson ratio $\nu=\nu(x)$ fixed. The isoperimetric condition (6) is kept. If $\nu=\text{const}$, the unit cost is simply proportional to E. The YMD problem ($\mathrm{P_{YMD}}$) reads:

construct the least compliant body made of isotropic material of the prescribed Poisson ratio field $\nu(x)$. Find the optimal distribution of Young's modulus $E(x)\geq 0$, satisfying the isoperimetric condition (6).

This problem leads to an auxiliary problem (4) with the integrand given by

$$\begin{aligned}
\varrho_Y(\boldsymbol{\tau}) &= \left[\frac{6-9\nu}{3(1+\nu)}(\operatorname{tr}\boldsymbol{\tau})^2 + \frac{6-9\nu}{1-2\nu}||\operatorname{dev}\boldsymbol{\tau}||^2\right]^{\frac{1}{2}} \\
\varrho_Y(\boldsymbol{\tau}) &= \left[\frac{3-\nu}{2(1+\nu)}(\operatorname{tr}\boldsymbol{\tau})^2 + \frac{3-\nu}{1-\nu}||\operatorname{dev}\boldsymbol{\tau}||^2\right]^{\frac{1}{2}}
\end{aligned} \tag{8}$$

for $n=3$ and $n=2$, respectively. Let $\hat{\boldsymbol{\tau}}$ be the minimizer of this auxiliary problem. The optimal Young's modulus $\hat{E}$ is proportional to $\varrho_Y(\hat{\boldsymbol{\tau}})$, see (Czarnecki & Lewiński 2017, Eq. 2.34). The effective domain of $\hat{\boldsymbol{\tau}}$ cuts out the material domain Ω_m from Ω.

The YMD is the only method which always determines the optimal tensor $\hat{\mathbf{C}}$ in the material domain Ω_m as a non-singular tensor. Note, that the IMD method divides the design domain into the subdomains: Ω_{m1} where $\hat{k}>0$ and $\hat{\mu}>0$; Ω_{m2} where $\hat{k}=0$ and $\hat{\mu}>0$, Ω_{m3} where $\hat{k}>0$ and $\hat{\mu}=0$, $\Omega_4=\Omega\backslash\Omega_m$, where both $\hat{k}$ and $\hat{\mu}$ vanish. On the other hand, the CMD always leads to singular $\mathbf{C}$. The most dramatic singularity is produced by AMD; the optimal $\mathbf{C}$ exhibits only one non-zero eigenvalue. We conclude that the greatest choice the strongest singularity of the result.

The possible remedy is to optimize the structure with respect to many load variants. In the case of the AMD approach the $3(n-1)$ load variants suffice to make $\mathbf{C}$ non-singular. Then the number of load variants equals the number of stress components, cf. Czarnecki & Lewiński (2014).

The FMD methods have been already applied to shells in Gaile et al. (2009), where Naghdi's (1963) shell model has been used. The AMD problem has been reduced there to an auxiliary problem of maximization of the virtual work (with extra terms) over virtual displacements being locally bounded, see problem (29) therein. A direct comparison is not possible, since even if the transverse shear deformations are neglected, the AMD problem in Gaile et al. (2009) does not coincide with the problem discussed in the present paper; it involves some extra conditions omitted here. Nevertheless, this problem (29) can be viewed as a counterpart of the problem dual to (4) with an appropriately modified integrand. Moreover, solving the problem (4) paves the way towards optimal moduli, while solving its dual only starts a long procedure to determine the moduli. This will be cleared up in the paper. Recently, a new numerical procedure for the FMD problems of shells and laminates has been presented in Weldeysus & Stolpe (2016).

The simplest version of ($\mathrm{P_{AMD}}$) for thin shells has been proposed in Czarnecki et al. (2014). The problem has been reduced there to the form (4) with the integrand of linear growth. This formulation will be complemented here by its dual form in Sec. 5.3.

The main aim of the paper is to extend the IMD and YMD formulations (known for plates loaded in plane and for 3D setting) towards coupled problems of plates and shells. The optimum design problems will be reduced to the form (4) to have *the tool of cutting the material domain from the design domain*. For maximum simplicity we assume that the shell is transversely homogeneous, sufficiently thin to neglect transverse deformations, and its thickness is constant. The shape of the middle surface is not subject to optimization. The only design variables are elastic moduli, regarded as fields referred to the middle surface. The optimum design will lead to the membrane-bending coupling even in the case where the statics problem is decoupled.

2 DESIGN OF ISOTROPIC PROPERTIES (IMD) OF THIN TRANSVERSELY HOMOGENEOUS PLATES

Consider a thin isotropic transversely homogeneous plate of middle plane Ω and constant thickness h. Let the Cartesian coordinates (x_1,x_2) parameterize Ω; the

unit basis vectors being $\mathbf{e}_1, \mathbf{e}_2$. Let x_3 be orthogonal to the plane. The domain of the plate is: $x = (x_1, x_2) \in \Omega$, $|x_3|, \leq h/2$. Let $\mathbf{u} = (u_1, u_2)$ represent in-plane displacements while w is deflection along x_3. Assume generalized plane stress state, as usual in the plate theory. The isotropic Hooke tensor is represented by

$$\mathbf{C} = 2k\mathbf{\Lambda}_1 + 2\mu\mathbf{\Lambda}_2 \tag{9}$$

where k and μ are bulk and shear moduli, respectively. Moreover

$$\mathbf{\Lambda}_1 = \frac{1}{2}\delta_{\alpha\beta}\delta_{\lambda\mu}\mathbf{e}_\alpha \otimes \mathbf{e}_\beta \otimes \mathbf{e}_\lambda \otimes \mathbf{e}_\mu, \quad \mathbf{\Lambda}_1 = \mathbf{I}^4 - \mathbf{\Lambda}_1 \tag{10}$$

and $\mathbf{I}^4$ is the unit tensor in $\mathbb{E}^4_s$. The moduli k and μ are linked with Young's modulus E and Poisson ratio ν by

$$2k = \frac{E}{1-\nu}, \qquad 2\mu = \frac{E}{1+\nu} \tag{11}$$

Note that $\mathrm{tr}\,\mathbf{C} = 2k + 4\mu$. We assume that the plate is transversely homogeneous, hence k and μ depend on $x = (x_1, x_2)$ only. The stress resultants $\mathbf{N} = (N_{\alpha\beta})$ and couple resultants $\mathbf{M} = (M_{\alpha\beta})$ of the plate are linked with in-plane strains $\gamma_{\alpha\beta} = \varepsilon_{\alpha\beta}(\mathbf{u})$ and changes of curvature $\varkappa_{\alpha\beta} = -w_{,\alpha\beta}$ by

$$\mathbf{N} = h\mathbf{C}\boldsymbol{\gamma}, \qquad \mathbf{M} = \frac{h^3}{12}\mathbf{C}\boldsymbol{\varkappa} \tag{12}$$

Here $\varepsilon_{\alpha\beta}(\mathbf{u})$ is the symmetric part of $\nabla\mathbf{u}$ and $\nabla\mathbf{u} = (u_{\alpha,\beta})$. Let $V(\Omega)$ be the space of kinematically admissible displacements $(\mathbf{u}, w)$ and let $f(\mathbf{u}, w)$ represent the virtual work of the load.

The fields $(\mathbf{N}, \mathbf{M})$ are regarded statically admissible if

$$\int_\Omega (\mathbf{N}\cdot\boldsymbol{\varepsilon}(\mathbf{v}) + \mathbf{M}\cdot\boldsymbol{\varkappa}(v))dx = f(\mathbf{v},\ v) \qquad \forall\ (\mathbf{v}, v) \in V(\Omega) \tag{13}$$

where $\boldsymbol{\varkappa}(v) = (-v_{,\alpha\beta})$. Next we write $(\mathbf{N}, \mathbf{M}) \in \Sigma_0(\Omega)$, the set $\Sigma_0(\Omega)$ comprises all the fields $(\mathbf{N}, \mathbf{M})$ statically admissible.

According to Castigliano theorem the compliance of the plate, viewed here as a function of k and μ, is expressed by

$$\wp(k,\mu) = \frac{1}{h}\min_{(\mathbf{N},\mathbf{M})\in\Sigma_0(\Omega)} \int_\Omega \left[\mathbf{N}\cdot(\mathbf{C}^{-1}\mathbf{N}) + \frac{12}{h^2}\mathbf{M}\cdot(\mathbf{C}^{-1}\mathbf{M})\right] dx \tag{14}$$

If the pair $(\mathbf{N}, \mathbf{M})$ solves this problem, there exist the fields $(\mathbf{u}, w) \in V(\Omega)$ such that (12) holds, where $\boldsymbol{\gamma} = \boldsymbol{\varepsilon}(\mathbf{u})$, $\boldsymbol{\varkappa} = (-w_{,\alpha\beta})$. The value $\varrho(k,\mu)$ is equal $f(\mathbf{u}, w)$.

Let $\mathbf{K}^{(1)} = \mathbf{N}$, $\mathbf{K}^{(2)} = \left(\frac{\sqrt{12}}{h}\right)\mathbf{M}$, $\boldsymbol{\kappa} = \left(\frac{h}{\sqrt{12}}\right)\boldsymbol{\varkappa}$.

If $(\mathbf{N}, \mathbf{M}) \in \Sigma_0(\Omega)$ then $(\mathbf{K}^{(1)}, \mathbf{K}^{(2)}) \in \Sigma(\Omega)$.

Let us re-write problem (14) as

$$\wp(k,\mu) = \frac{1}{h}\min_{(\mathbf{K}^{(1)}\mathbf{K}^{(2)})\in\Sigma(\Omega)} \int_\Omega \sum_{\alpha=1}^{2} \mathbf{K}^{\alpha)}\cdot(\mathbf{C}^{-1}\mathbf{K}^{(\alpha)})dx \tag{15}$$

where $\mathbf{C}^{-1}$ is given by (9) with $(2k, 2\mu)$ being replaced by their inverses. Note that for $\boldsymbol{\tau} \in \mathbb{E}^2_s$

$$\boldsymbol{\tau}\cdot(\mathbf{C}^{-1}\boldsymbol{\tau}) = \frac{1}{2k}\left(\frac{\mathrm{tr}\,\boldsymbol{\tau}}{\sqrt{2}}\right)^2 + \frac{1}{2\mu}||\mathrm{dev}\,\boldsymbol{\tau}||^2 \tag{16}$$

Assume that the unit cost of the design is equal to $\mathrm{tr}\,\mathbf{C}$. Let the total cost of the design

$$\int_\Omega (2k + 4\mu)dx = \Lambda \tag{17}$$

be given. The optimum design problem is

$$\wp^0 = \min\{\wp(k,\mu) \mid k \geq 0,\ \mu \geq 0,\ \text{with (17)}\} \tag{18}$$

Thus, the aim is to find the optimal layouts of (k, μ) on the domain Ω to make the plate as stiff as possible among the plates of given cost (17). We interchange the minimization operations and perform minimization over the design variables (k, μ) analytically. The result is

$$\wp^0 = \frac{1}{h\Lambda}(Z_1)^2 \tag{19}$$

with

$$Z_1 = \min_{(\mathbf{K}^{(1)},\mathbf{K}^{(2)})\in\Sigma(\Omega)} \int_\Omega d\varrho_{\sqrt{2}}(\mathbf{K}^{(1)}, \mathbf{K}^{(2)}) \tag{20}$$

where

$$\varrho_{\sqrt{2}}(\boldsymbol{\tau}^{(1)}, \boldsymbol{\tau}^{(2)}) = \sqrt{\sum_{\alpha=1}^{2}\left(\frac{\mathrm{tr}\,\boldsymbol{\tau}^{(\alpha)}}{\sqrt{2}}\right)^2} + \sqrt{2}\sqrt{\sum_{\alpha=1}^{2}||\mathrm{dev}\,\boldsymbol{\tau}^{(\alpha)}||^2} \tag{21}$$

If $\alpha = 1$ then this norm assumes the form (7) for $n = 2$. The function $\varrho_{\sqrt{2}}(\cdot)$ is a norm in $\mathbb{E}^2_s \times \mathbb{E}^2_s$. Assume that $(\hat{\mathbf{K}}^{(1)}, \hat{\mathbf{K}}^{(2)})$ is a minimizer of (20). Then the optimal moduli of the material are expressed by

$$2\hat{k}(x) = \frac{\Lambda}{\displaystyle\int_\Omega d\varrho_{\sqrt{2}}\left(\hat{\mathbf{K}}^{(1)}, \hat{\mathbf{K}}^{(2)}\right)}\sqrt{\sum_{\alpha=1}^{2}\left(\frac{\mathrm{tr}\,\hat{\mathbf{K}}^{(\alpha)}(x)}{\sqrt{2}}\right)^2} \tag{22}$$

$$4\hat{\mu}(x) = \frac{\Lambda\sqrt{2}}{\displaystyle\int_\Omega d\varrho_{\sqrt{2}}\left(\hat{\mathbf{K}}^{(1)}, \hat{\mathbf{K}}^{(2)}\right)}\sqrt{\sum_{\alpha=1}^{2}||\mathrm{dev}\,\hat{\mathbf{K}}^{(\alpha)}(x)||^2}$$

We note that the moduli found above satisfy the cost condition (17). The optimal $\hat{E}, \hat{\nu}$ are given by (11).

In general, the minimizer of (20) is a pair of two Radon measures. In the regular case they are functions and the integrand of (20) reads $\varrho_{\sqrt{2}}(\mathbf{K}^{(1)}, \mathbf{K}^{(2)})dx$, dx being Lebesgue measure.

The passage from (18) to (19) is based on the following result, valid for appropriately regular function $F \geq 0$ defined in Ω:

$$\min_{\substack{u\geq 0 \\ \int_\Omega u dx = \Lambda}} \int_\Omega \frac{F(x)}{u(x)} dx = \frac{1}{\Lambda}\left(\int_\Omega \sqrt{F(x)} dx\right)^2 \tag{23}$$

and the minimum is attained for

$$\hat{u}(x) = \Lambda \frac{\sqrt{F(x)}}{\displaystyle\int_\Omega \sqrt{F(x)} dx} \tag{24}$$

The proof is based on Cauchy-Schwarz inequality, see (Sec. 2 in Czarnecki & Lewiński 2017). The crucial observation is that if F grows quadratically, the integrand at the r.h.s. of (23) grows linearly. Consequently, the minimizers of (20) are, in general, Radon measures. The problem (20) should be discussed and solved with a simultaneous analysis of its dual, which reads

$$Z_2 = \max\{f(\mathbf{v}, v) \mid (\mathbf{v}, v) \in V(\Omega), \\ \varrho^*_{\sqrt{2}}(\boldsymbol{\varepsilon}(\mathbf{v}), \boldsymbol{\kappa}(v)) \leq 1\} \tag{25}$$

where $\boldsymbol{\kappa}(v) = \left(\frac{h}{\sqrt{12}}\right)(-v_{,\alpha\beta})$ and $\varrho^*_{\sqrt{2}}(\cdot,\cdot)$ is a norm dual to the norm $\varrho_{\sqrt{2}}(\cdot,\cdot)$; it has the form

$$\varrho^*_{\sqrt{2}}(\boldsymbol{\varepsilon}^{(1)}, \boldsymbol{\varepsilon}^{(2)}) = \tag{26}$$
$$\max\left\{\sqrt{\sum_{\alpha=1}^{2}\left(\frac{\operatorname{tr}\boldsymbol{\varepsilon}^{(\alpha)}}{\sqrt{2}}\right)^2}, \frac{1}{\sqrt{2}}\sqrt{\sum_{\alpha=1}^{2}||\operatorname{dev}\boldsymbol{\varepsilon}^{(\alpha)}||^2}\right\}$$

One can prove that $Z_1 = Z_2$. A rigorous proof can be performed by following the arguments of Bouchitté & Buttazzo (2001). Problem (20) resembles (4), which links the discussed problem with Michell's theory.

The solution of (20) divides the middle plane of the plate into subdomains: a) material domain where both $\hat{k}$ and $\hat{\mu}$ are positive, b) material domain for which $\hat{k} > 0$ but $\hat{\mu} = 0$, c) material domain where $\hat{k} = 0$ and $\hat{\mu} > 0$ and d) empty domain in which $\hat{k} = 0$ and $\hat{\mu} = 0$. The first three domains determine the material subdomain Ω_m which is cut out from the design domain Ω. Thus, the method delivers the tool for *shape design*. The material design discussed here turns out to encompass the shape design tool.

3 YOUNG MODULUS DESIGN (YMD) OF THIN TRANSVERSELY HOMOGENEOUS PLATES

Assume that the Poisson's ratio field ν is transversely homogeneous and given; $\nu = \nu(x), x = (x_1, x_2)$. Young's modulus $E = E(x)$ will be the only design variable. The isoperimetric condition is still assumed by (6), it reads now

$$\int_\Omega E_1 dx = \Lambda, \quad E_1 = aE, \quad a(x) = \frac{3-\nu(x)}{1-\nu^2(x)} \tag{27}$$

Let us write down the representation (9) in the form

$$\mathbf{C} = E_1\mathbf{G}, \qquad \mathbf{G} = \frac{1+\nu}{3-\nu}\boldsymbol{\Lambda}_1 + \frac{1-\nu}{3-\nu}\boldsymbol{\Lambda}_2 \tag{28}$$

explicitly dependent on E_1. The compliance $\wp(E_1)$ of the plate is given by (15), where $\mathbf{C}$ is given by (28). Let us consider the optimum design problem in which the Young's modulus is the only design variable, by analogy to (18) we have

$$\wp^0 = \min\left\{\wp(E_1) \mid E_1 \geqslant 0, \int_\Omega E_1 dx = \Lambda\right\} \tag{29}$$

We interchange the sequence of minimization operations. Minimization over E_1 can be performed analytically using (23), (24). Thus we once again come across the result in the form (19), (20) where the integrand is given by the norm now:

$$\varrho_Y(\boldsymbol{\tau}^{(1)}, \boldsymbol{\tau}^{(2)}) = \tag{30}$$
$$\left[\frac{3-\nu}{1+\nu}\sum_{\alpha=1}^{2}\left(\frac{\operatorname{tr}\boldsymbol{\tau}^{(\alpha)}}{\sqrt{2}}\right)^2 + \frac{3-\nu}{1-\nu}\sum_{\alpha=1}^{2}||\operatorname{dev}\boldsymbol{\tau}^{(\alpha)}||^2\right]^{\frac{1}{2}}$$

Let $(\hat{\mathbf{K}}^{(1)}, \hat{\mathbf{K}}^{(2)})$ be the minimizer of the problem (20) with the norm (30). The optimal Young's modulus is given by

$$\hat{E}(x) = \frac{\Lambda \cdot \varrho_Y(\hat{\mathbf{K}}^{(1)}(x), \hat{\mathbf{K}}^{(2)}(x))}{a(x)\displaystyle\int_\Omega d\varrho_Y(\hat{\mathbf{K}}^{(1)}, \hat{\mathbf{K}}^{(2)})} \tag{31}$$

The condition (27) is fulfilled.

The problem (20) with the norm (30) should be considered jointly with its dual. It has the form (25) in which the norm $\varrho^*_{\sqrt{2}}(\cdot,\cdot)$ should be replaced with the norm dual to (30), or

$$\varrho^*_Y(\boldsymbol{\varepsilon}^{(1)}, \boldsymbol{\varepsilon}^{(2)}) = \tag{32}$$
$$\left[\frac{1+\nu}{3-\nu}\sum_{\alpha=1}^{2}\left(\frac{\operatorname{tr}\boldsymbol{\varepsilon}^{(\alpha)}}{\sqrt{2}}\right)^2 + \frac{1-\nu}{3-\nu}\sum_{\alpha=1}^{2}||\operatorname{dev}\boldsymbol{\varepsilon}^{(\alpha)}||^2\right]^{\frac{1}{2}}$$

The YMD method outlined here solves two problems simultaneously: the optimum shape and material problems. The domain, where $E_1 > 0$ is the domain of the plate; the domain where $E_1 = 0$ is cut out from the design domain. In the case of the in-plane loaded structures the YMD reduces to solving (4) with the integrand given by (8), the case of $n = 2$. An illustrative YMD solution is shown in Fig. 2 corresponding to the problem stated in Fig. 1.

Figure 2. The YMD solution for the problem posed in Fig. 1(a). The optimal layout of the Young's modulus E: a) contour plot; b) 3D plot.

4 ON OPTIMUM DESIGN OF MEMBRANE SHELLS

4.1 *Michell's problem of torsion*

Consider the problem of Fig. 3: to construct the lightest structure of a bounded stress level between two rings subjected to circumferential loadings of intensities: p_a, p_b, giving two resultant torques M of opposite directions; the radii of the rings are: a and b. The equilibrium condition implies

$$p_a = \frac{M}{2\pi a^2}, \qquad p_b = \frac{M}{2\pi b^2}. \tag{33}$$

Michell (1904) noted that the lightest structure is a membrane spherical shell.

Since this statement is still not proved, let us assume now that the solutions should be sought among membrane shells of revolution. This problem takes the form (4), (5) where $\boldsymbol{\tau} = \mathbf{N}$ is the field of stress resultants of the membrane shell. The problem thus formulated has been solved in Lewiński (2004a), where an elementary proof is given that the spherical shell is lighter than other membrane shells of revolution subjected to a given torsional load. The results of this paper have been recently confirmed numerically in Zegard & Paulino (2015).

The advanced numerical analysis of Zegard & Paulino (2015) confirms a spectacular prediction by Michell that a spherical shell is the solution to this torsion problem. The shape of a shell emerges due to the specific load applied along the curved lines.

Let us add that Kobelev has recently (2016) proved that the spherical shell is the stiffest among all elastic and isotropic shells loaded as in Fig. 3.

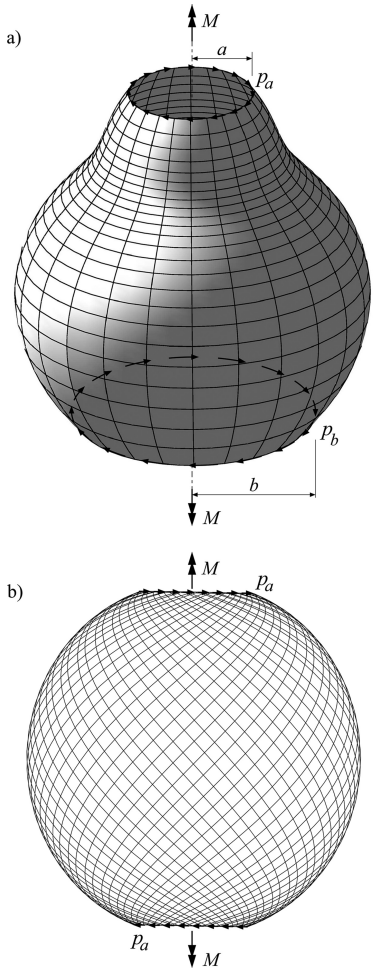

Figure 3. Michell's problem of torsion: a) posing the problem; b) sketch of the exact solution.

4.2 *Emerging of latticed shells of minimal weight*

If the load is concentrated at points or along curves in space the effective domain of the solution to problems (4), (5) may concentrate on surfaces, thus forming optimum designs in the form of shells of fibrous microstructure. The contemporary version of the *ground structure method* (see Gilbert & Tyas 2003; Pritchard et al. 2005; Sokół 2011, 2016) makes it possible to create such 3D solutions. The starting point is the *ground structure*: a truss of all possible members linking the joints within a given feasible domain. We consider here the problems (4), (5) corresponding to the four horizontal point loads of equal magnitudes applied at the vertices of the cuboid, orthogonally to the diagonals of the upper square side. The bottom square basis plays the role of the support domain. The optimal solution designed within the cuboid turns out to be a latticed shell of a non-smooth shape, arising from the square line of the support towards the points of application of the forces, see Fig. 4. The interior points of the support are left unused. The shell turns out to be stiffer than all other fibrous structures transmitting the given load to the support. The numerical solution presented in Fig. 4 was carried out using the program developed by Sokół (2016) with the spatial ground structure of $30 \times 30 \times 60$ cells and almost 1.5×10^9 bars. The analytical solution to this problem is unknown.

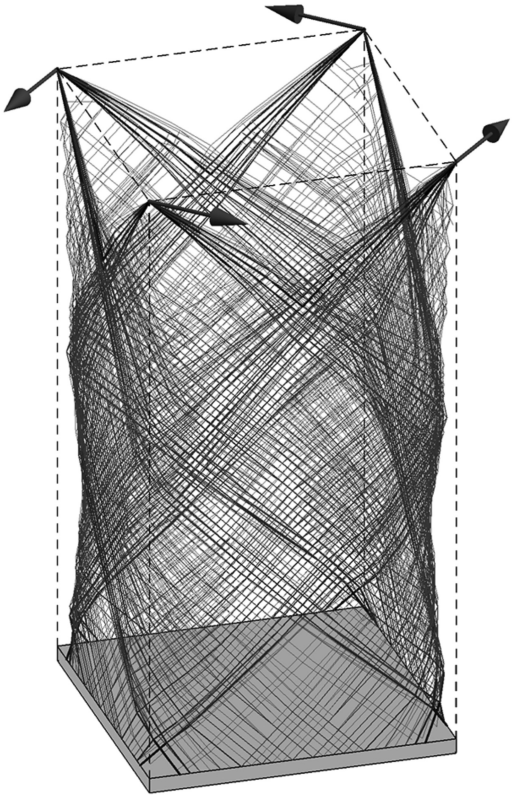

Figure 4. The lightest fully stressed structure transmitting the given four concentrated forces to the basis of the cuboid, being the design domain. The optimal latticed shell lies on the lateral sides of the feasible domain, thus making the interior of this domain almost empty.

4.3 *Isotropic material design*

In the membrane theory of shells the stretching tensor $\gamma_{\alpha\beta}$ is expressed by both the fields: $\mathbf{u}$ and w representing displacements in the tangent and normal directions, respectively, see (Naghdi 1963, Eq. 6.51). The field $\mathbf{N}$ is said to be statically admissible if

$$\int_\Omega \mathbf{N}\cdot\boldsymbol{\gamma}(\mathbf{v},v)d\Omega = f(\mathbf{v},v) \quad \forall\,(\mathbf{v},v)\in V(\Omega) \tag{34}$$

Here $f(\cdot,\cdot)$ must be compatible with the membrane theory which admits only the loads tangent to the edges, see Gol'denveizer (1976). Such fields $\mathbf{N}$ constitute the set $\Sigma(\Omega)$. There exists a class of problems in which this set is one element. These problems are considered statically determinate. Let $\mathcal{R}$ be the set of fields $(\mathbf{v},v)\in V(\Omega)$ such that $\boldsymbol{\gamma}(\mathbf{v},v)=\mathbf{0}$.

This is the set of inextensional deformations (some say: isometric deformations). If the shell is closed and convex, then $\mathcal{R}$ reduces to rigid motions: small rotations and translations, which has been proved by special tools of complex analysis, see Vekua (1982). If the shell is open and the edge is free, there exist isometric deformations not being rigid motions. For the spherical shell they have been already found by Rayleigh in the middle of XIX century and then repeated by A.E.H.Love in his seminal paper of 1889. One of such deformations can be seen on the cover of the book by Mazurkiewicz (2004).

The necessary condition of solvability of the membrane theory is: $f(\mathbf{v},v)=0\ \forall\,(\mathbf{v},v)\mathcal{R}\cap V(\Omega)$ to make both sides of the virtual equation (34) compatible. In the membrane theory the Castigliano theorem does not hold, but the compliance can be still defined in the form similar to (15) or

$$\wp(k,\mu)=\frac{1}{h}\min_{\mathbf{N}\in\Sigma(\Omega)}\int_\Omega \mathbf{N}\cdot(\mathbf{C}^{-1}\mathbf{N})d\Omega \tag{35}$$

where $\mathbf{C}$ is given by (9), while the basis $\mathbf{e}_\alpha$ is now local. Consider the problem (18) of construction of the fields k and μ on the shell middle surface, assuming transverse homogeneity. Minimization over k, μ leads to (19) where Z_1 takes the form

$$Z_1=\min_{\mathbf{N}\in\Sigma(\Omega)}\int_\Omega d\varrho_{\sqrt{2}}(\mathbf{N}) \tag{36}$$

and $\varrho_{\sqrt{2}}(\cdot)$ is given by (7), $n=2$, $\gamma=\sqrt{2}$.

Let $\hat{\mathbf{N}}$ be the minimizer of (36). The optimal moduli are given by the formulae

$$\begin{aligned} 2\hat{k}(x)&=\frac{\Lambda}{\displaystyle\int_\Omega d\varrho_{\sqrt{2}}(\hat{\mathbf{N}})}\left|\frac{\operatorname{tr}\hat{\mathbf{N}}(x)}{\sqrt{2}}\right| \\ 4\hat{\mu}(x)&=\frac{\sqrt{2}\Lambda}{\displaystyle\int_\Omega d\varrho_{\sqrt{2}}(\hat{\mathbf{N}})}||\operatorname{dev}\hat{\mathbf{N}}(x)|| \end{aligned} \tag{37}$$

which satisfy the isoperimetric condition (17) identically. There exists a rich class of problems where the set $\Sigma(\Omega)$ is one element and then (37) determine the isotropic moduli directly by the membrane stress resultants fields.

4.4 *Young's modulus design*

Consider transversely homogeneous shells of a prescribed Poisson's ratio distribution $\nu=\nu(x)$. The aim is to minimize the compliance (35), treated now as a function $\wp(E_1)$ where E_1 is defined by (27). The problem reduces to the construction of the minimizer $\hat{\mathbf{N}}$ of the problem

$$Z_1=\min_{\mathbf{N}\in\Sigma(\Omega)}\int_\Omega d\varrho_Y(\mathbf{N}) \tag{38}$$

where $\varrho_Y(\cdot)$ is given by (8), $n=2$. Having found $\hat{\mathbf{N}}$ one can determine the optimal distribution of Young's modulus by (31) or

$$\hat{E}(x)=\frac{\Lambda}{a(x)\displaystyle\int_\Omega d\varrho_Y(\hat{\mathbf{N}})}\varrho_Y(\hat{\mathbf{N}}(x)) \tag{39}$$

and $\hat{E}_1 = a\hat{E}$ satisfies (27). We note that if $\nu = \text{const}$, then $\hat{E}$ is proportional to the energy density.

Remark 4.1
Gol'denveizer (1976) noted that the system of equilibrium equations of membrane shells is elliptic at a point, if there the Gauss curvature $K > 0$; it is hyperbolic, if $K < 0$ and it is parabolic if K vanishes, see also Ciarlet & Sanchez-Palencia (1996). Therefore, if $K > 0$ then the fields $\mathbf{N}$ from the set $\Sigma(\Omega)$ will not vanish on subdomains of positive measure. We conclude that if the shell has a positive Gauss curvature everywhere (then we say that the middle surface is uniformly elliptic), the methods IMD and YMD will not predict emerging of the openings and will not tend to cut out boundary segments from the initial design domain. In other cases we should expect that cutting out some domains may lead to better designs. Note, that in the case of uniformly elliptic shells the normal displacement field may be eliminated thus leading to a reduced problem, see Ciarlet & Sanchez-Palencia (1996), which can be a proper starting point for any optimum design methods.

5 ON OPTIMUM DESIGN OF THIN TRANSVERSELY HOMOGENEOUS SHELLS OF CONSTANT THICKNESS

For the correct formulation of the optimum design of general thin elastic shells an appropriate theory is necessary in which Castigliano theorem holds and in which all the strain and stress measures are symmetric. A broad class of such theories have been discussed in (Naghdi 1963, Budiansky & Sanders 1963). Among these theories one can select a narrow class of theories in which the static-geometric analogy (discovered by A.I. Lur'e and A.L. Gol'denveizer in 1940's) holds. It turns out that just this analogy is very useful in the formulation and in the process of solving numerically the specific optimum design problems discussed in the paper. This analogy takes place in the so called "best" version of the 1st order Love's theories, see Budiansky & Sanders 1963. This theory is usually named: Budiansky-Sanders-Koiter theory and will be here named shortly: BSK theory.

The equations of equilibrium are encompassed by the variational equation

$$\int_\Omega (\mathbf{N}\cdot\boldsymbol{\gamma}(\mathbf{v},v) + \mathbf{M}\cdot\boldsymbol{\varkappa}(\mathbf{v},v))\,d\Omega = f(\mathbf{v},v) \qquad \forall\,(\mathbf{v},v)\in V(\Omega) \tag{40}$$

in which the strain measures $\boldsymbol{\gamma}(\mathbf{v},v)$, $\boldsymbol{\varkappa}(\mathbf{v},v)$ are defined in Budiansky & Sanders 1963, see also (Lewiński & Telega 2000, Secs. 16.2, 16.3).

The set of pairs $(\mathbf{N},\mathbf{M})$ satisfying this equation forms a set $\Sigma_0(\Omega)$ of statically admissible stress and couple resultants. The constitutive equations are decoupled, like in all 1st order Love's theories.

5.1 *The IMD method*

The fields $k(x)$ and $\mu(x)$ are design variables on Ω. The compliance is correctly expressed by (15), since the chosen theory satisfies all desired criteria of correctness. The minimum compliance problem (15) can be reduced to the problem (19), (20). Having found the minimizer $(\hat{\mathbf{N}},\hat{\mathbf{M}})$ we made up the solution by (22). The numerical method can be augmented by means of simultaneous analysis of the dual problem.

In order to construct the set $\Sigma_0(\Omega)$ one can make use of the stress functions representations which hold in the selected shell theories. Let $\epsilon^{\alpha\beta}$ be Ricci's pseudo–tensor referred to the basis $(\mathbf{g}_1,\mathbf{g}_2)$ on the middle surface. Let us express the stress and couple resultants in terms of new unknown fields $\boldsymbol{\psi} = (\psi_1,\psi_2)$, ψ: according to

$$\begin{aligned} N^{\alpha\beta} &= -\epsilon^{\alpha\nu}\epsilon^{\beta\mu}\varkappa_{\nu\mu}(\boldsymbol{\psi},\psi) \\ M^{\alpha\beta} &= \epsilon^{\alpha\nu}\epsilon^{\beta\mu}\gamma_{\nu\mu}(\boldsymbol{\psi},\psi) \end{aligned} \tag{41}$$

Substitution of these representations into the homogeneous equilibrium equations leads to identities. Thus, in the case of the load applied along the edges the formulae (41) determine the unknown fields $\mathbf{N}$, $\mathbf{M}$. If a surface load is applied, the formulae (41) should be complemented by particular solutions to the equilibrium equations but also here a special care is necessary, see Pietraszkiewicz (1968). Minimization over six fields $(\mathbf{N},\mathbf{M})\in\Sigma_0(\Omega)$ reduces to minimization over three fields ψ_1,ψ_2,ψ satisfying the boundary conditions, expressed now in terms of ψ_α,ψ and its derivatives along the loaded edges. Let us denote this set by $S(\Omega)$. Note that the fields of this set are not subject to differential constraints within the design domain.

Let us come back to the minimum compliance problem. By using (41) the complementary energy of the stress and couple resultants may be expressed in the form

$$\mathbf{N}\cdot(\mathbf{C}^{-1}\mathbf{N}) = \boldsymbol{\varkappa}\cdot(\mathbf{E}\boldsymbol{\varkappa}), \quad \mathbf{M}\cdot(\mathbf{C}^{-1}\mathbf{M}) = \boldsymbol{\gamma}\cdot(\mathbf{E}\boldsymbol{\gamma}) \tag{42}$$

where $\boldsymbol{\varkappa} = \boldsymbol{\varkappa}(\boldsymbol{\psi},\psi)$, $\boldsymbol{\gamma} = \boldsymbol{\gamma}(\boldsymbol{\psi},\psi)$ and the components of the tensor $\mathbf{E}$ in the basis $(\mathbf{g}_1,\mathbf{g}_2)$ are given by

$$E^{\alpha\beta\lambda\mu} = \epsilon^{\alpha\gamma}\epsilon^{\beta\delta}(\mathbf{C}^{-1})_{\gamma\delta\omega\varkappa}\epsilon^{\omega\lambda}\epsilon^{\varkappa\mu} \tag{43}$$

Let $\boldsymbol{\varkappa}^{(1)} = \boldsymbol{\varkappa}$, $\boldsymbol{\varkappa}^{(2)} = \frac{\sqrt{12}}{h}\boldsymbol{\gamma}$. The integrand of the compliance (14) is expressed as below

$$\frac{1}{h}\left[\boldsymbol{\varkappa}^{(1)}\cdot(\mathbf{E}\boldsymbol{\varkappa}^{(1)}) + \boldsymbol{\varkappa}^{(2)}\cdot(\mathbf{E}\boldsymbol{\varkappa}^{(2)})\right]. \tag{44}$$

If tensor $\mathbf{C}$ is isotropic, see (9), the components of $\boldsymbol{\Lambda}_1$, $\boldsymbol{\Lambda}_2$ refer to the basis $(\mathbf{g}_1,\mathbf{g}_2)$ of the curvilinear system with the metric tensor $(g_{\alpha\beta})$. Then

$$\boldsymbol{\varkappa}\cdot(\mathbf{E}\boldsymbol{\varkappa}) = \frac{1}{2k}\left(\frac{\operatorname{tr}\boldsymbol{\varkappa}}{\sqrt{2}}\right)^2 + \frac{1}{2\mu}||\operatorname{dev}\boldsymbol{\varkappa}||^2 \tag{45}$$

Thus the compliance of the shell can be expressed by

$$\wp(k,\mu)=\frac{1}{h}\min_{(\boldsymbol{\psi},\psi)\in S(\Omega)}\int_\Omega\sum_{\alpha=1}^{2}\varkappa^{(\alpha)}\cdot(\mathbf{E}\varkappa^{(\alpha)})d\Omega \quad (46)$$

where $\varkappa^{(\alpha)}$ depend on $\boldsymbol{\psi}$, ψ according to the definitions of the BSK theory.

Let us impose the isoperimetric condition (17) and consider the optimum design problem (18). Performing minimization over k and μ analytically, the auxiliary problem is obtained

$$Z_1=\min_{(\boldsymbol{\psi},\psi)\in S(\Omega)}\int_\Omega d\varrho_{\sqrt{2}}(\varkappa^{(1)},\varkappa^{(2)}) \quad (47)$$

with $\varkappa^{(1)}(\boldsymbol{\psi},\psi)=\varkappa(\boldsymbol{\psi},\psi)$, $\varkappa^{(2)}(\boldsymbol{\psi},\psi)=\frac{\sqrt{12}}{h}\boldsymbol{\gamma}(\boldsymbol{\psi},\psi)$ and $\varrho_{\sqrt{2}}(\cdot,\cdot)$ is given by (21). Let $(\hat{\boldsymbol{\psi}},\hat{\psi})$ be the minimizer of (47). The optimal moduli are expressed by

$$2\hat{k}(x)=\frac{\Lambda}{Z_1}\left[\sum_{\alpha=1}^{2}\left(\frac{\operatorname{tr}\varkappa^{(\alpha)}(\hat{\boldsymbol{\psi}}(x),\hat{\psi}(x))}{\sqrt{2}}\right)^2\right]^{\frac{1}{2}}$$
$$4\hat{\mu}(x)=\frac{\Lambda\sqrt{2}}{Z_1}\left[\sum_{\alpha=1}^{2}||\operatorname{dev}(\varkappa^{(\alpha)}(\hat{\boldsymbol{\psi}}(x),\hat{\psi}(x)))||^2\right]^{\frac{1}{2}} \quad (48)$$

where Z_1 is given by (47).

5.2 *The YMD method*

Assume that the material of the shell is transversely homogeneous and isotropic. The Poisson's ratio field $\nu(x)$ is given. The Young's modulus $E(x,x_3)=E(x)$ is subject to the isoperimetric constraint (27), where integration refers to the middle surface now. The tensor $\mathbf{C}$ is represented by (28). The shell is loaded along the edges and its compliance is expressed by (15) where dx is replaced by $d\Omega$. The field E_1 is the design variable, see (27). Let us consider the problem (29) referring now to the thin shell. Minimization over E_1 is done in the first step. We get (19) with Z_1 given by

$$Z_1=\min_{(\boldsymbol{\psi},\psi)\in S(\Omega)}\int_\Omega d\varrho_Y(\varkappa^{(1)}(\boldsymbol{\psi},\psi),\ \varkappa^{(2)}(\boldsymbol{\psi},\psi)) \quad (49)$$

where $\varrho_Y(\cdot,\cdot)$ is defined by (30). Let $(\hat{\boldsymbol{\psi}},\hat{\psi})$ be the minimizer of (49). The optimal Young's modulus is expressed by

$$\hat{E}(x)=\frac{\Lambda}{a(x)Z_1}\varrho_Y(\varkappa^{(1)}(\hat{\boldsymbol{\psi}}(x),\hat{\psi}(x)),\ \varkappa^{(2)}(\hat{\boldsymbol{\psi}}(x),\hat{\psi}(x))) \quad (50)$$

Let Ω_m be the support of $\hat{E}$. The minimizer $(\hat{\boldsymbol{\psi}},\hat{\psi})$ determines $\hat{\mathbf{K}}^{(\alpha)}$ and $\hat{\mathbf{N}}$, $\hat{\mathbf{M}}$ by (41). In the shell with the Young's modulus $\hat{E}$ there appear the stress and couple resultants $\check{\mathbf{N}}$, $\check{\mathbf{M}}$. These fields are minimizing (14) where $\mathbf{C}$ is expressed by $\hat{E}$ and a given field ν. Let us note that the integrand in (14) is expressed by

$$\frac{1}{\hat{E}_1(x)}\left[\varrho_Y(\mathbf{K}^{(1)},\mathbf{K}^{(2)})\right]^2 \quad (51)$$

with

$$\hat{E}_1=\alpha\varrho_Y(\hat{\mathbf{K}}^{(1)}(x),\ \hat{\mathbf{K}}^{(2)}(x)) \quad (52)$$

and $\alpha=\Lambda/Z_1$. Thus, the pair $(\check{\mathbf{K}}^{(1)},\check{\mathbf{K}}^{(2)})$ is the minimizer of the problem

$$h\alpha\wp^0=\min_{(\mathbf{K}^{(1)},\mathbf{K}^{(2)})\in\Sigma(\Omega)}\int_{\Omega_m}\frac{[\varrho_Y(\mathbf{K}^{(1)},\mathbf{K}^{(2)})]^2}{\hat{\varrho}_Y}d\Omega_m \quad (53)$$

with

$$\hat{\varrho}_Y=\varrho_Y(\hat{\mathbf{K}}^{(1)},\hat{\mathbf{K}}^{(2)}).$$

Let us prove that

$$\check{\mathbf{K}}^{(\alpha)}=\hat{\mathbf{K}}^{(\alpha)} \quad (54)$$

To this end we estimate the integral of $\varrho_Y=\varrho_Y(\mathbf{K}^{(1)},\mathbf{K}^{(2)})$ by using Cauchy-Schwarz inequality

$$\int_{\Omega_m}\varrho_Y d\Omega_m=\int_{\Omega_m}\frac{\varrho_Y}{\sqrt{\hat{\varrho}_Y}}\sqrt{\hat{\varrho}_Y}d\Omega_m\le$$
$$=\sqrt{\int_{\Omega_m}\frac{(\varrho_Y)^2}{\hat{\varrho}_Y}d\Omega_m}\sqrt{\int_{\Omega_m}\hat{\varrho}_Y d\Omega_m} \quad (55)$$

Hence

$$\int_{\Omega_m}\frac{(\varrho_Y)^2}{\hat{\varrho}_Y}d\Omega_m\ge\frac{\left(\int_\Omega\varrho_Y d\Omega_m\right)^2}{\int_\Omega\hat{\varrho}_Y d\Omega_m} \quad (56)$$

According to the choice of $(\hat{\mathbf{K}}^{(1)},\hat{\mathbf{K}}^{(2)})$ as the minimizer of the integral of $\varrho_Y(\mathbf{K}^{(1)},\mathbf{K}^{(2)})$ over $(\mathbf{K}^{(1)},\mathbf{K}^{(2)})\in\Sigma(\Omega)$ we estimate

$$\int_{\Omega_m}\varrho_Y(\mathbf{K}^{(1)},\mathbf{K}^{(2)})d\Omega_m\ge\int_{\Omega_m}\varrho_Y(\hat{\mathbf{K}}^{(1)},\hat{\mathbf{K}}^{(2)})d\Omega_m$$
$$=\int_{\Omega_m}\hat{\varrho}_Y d\Omega_m \quad (57)$$

Hence (56) implies

$$\int_{\Omega_m}\frac{(\varrho_Y)^2}{\hat{\varrho}_Y}d\Omega_m\ge\int_{\Omega_m}\hat{\varrho}_Y d\Omega_m \quad (58)$$

The equality is attained for $\varrho_Y=\hat{\varrho}_Y$. Thus, the minimum in (53) is attained if $\mathbf{K}^{(\alpha)}=\hat{\mathbf{K}}^{(\alpha)}$ and then (54) holds. The substitution of (54) into (53) gives

$$h\wp^0=\frac{1}{\alpha}\int_{\Omega_m}\hat{\varrho}_Y d\Omega=\frac{1}{\alpha}Z_1=\frac{1}{\Lambda}(Z_1)^2 \quad (59)$$

or (19) is confirmed. We conclude that the stress and couple resultants within the optimal shell are the same as those which solve the auxiliary problem

$$Z_1 = \min_{(\mathbf{N},\mathbf{M})\in\Sigma_0(\Omega)} \int_\Omega d\varrho_Y \left(\mathbf{N}, \frac{\sqrt{12}}{h}\mathbf{M}\right) \tag{60}$$

The pair of the fields: $(\hat{\mathbf{N}}, \hat{\mathbf{M}})$, the minimizer of (60), may concentrate on lines, which represents the reinforcing ribs. Thus the expression (60) encompasses the energy of ribs. Thus, the support of $(\hat{\mathbf{N}}, \hat{\mathbf{M}})$ determines: the shape of the middle surface as well as the position and shape of the reinforcing ribs.

The problem (60) should be solved simultaneously with its dual. The latter takes the form (25) where now $\varrho^*_{\sqrt{2}}(\cdot,\cdot)$ should be replaced by $\varrho^*_Y(\cdot,\cdot)$ see (32).

Let us compute the strains associated with $(\check{\mathbf{N}}, \check{\mathbf{M}})$. These strains appear in the optimal shell:

$$\check{\boldsymbol{\gamma}} = \frac{1}{h}\mathbf{C}^{-1}\hat{\mathbf{K}}^{(1)}, \qquad \check{\boldsymbol{\kappa}} = \frac{h}{\sqrt{12}}\check{\varkappa} = \frac{1}{h}\mathbf{C}^{-1}\hat{\mathbf{K}}^{(2)} \tag{61}$$

$$\hat{\mathbf{K}}^{(1)} = \check{\mathbf{N}}, \qquad \hat{\mathbf{K}}^{(2)} = \frac{\sqrt{12}}{h}\check{\mathbf{M}}$$

Thus, upon taking into account (28), (50) we arrive at the constitutive equations for the optimal shell

$$\check{\boldsymbol{\gamma}} = \frac{\Lambda}{hZ_1\varrho_Y(\hat{\mathbf{K}}^{(1)}, \hat{\mathbf{K}}^{(2)})}\mathbf{G}^{-1}\hat{\mathbf{K}}^{(1)}$$

$$\check{\boldsymbol{\kappa}} = \frac{\Lambda}{hZ_1\varrho_Y(\hat{\mathbf{K}}^{(1)}, \hat{\mathbf{K}}^{(2)})}\mathbf{G}^{-1}\hat{\mathbf{K}}^{(2)} \tag{62}$$

These strains are subject to the point-wise condition

$$\varrho^*_Y(\check{\boldsymbol{\gamma}}, \check{\boldsymbol{\kappa}}) = c, \qquad c = \frac{\Lambda}{hZ_1} \tag{63}$$

We conclude that the optimization process leads to making the strain distribution uniform in the norm $\varrho^*_Y(\cdot,\cdot)$.

Given $\hat{\mathbf{K}}^{(\alpha)}$ we may compute $(\check{\boldsymbol{\gamma}}, \check{\varkappa})$, but not vice versa. The equations (62) are non-invertible.

5.3 *The AMD design*

Let us consider the minimum compliance problem of thin shells formulated by (14) with $(\mathbf{N}, \mathbf{M})$ being stress and couple resultants in the thin shell; they satisfy the equilibrium equation (40), which will be written as $(\mathbf{N}, \mathbf{M}) \in \Sigma_0(\Omega)$. The compliance $\wp$ is considered a functional of argument $\mathbf{C}$; the tensor $\mathbf{C}$ is subject to Hooke's tensor symmetries, to the condition of positive semidefiniteness ($\mathbf{C} \geq \mathbf{0}$) and to the isoperimetric condition (6). Consider the problem

$$\wp^0 = \min\left\{\wp(\mathbf{C}) \;\middle|\; \mathbf{C}\in\mathbb{E}^4_s,\ \mathbf{C}\geq 0,\ \int_\Omega \operatorname{tr}\mathbf{C}d\Omega = \Lambda\right\} \tag{64}$$

where $\wp(\mathbf{C})$ is given by (14), and $(\mathbf{N}, \mathbf{M})$ satisfy (40). Czarnecki et al. (2014) proved that the compliance (64) is expressed by (19) with

$$Z_1 = \min_{(\mathbf{K}^{(1)},\mathbf{K}^{(2)})\in\Sigma(\Omega)} \int_\Omega d\varrho_A(\mathbf{K}^{(1)}, \mathbf{K}^{(2)}) \tag{65}$$

where

$$\varrho_A(\boldsymbol{\tau}^{(1)}, \boldsymbol{\tau}^{(2)}) = \sqrt{a_1(\boldsymbol{\tau}^{(1)}, \boldsymbol{\tau}^{(2)})} + \sqrt{a_2(\boldsymbol{\tau}^{(1)}, \boldsymbol{\tau}^{(2)})} \tag{66}$$

and $a_i(\boldsymbol{\tau}^{(1)}, \boldsymbol{\tau}^{(2)})$ is the i-th eigenvalue of the Gram matrix $[\boldsymbol{\tau}^{(\alpha)} \cdot \boldsymbol{\tau}^{(\beta)}]$. The norm (66) may be expressed via singular values

$$\varrho_A(\mathbf{K}^{(1)}, \mathbf{K}^{(2)}) = s_1(\mathbf{K}) + s_2(\mathbf{K}) \tag{67}$$

where $\mathbf{K}$ is formed by the columns $\mathbf{K}^{(\alpha)}$. The function (67) is so called Schatten's 1-norm of matrix $\mathbf{K}$. We know from algebra that the norm dual to the Schatten's 1-norm (67) is expressed as below

$$\varrho^*_A(\boldsymbol{\varepsilon}^{(1)}, \boldsymbol{\varepsilon}^{(2)}) = \max\{s_1(\boldsymbol{\varepsilon}), s_2(\boldsymbol{\varepsilon})\} \tag{68}$$

where $\boldsymbol{\varepsilon}$ is formed by columns: $\boldsymbol{\varepsilon}^{(\alpha)}$.

Thus we conclude that the problem dual to (65) assumes the form

$$Z_2 = \max\{f(\mathbf{v}, v) \mid (\mathbf{v}, v) \in V(\Omega), \\ \varrho^*_A(\boldsymbol{\gamma}(\mathbf{v}, v), \boldsymbol{\kappa}(\mathbf{v}, v)) \leq 1\} \tag{69}$$

The maximization operation chooses the greatest singular value. The result (68), (69) complements the discussion in Czarnecki et al. (2014). The proof of the equality $Z_1 = Z_2$ is neglected here. The problem (69) may be regarded as a counterpart of the problem (29) in Gaile et al. (2009).

The minimizer $(\hat{\mathbf{K}}^{(1)}, \hat{\mathbf{K}}^{(2)})$ of the problem (65) determines the tensor field $\hat{\mathbf{C}}$. Its eigenvalues are expressed by Eqs (18) in Czarnecki et al. (2014). One of the eigenvalues vanishes, which is the consequence of considering a single load condition only.

6 FINAL REMARKS

The compliance minimization problem of thin shells leads to the auxiliary minimization problem (20) and to its dual form (25) involving maximization operation. Both the problems are counterparts of the celebrated Michell's problem of weight minimization. Solving these problems we determine the material domain which is cut out from the design domain. This method paves the way towards 3D printing of the specimens of small dimensions, see Smith et al. (2016).

ACKNOWLEDGEMENT

The paper was prepared within the Research Grant no 2013/11/B/ST8/04436 financed by the National Science Centre (Poland), entitled: Topology optimization of engineering structures. An approach synthesizing the methods of: free material design, composite design and Michell-like trusses.

REFERENCES

Allaire, G. (2002). *Shape optimization by the homogenization method*. New York: Springer.

Bendsøe, M.P., J.M. Guedes, R.B. Haber, P. Pedersen, & J.E. Taylor (1994). An Analytical Model to Predict Optimal Material Properties in the Context of Optimal Structural Design. *Journal of Applied Mechanics. Transactions of ASME. 61 (4)*, 930–937.

Bouchitté, G. & G. Buttazzo (2001). Characterization of optimal shapes and masses through Monge-Kantorovich equation. *Journal of European Mathematical Society. 3*, 139–168.

Bouchitté, G., W. Gangbo, & P. Seppecher (2008). Michell trusses and lines of principal action. *Mathematical Models and Methods in Applied Sciences. 18 (9)*, 1571–1603.

Budiansky, B. & J.L. Sanders (1963). On the "best" first-order linear shell theory. In: *Progress in Applied Mechanics. The Prager Anniversary Volume*, 129–140. New York: The Macmillan Co.

Cherkaev, A.V. (2000). *Variational Methods for Structural Optimization*. New York: Springer.

Ciarlet, Ph. & E. Sanchez-Palencia (1996). An existence and uniqueness theorem for the two-dimensional linear membrane shell equations. *Journal de Mathematiques Pures et Appliquées. 75*, 51–67.

Czarnecki, S. (2015). Isotropic material design. *Computational Methods in Science and Technology. 21*, 49–64.

Czarnecki, S., R. Czubacki, G. Dzierżanowski & T. Lewiński (2014). The Free Material Design of Thin Elastic Shells. In *W. Pietraszkiewicz & J. Górski (eds), Shell Structures: Theory and Applications. Vol. 3. Proc. of the 10th SSTA Conference, Gdańsk*, 16–18. *October 2013*, 73–76. London:. CRC Press, Taylor& Francis/Balkema.

Czarnecki, S. & T. Lewiński (2013). On minimum compliance problems of thin elastic plates of varying thickness. *Structural and Multidisciplinary Optimization. 48*, 17–31.

Czarnecki, S. & T. Lewiński (2014). A stress-based formulation of the free material design problem with the trace constraint and multiple load conditions. *Structural and Multidisciplinary Optimization. 49*, 707–731.

Czarnecki S. & T. Lewiński (2017). On material design by the optimal choice of Young's modulus distribution. *International Journal of Solids and Structures. 110–111*, 315–331.

Czarnecki, S. & P. Wawruch (2015). The emergence of auxetic material as a result of optimal isotropic design. *Physica Status Solidi (B). 252*, 1–11.

Czubacki, R. & T. Lewiński (2015). Topology optimization of spatial continuum structures made of non-homogeneous material of cubic symmetry. *Journal of Mechanics of Materials and Structures. 10*, 519–535.

Dzierżanowski, G. (2012). Stress energy minimization as a tool in the material layout design of shallow shells. *International Journal of Solids and Structures. 49*, 1343–1354.

Gaile, S., G. Leugering, & M. Stingl (2009). Free Material Optimization for Plates and Shells, In: A. Korytowski et al. (eds.): *System Modeling and Optimization, IFIP AICT. 31*, 239–250. Berlin: Springer.

Gilbert, M. & A. Tyas (2003). Layout optimization of large-scale pin-jointed frames. *Engineering Computations. 20*, 1044–1064.

Gol'denveizer, A.L. (1976). *Theory of elastic thin shells*. Moscow: Nauka (in Russian).

Kobelev, V. (2016). The extreme property of twisted spherical shell. *Structural and Multidisciplinary Optimization. 53*, 123–127.

Lewiński, T. (2004a). Michell structures formed on surfaces of revolution. *Structural and Multidisciplinary Optimization. 28*, 20–30.

Lewiński, T. (2004b). Homogenization and optimal design in structural mechanics, In P.P. Castañeda, J.J. Telega & B. Gambin (Eds.), *Nonlinear homogenization and its application to composites, polycrystals and smart materials, NATO Science Series II, Mathematics, Physics and Chemistry. 170*: 139–168, Dordrecht: Kluwer.

Lewiński, T. & J.J. Telega (2000). *Plates, laminates and shells. Asymptotic analysis and homogenization*. Singapore-New Jersey-London-Hong Kong: World Scientific Publishing.

Mazurkiewicz, Z. (2004). *Thin elastic shells. Linear theory.* Warszawa: Warsaw University of Technology Publishing House. (in Polish).

Michell, A.G.M. (1904). The limits of economy of material in frame structures. *Philosophical Magazine. 8 (47)*, 589–597.

Naghdi, P.M. (1963). Foundation of elastic shell theory. In: I.N. Sneddon & R. Hill (eds). *Progress in Solid Mechanics. 4*, 2–90. Amsterdam: North Holland.

Pietraszkiewicz, W. (1968). Multivalued stress functions in the linear theory of shells. *Archives of Mechanics. 20*, 37–45.

Pritchard, T.J., M. Gilbert & A. Tyas, (2005). *Plastic layout optimization of large-scale frameworks subject to multiple load cases, member self-weight and with joint length penalties*. Proc. 6th World Congress of Structural and Multidisciplinary Optimization, Rio de Janeiro, 30 May–3 June, Brazil (CD-ROM).

Rozvany, G.I.N., (1976). *Optimal design of flexural systems*. London: Pergamon Press.

Smith, C.J., M. Gilbert, I. Todd, & F. Dergutti (2016). Application of layout optimization to the design of additively manufactured metallic components. *Structural and Multidisciplinary Optimization. 54*, 1297–1313.

Sokół, T. (2011). A 99 line code for discretized Michell truss optimization written in Mathematica. *Structural and Multidisciplinary Optimization. 43*, 181–190.

Sokół, T. (2016). *A new adaptive ground structure method for multi-load spatial Michell structures*, 525–528. *In M. Kleiber, T. Burczyński, K. Wilde, J. Górski, K. Winkelmann, Ł. Smakosz (Eds), Advances in Mechanics: Theoretical, Computational and Interdisciplinary Issues*, CRC Press.

Strang, S. & R.V. Kohn (1983). Hencky-Prandtl nets and constrained Michell trusses. *Computer Methods in Applied. Mechanics and Engineering. 36*, 207–222.

Vekua, I.N. (1982). *Selected general methods of construction of various types of shell theories*. Moscow: Nauka (in Russian).

Weldeysus, A.G. & M. Stolpe (2016). Free material optimization for laminated plates and shells. *Structural and Multidisciplinary Optimization. 53*, 1335–1347.

Zegard, T. & G.H. Paulino (2015). GRAND-3 – Ground structure based topology optimization for arbitrary 3D domains using MATLAB. *Structural and Multidisciplinary Optimization. 52*, 1161–1184.

Taylor & Francis
Taylor & Francis Group
http://taylorandfrancis.com

Shell Structures: Theory and Applications Volume 4 – Pietraszkiewicz & Witkowski (eds)
© 2018 Taylor & Francis Group, London, ISBN 978-1-138-05045-7

Solid-shell formulations based on reduced integration—investigations of anisotropic material behaviour, large deformation problems and stability

S. Reese, O. Barfusz, M. Schwarze & J.-W. Simon
Institute of Applied Mechanics, RWTH Aachen University, Aachen, Germany

ABSTRACT: In the paper, a solid-shell finite element is proposed for composite structures consisting of woven fabrics, with two families of fibres, embedded in a matrix material. It is particularly suited for application to thin shell structures curing locking phenomena by implementing both the EAS and the ANS concept. Moreover, using reduced integration with hourglass stabilization leads to high computational efficiency, still representing satisfactorily the through-the-thickness stress distribution, since the number of integration points can be chosen arbitrarily. Orthotropic material behaviour is incorporated by means of a micromechanically motivated model, which is based on structural tensors representing different fibre orientations.

1 INTRODUCTION

Composite materials are very promising in lightweight structures due to their very high stiffness and low density at the same time. They consist e.g. of multi-layered fabric embedded in a matrix material. The fabric is usually woven out of glass, aramide or carbon fibres, whereas the matrix is made of thermoplastics or thermosets. In addition, in aerospace structures one can find metal matrices or ceramics which can be used for both fibres and matrices. Besides the anisotropic structure, the stress-strain behaviour of fibre composite materials is highly non-linear. Moreover, the material response in tension and compression differs significantly.

Models for anisotropic material behaviour at finite strains have been developed mostly in the field of biomechanics. For instance, in (Holzapfel, Eberlein, Wriggers, & Weizsäcker 1996) the authors investigate axisymmetric orthotropic blood vessels, whereas biological soft tissues are modelled in (Weiss, Maker, & Govindjee 1996) based on an incompressible transversely isotropic law for moderate deformations. The transversely isotropic behaviour of rubber is described in (Rüter & Stein 2000), and orthotropic constitutive equations are presented in (Bonet & Burton 1998) for the simulation of human leg impact problems. In the paper we use a modification of the micromechanically motivated model proposed in (Reese, Raible, & Wriggers 2001) and (Reese 2003). Therein, an anisotropic model has been presented for the hyperelastic material behaviour of pneumatic membranes reinforced with woven fibres which is particularly suitable for the fibre reinforced composites considered here.

The introduction of fully three-dimensional material models is not straightforward in classical shell formulations because of the assumption of plane stress. Even though there exist shell formulations which take into account the through-the-thickness stretching, see e.g. (Bischoff & Ramm 1997, Brank, Korelc, & Ibrahimbegović 2002, Cardoso & Yoon 2005) as well as (Klinkel, Gruttmann, & Wagner 2008, Kim & Bathe 2008), the implementation of three-dimensional material models is much simpler in the context of solid elements. On the other hand, it is a well-known fact that solid elements provide a poor performance when being applied to thin shell-like structures. In particular, there are different locking phenomena which cause overestimation of the stress state and underestimation of the deformation.

One possible strategy to deal with this problem is to use solid-shells which combine the advantages of both solid elements and shell elements at the same time. These allow for displaying realistically the three-dimensional geometry and enable the definition of surface friction, while still providing the suitable shape for thin structures in accordance to shell elements. To eliminate volumetric locking in the case of (nearly) incompressible materials as well as the Poisson thickness locking due to the non-constant distribution of transverse normal strain over the thickness in bending problems of shell-like structures, the enhanced assumed strain (EAS) concept is used. In the literature, several solid-shell formulations incorporating the EAS concept have been presented, see e.g. (Vu-Quoc & Tan 2003, Valente, Sousa, & Jorge 2004) Alves de Sousa, Cardoso, Fontes Valente, Yoon, Grácio, & Natal Jorge 2006) as well as in (Reese 2007) to name only a few.

To cure the transverse shear locking which is present in standard eight-node hexahedral elements, the assumed natural strain (ANS) method is applied. In the context of full integration formulations the ANS method can be found e.g. in (Vu-Quoc & Tan 2003, Kim, Liu, & Han 2005, Klinkel, Gruttmann, & Wagner 2006) and for reduced

integration solid-shell formulations e.g. in (Cardoso, Yoon, Mahardika, Choudhry, Alves de Sousa, & Fontes Valente 2008, Schwarze & Reese 2009, Schwarze & Reese 2011, Schwarze, Vladimirov, & Reese 2011). Note, that the hourglass stabilization is also formulated in such a way, that neither volumetric nor transversal shear locking occur.

2 ANISOTROPIC MATERIAL MODEL

The fibre composites considered here are composed of several layers, each layer consists of a woven fabric embedded in a matrix material. In order to describe the anisotropic material behaviour on a phenomenological level, we adopt a micro-mechanically motivated model proposed in (Reese, Raible, & Wriggers 2001). The basic equations of the continuum model are summarized in the following. The material parameters are chosen such that the behaviour of carbon fibers embedded in an epoxy resin matrix is approximately represented.

2.1 *Concept of structural tensors*

Introducing the deformation gradient $\mathbf{F}$, deformation of a continuous body is represented by the right Cauchy-Green tensor

$$\mathbf{C} = \mathbf{F}^{\mathrm{T}}\mathbf{F} \tag{1}$$

The characterization of a hyperelastic body is then given by the existence of a scalar potential which is the stored energy function $\psi = \psi(\mathbf{C})$, such that

$$\mathbf{S} = 2\,\frac{\partial \psi(\mathbf{C})}{\partial \mathbf{C}} \tag{2}$$

is the second Piola-Kirchhoff stress tensor. In the case of orthotropic material behaviour, the energy function $\psi(\mathbf{C})$ reduces to an isotropic function of $\mathbf{C}$ and the structural tensors $\mathbf{M}_1$ and $\mathbf{M}_2$ which are defined by

$$\mathrm{M}_1 = \boldsymbol{n}_1 \otimes \boldsymbol{n}_1 \qquad \text{and} \qquad \mathrm{M}_2 = \boldsymbol{n}_2 \otimes \boldsymbol{n}_2 \tag{3}$$

where the vectors $\boldsymbol{n}_1$ and $\boldsymbol{n}_2$ are oriented parallel to the fibres, see Figure 1.

For a discussion of the theoretical background we refer to (Svendsen 1994) and the references therein.

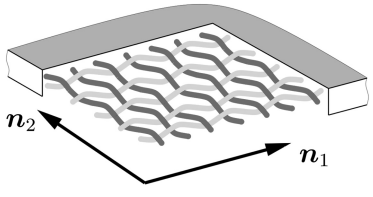

Figure 1. Fabric structure with vectors $\boldsymbol{n}_1$ and $\boldsymbol{n}_2$.

The strain energy function ψ can be represented by the following invariants:

$$I_1 = \mathrm{tr}\ \mathbf{C} \tag{4a}$$

$$I_2 = \frac{1}{2}\left[(\mathrm{tr}\ \mathbf{C})^2 - \mathrm{tr}\left(\mathbf{C}^2\right)\right] \tag{4b}$$

$$I_3 = \det \mathbf{C} \tag{4c}$$

$$I_4 = \mathrm{tr}\left(\mathbf{C}\,\mathbf{M}_1\right) \qquad I_5 = \mathrm{tr}\left(\mathbf{C}^2\,\mathbf{M}_1\right) \tag{4d}$$

$$I_6 = \mathrm{tr}\left(\mathbf{C}\,\mathbf{M}_2\right) \qquad I_7 = \mathrm{tr}\left(\mathbf{C}^2\,\mathbf{M}_2\right) \tag{4e}$$

2.2 *Strain energy function*

The proposed model from (Reese, Raible, & Wriggers 2001) covers different situations:

- in the small strain regime, due to the woven microstructure, the fibres are not pulled straight. Then the influence of the fibres is not considered. In this case, the material behaviour is isotropic.
- for compression in fibre direction, the fibre buckles. Its influence on the mechanical behaviour is not considered too.
- compression in one direction and tension in the other one, the material can be considered to be transversely isotropic.
- tension in both directions, the behaviour is predominated by the fibres.

Nevertheless, we consider the carbon fibres being embedded, such that the matrix acts as an elastic continuous support. Thus, in the current implementation it is assumed that the fibres influence the overall behaviour in the compression case as well. Except of this, we adopt the mentioned model and use the following strain energy function:

$$\begin{aligned}\psi \ &= \psi_{NH}(I_1, I_3) + \psi^{+}_{iso}(I_1, I_2) \\ &\quad + \psi_{ani}(I_4, I_5, I_6, I_7)\end{aligned} \tag{5}$$

Here, ψ_{NH} denotes the Neo-Hookean part displaying the isotropic case. The corresponding strain energy function is given by

$$\begin{aligned}\psi_{NH} \ &= \frac{\mu}{2}\,(I_1 - 3) - \mu \ln \sqrt{I_3} \\ &\quad + \frac{\Lambda}{4}\left(I_3 - 1 - 2\ln\sqrt{I_3}\right),\end{aligned} \tag{6}$$

where μ and Λ are the Lamé parameters. If incompressibility is assumed, Λ remains undetermined. Since even in the isotropic case the stiffening in the large strain regime cannot be captured by this, we add an additional term

$$\psi^{+}_{iso} \ = \ K_1^{iso}\,(I_1 - 3)^{\alpha_1} + K_2^{iso}\,(I_2 - 3)^{\alpha_2} \tag{7}$$

The anisotropic behaviour of the fabric is introduced by the part

$$\begin{aligned}\psi_{ani} &= K_1^{ani\,1}\,(I_4-1)^{\beta_1} + K_2^{ani\,1}\,(I_5-1)^{\beta_2} \\ &+ K_1^{ani\,2}\,(I_6-1)^{\gamma_1} + K_2^{ani\,2}\,(I_7-1)^{\gamma_2} \\ &+ K^{coup\,ani}\,(I_4-1)^{\xi}(I_6-1)^{\xi}\end{aligned} \tag{8}$$

Note that in (Reese, Raible, & Wriggers 2001) further coupling terms have been introduced. However, the latter could be shown to have almost no influence in the computer experiments. Thus, they are neglected from the beginning. The model includes 16 material parameters (15 in the case of incompressibility). In order to ensure that neither the stress tensor $\mathbf{S}$ nor the material tensor $\mathcal{L} = 4\,\frac{\partial^2\psi}{\partial\mathbf{C}^2}$ contain any undetermined values, all exponents $\alpha_i, \beta_i, \gamma_i, \xi\,(i=1,2)$ are chosen to be integers larger than 2.

2.3 *Reduction to orthotropic linear hyperelasticity*

In order to reduce the proposed model to the case of orthotropic linear hyperelasticity, we require the second Piola-Kirchhoff stress tensor $\mathbf{S}$ obtained from (2) to be linear in $\mathbf{C}$. Note, that the restriction to linear elasticity weakens the aforementioned constraints for the exponents in the strain energy function ψ_{lin} which are chosen to take the following values:

$$\begin{aligned}&\alpha_1 = 2 \quad \alpha_2 = 1 \quad \beta_1 = 2 \quad \beta_2 = 1 \\ &\gamma_1 = 2 \quad \gamma_2 = 1 \quad \xi = 1\end{aligned} \tag{9}$$

In order to obtain a stress-free undeformed state, the terms

$$\Delta\psi_{iso}^{+} = -2K_2^{iso}\,(I_1-3) \tag{10}$$

$$\Delta\psi_{ani} = -4K_2^{ani\,1}\,(I_4-1) - 4K_2^{ani\,2}\,(I_6-1) \tag{11}$$

must be added to the strain energy function. Finally, the linear model reads

$$\begin{aligned}\psi_{lin} &= K_1^{iso}\,(I_1-3)^2 \\ &+ K_2^{iso}\,(I_2-3-2\,(I_1-3)) \\ &+ K_1^{ani\,1}\,(I_4-1)^2 \\ &+ K_2^{ani\,1}\,(I_5-1-4\,(I_4-1)) \\ &+ K_1^{ani\,2}\,(I_6-1)^2 \\ &+ K_2^{ani\,2}\,(I_7-1-4\,(I_6-1)) \\ &+ K^{coup\,ani}\,(I_4-1)(I_6-1)\end{aligned} \tag{12}$$

Further, comparison with isotropic linear elasticity yields the following relations:

$$K_1^{iso} = -\frac{\mu}{2} \qquad K_2^{iso} = \frac{1}{8}\,(\Lambda + 2\,\mu) \tag{13}$$

3 SOLID-SHELL FORMULATION

The implementation of the described three-dimensional material model into classical shell elements is not straightforward, because these usually assume plane stress. On the other hand, using standard solid elements requires a fine discretization to predict the stress distribution with sufficient accuracy. In fact, it is not even clear whether or not the converged solution using solid elements is equal to the solution using shell elements. This holds especially in case of thin structures, where locking phenomena often occur. To overcome different types of locking and to achieve efficient computations, we use the solid-shell concept. The one, based on the works of (Reese 2007, Schwarze & Reese 2011, Schwarze, Vladimirov, & Reese 2011) is chosen here.

Moreover, the use of the solid-shell formulation enables to choose arbitrarily many Gauss points over the shell thickness. Since the material parameters can be defined for each Gauss point separately, this concept provides an easy way to deal with layers of different fibre orientations.

3.1 *Finite element framework and interpolation*

The solid-shell concept is based on the well known two-field variational functional

$$\mathrm{g}_1(\mathbf{u}, \mathbf{E}_\mathrm{e}) = \int_{\mathrm{B}_0} \mathbf{S}(\mathbf{E}) : \delta\mathbf{E}_\mathrm{c}\,\mathrm{dV} + \mathrm{g}_{\mathrm{ext}} = 0 \tag{14}$$

$$\mathrm{g}_2(\mathbf{u}, \mathbf{E}_\mathrm{e}) = \int_{\mathrm{B}_0} \mathbf{S}(\mathbf{E}) : \delta\mathbf{E}_\mathrm{e}\,\mathrm{dV} = 0 \tag{15}$$

where g_{ext} denotes the virtual work of the external loading. The total Green-Lagrange strain tensor $\mathbf{E}$ is split additively into a compatible part $\mathbf{E}_\mathrm{c}$ and an enhanced part $\mathbf{E}_\mathrm{e}$ based on the EAS concept:

$$\mathbf{E} = \mathbf{E}_\mathrm{c} + \mathbf{E}_\mathrm{e} \tag{16}$$

Considering a standard eight-node hexahedral finite element based on the isoparametric concept, the position vector of the reference configuration $\mathbf{X}(\boldsymbol{\xi}) = [\mathrm{X}_1, \mathrm{X}_2, \mathrm{X}_3]^\mathrm{T}$ and the displacement vector $\mathbf{U}(\boldsymbol{\xi}) = [\mathrm{U}_1, \mathrm{U}_2, \mathrm{U}_3]^\mathrm{T}$ can be approximated by

$$\mathrm{X_i} = \sum_{\mathrm{I}=1}^{8} \mathrm{N_I}\,\mathrm{X_{iI}} \quad (\mathrm{i} = 1,2,3) \tag{17}$$

$$\mathrm{U_i} = \sum_{\mathrm{I}=1}^{8} \mathrm{N_I}\,\mathrm{U_{iI}} \quad (\mathrm{i} = 1,2,3) \tag{18}$$

respectively, using tri-linear shape functions

$$\begin{aligned}N_I &= 1/8(1+\xi_I\xi)(1+\eta_I\eta)(1+\zeta_I\zeta) \\ &\qquad (I = 1, \ldots, 8)\end{aligned} \tag{19}$$

The position vector of the current (deformed) configuration reads

$$\mathbf{x}(\boldsymbol{\xi}) = \mathbf{X}(\boldsymbol{\xi}) + \mathbf{U}(\boldsymbol{\xi}) \tag{20}$$

Then, introducing the displacement gradient $\mathbf{D} = \partial\mathbf{U}/\partial\boldsymbol{\xi}$, the Jacobian matrices $\mathbf{J}$ and $\tilde{\mathbf{J}}$ of the reference and the current configuration, respectively, can be written as follows:

$$\mathbf{J} = \frac{\partial \mathbf{X}}{\partial \boldsymbol{\xi}} = [\mathbf{J}_1, \mathbf{J}_2, \mathbf{J}_3] \tag{21}$$

$$\tilde{\mathbf{J}} = \frac{\partial \mathbf{x}}{\partial \boldsymbol{\xi}} = \mathbf{J} + \mathbf{D} = \left[\tilde{\mathbf{J}}_1, \tilde{\mathbf{J}}_2, \tilde{\mathbf{J}}_3\right] \tag{22}$$

The columns of $\mathbf{J}$ and $\tilde{\mathbf{J}}$ represent the covariant base vectors with respect to the reference and current configuration, respectively.

It is a crucial point of the finite element formulation that the hourglass stabilization part can be computed analytically. For this purpose the inverse of the Jacobian matrix must have polynomial form. Furthermore earlier investigations have shown that it is not sufficient to work with the center part of $\mathbf{J}$. The incorporation of the linear and bilinear terms enables to reduce mesh distortion sensitivity. Hence we consider the polynomial form of the Jacobian matrices defined in (21), which can be obtained by

$$\begin{aligned}\mathbf{J} &= \mathbf{J}^0 + \xi\,\mathbf{J}^\xi + \eta\,\mathbf{J}^\eta + \zeta\,\mathbf{J}^\zeta \\ &\quad + \xi\eta\,\mathbf{J}^{\xi\eta} + \eta\zeta\,\mathbf{J}^{\eta\zeta} + \xi\zeta\,\mathbf{J}^{\xi\zeta}\end{aligned} \tag{23}$$

$$\begin{aligned}\mathbf{D} &= \mathbf{D}^0 + \xi\,\mathbf{D}^\xi + \eta\,\mathbf{D}^\eta + \zeta\,\mathbf{D}^\zeta \\ &\quad + \xi\eta\,\mathbf{D}^{\xi\eta} + \eta\zeta\,\mathbf{D}^{\eta\zeta} + \xi\zeta\,\mathbf{D}^{\xi\zeta}\end{aligned} \tag{24}$$

The contravariant base vectors with respect to the initial configuration and the current configuration are denoted by

$$\mathbf{H}_\mathrm{i} = \frac{\partial \xi_\mathrm{i}}{\partial \mathrm{X}_\mathrm{j}}\,\mathbf{e}_\mathrm{j} = \mathrm{j}_{\mathrm{ij}}\,\mathbf{e}_\mathrm{j} \quad \text{and} \quad \tilde{\mathbf{H}}_\mathrm{i} = \frac{\partial \xi_\mathrm{i}}{\partial \mathrm{x}_\mathrm{j}}\,\mathbf{e}_\mathrm{j} = \tilde{\mathrm{j}}_{\mathrm{ij}}\,\mathbf{e}_\mathrm{j} \tag{25}$$

These represent the rows of the inverse Jacobian matrices $\mathbf{J}^{-1}$ and $\tilde{\mathbf{J}}^{-1}$, respectively, the coefficients of which are denoted by $j_{ij} = (\mathbf{J}^{-1})_{ij}$ and $\tilde{j}_{ij} = (\tilde{\mathbf{J}}^{-1})_{ij}$.

With this definition, the Green-Lagrange strain tensor can be written in terms of its cartesian and covariant components E_{ij} and $\bar{\mathrm{E}}_{ij} = E_{\xi_i\xi_j}$, respectively,

$$\mathbf{E} = \mathrm{E}_{\mathrm{ij}}\,\mathbf{e}_\mathrm{i} \otimes \mathbf{e}_\mathrm{j} = \bar{\mathrm{E}}_{\mathrm{ij}}\,\mathbf{H}_\mathrm{i} \otimes \mathbf{H}_\mathrm{j} \tag{26}$$

Denoting the Voigt notation by $(\hat{\bullet})$ and exploiting symmetry as well as $\boldsymbol{\Gamma}_{\mathrm{ij}} = 2\mathrm{E}_{\mathrm{ij}}$, the latter can be stored into the 6×1 vectors

$$\hat{\mathbf{E}} = \{E_{11},\, E_{22},\, E_{33},\, \Gamma_{12},\, \Gamma_{23},\, \Gamma_{13}\}^T \tag{27}$$

$$\hat{\bar{\mathbf{E}}} = \{E_{\xi\xi},\, E_{\eta\eta},\, E_{\zeta\zeta},\, \Gamma_{\xi\eta},\, \Gamma_{\eta\zeta},\, \Gamma_{\xi\zeta}\}^T \tag{28}$$

The two vectors can be transformed into each other by means of the relation

$$\hat{\mathbf{E}} = \mathbf{T}\,\hat{\bar{\mathbf{E}}}, \tag{29}$$

where

$$\mathbf{T} = \tag{30}$$

$$\begin{bmatrix}
\mathrm{j}_{11}^2 & \mathrm{j}_{21}^2 & \mathrm{j}_{31}^2 & \mathrm{j}_{11}\mathrm{j}_{21} & \mathrm{j}_{21}\mathrm{j}_{31} & \mathrm{j}_{11}\mathrm{j}_{31} \\
\mathrm{j}_{12}^2 & \mathrm{j}_{22}^2 & \mathrm{j}_{32}^2 & \mathrm{j}_{12}\mathrm{j}_{22} & \mathrm{j}_{22}\mathrm{j}_{32} & \mathrm{j}_{12}\mathrm{j}_{32} \\
\mathrm{j}_{13}^2 & \mathrm{j}_{23}^2 & \mathrm{j}_{33}^2 & \mathrm{j}_{13}\mathrm{j}_{23} & \mathrm{j}_{23}\mathrm{j}_{33} & \mathrm{j}_{13}\mathrm{j}_{33} \\
2\mathrm{j}_{11}\mathrm{j}_{12} & 2\mathrm{j}_{21}\mathrm{j}_{22} & 2\mathrm{j}_{31}\mathrm{j}_{32} & \mathrm{j}_{12}\mathrm{j}_{21}+\mathrm{j}_{11}\mathrm{j}_{22} & \mathrm{j}_{22}\mathrm{j}_{31}+\mathrm{j}_{21}\mathrm{j}_{32} & \mathrm{j}_{12}\mathrm{j}_{31}+\mathrm{j}_{11}\mathrm{j}_{32} \\
2\mathrm{j}_{12}\mathrm{j}_{13} & 2\mathrm{j}_{22}\mathrm{j}_{23} & 2\mathrm{j}_{32}\mathrm{j}_{33} & \mathrm{j}_{13}\mathrm{j}_{22}+\mathrm{j}_{12}\mathrm{j}_{23} & \mathrm{j}_{23}\mathrm{j}_{32}+\mathrm{j}_{22}\mathrm{j}_{33} & \mathrm{j}_{13}\mathrm{j}_{32}+\mathrm{j}_{12}\mathrm{j}_{33} \\
2\mathrm{j}_{11}\mathrm{j}_{13} & 2\mathrm{j}_{21}\mathrm{j}_{23} & 2\mathrm{j}_{31}\mathrm{j}_{33} & \mathrm{j}_{13}\mathrm{j}_{21}+\mathrm{j}_{11}\mathrm{j}_{23} & \mathrm{j}_{23}\mathrm{j}_{31}+\mathrm{j}_{21}\mathrm{j}_{33} & \mathrm{j}_{13}\mathrm{j}_{31}+\mathrm{j}_{11}\mathrm{j}_{33}
\end{bmatrix}$$

is the 6×6 transformation matrix, which includes the coefficients of the inverse Jacobian matrix $\mathbf{J}^{-1}$ with respect to the reference configuration.

3.2 *Green-Lagrange strain field*

Therewith, the compatible Green-Lagrange strain can be written in the form $\hat{\mathbf{E}}_\mathrm{c} = \mathbf{T}\hat{\bar{\mathbf{E}}}_\mathrm{c}$. In order to obtain the components of the compatible Green-Lagrange strain tensor $\hat{\bar{\mathbf{E}}}_\mathrm{c}$ in polynomial form, the Jacobian matrix $\mathbf{J}$ and the displacement gradient $\mathbf{D}$ are split as follows:

$$\mathbf{J}_1 = \mathbf{J}_1^0 + \eta\,\mathbf{J}_1^\eta + \zeta\,\mathbf{J}_1^\zeta + \eta\zeta\,\mathbf{J}_1^{\eta\zeta} \tag{31a}$$

$$\mathbf{J}_2 = \mathbf{J}_2^0 + \xi\,\mathbf{J}_2^\xi + \zeta\,\mathbf{J}_2^\zeta + \xi\zeta\,\mathbf{J}_2^{\xi\zeta} \tag{31b}$$

$$\mathbf{J}_3 = \mathbf{J}_3^0 + \xi\,\mathbf{J}_3^\xi + \eta\,\mathbf{J}_3^\eta + \xi\eta\,\mathbf{J}_3^{\xi\eta} \tag{31c}$$

$$\mathbf{D}_1 = \mathbf{D}_1^0 + \eta\,\mathbf{D}_1^\eta + \zeta\,\mathbf{D}_1^\zeta + \eta\zeta\,\mathbf{D}_1^{\eta\zeta} \tag{32a}$$

$$\mathbf{D}_2 = \mathbf{D}_2^0 + \xi\,\mathbf{D}_2^\xi + \zeta\,\mathbf{D}_2^\zeta + \xi\zeta\,\mathbf{D}_2^{\xi\zeta} \tag{32b}$$

$$\mathbf{D}_3 = \mathbf{D}_3^0 + \xi\,\mathbf{D}_3^\xi + \eta\,\mathbf{D}_3^\eta + \xi\eta\,\mathbf{D}_3^{\xi\eta} \tag{32c}$$

Hence, the covariant compatible Green-Lagrange strain components are given by

$$\mathrm{E}_{\mathrm{c}\,\xi\xi} = \mathbf{J}_1^\mathrm{T}\mathbf{D}_1 + 1/2\,\mathbf{D}_1^\mathrm{T}\mathbf{D}_1 \tag{33a}$$

$$\mathrm{E}_{\mathrm{c}\,\eta\eta} = \mathbf{J}_2^\mathrm{T}\mathbf{D}_2 + 1/2\,\mathbf{D}_2^\mathrm{T}\mathbf{D}_2 \tag{33b}$$

$$\mathrm{E}_{\mathrm{c}\,\zeta\zeta} = \mathbf{J}_3^\mathrm{T}\mathbf{D}_3 + 1/2\,\mathbf{D}_3^\mathrm{T}\mathbf{D}_3 \tag{33c}$$

$$\boldsymbol{\Gamma}_{\mathrm{c}\,\xi\eta} = \mathbf{J}_1^\mathrm{T}\mathbf{D}_2 + \mathbf{J}_2^\mathrm{T}\mathbf{D}_1 + \mathbf{D}_1^\mathrm{T}\mathbf{D}_2 \tag{33d}$$

$$\boldsymbol{\Gamma}_{\mathrm{c}\,\eta\zeta} = \mathbf{J}_2^\mathrm{T}\mathbf{D}_3 + \mathbf{J}_3^\mathrm{T}\mathbf{D}_2 + \mathbf{D}_2^\mathrm{T}\mathbf{D}_3 \tag{33e}$$

$$\boldsymbol{\Gamma}_{\mathrm{c}\,\xi\zeta} = \mathbf{J}_1^\mathrm{T}\mathbf{D}_3 + \mathbf{J}_3^\mathrm{T}\mathbf{D}_1 + \mathbf{D}_1^\mathrm{T}\mathbf{D}_3 \tag{33f}$$

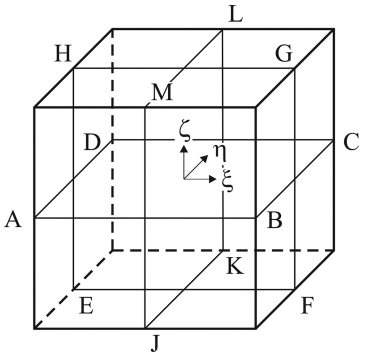

Figure 2. Sampling points of the ANS concept at reference element.

In order to cure the curvature thickness locking, we adopt the ANS concept proposed by Betsch and Stein and Bischoff and Ramm (Bischoff & Ramm 1997). The covariant compatible transverse normal strain terms $\mathrm{E}_{\mathrm{c}\,\zeta\zeta}|_{\boldsymbol{\xi}_\mathrm{K}} := \mathrm{E}^{\mathrm{K}}_{\mathrm{c}\,\zeta\zeta}$ are evaluated at so-called sampling points $\mathrm{K} = \mathrm{A}, \ldots, \mathrm{D}$, depicted in Figure 2.

Simultaneously, the covariant compatible strains are interpolated within the shell midplane of the reference element by means of bilinear shape functions Hence, the assumed transverse normal strain distribution reads

$$\mathrm{E}^{\mathrm{ANS}}_{\mathrm{c}\,\zeta\zeta} = \sum_{\mathrm{K=A}}^{\mathrm{D}} \bar{\mathrm{N}}_\mathrm{K} \mathrm{E}^{\mathrm{K}}_{\mathrm{c}\,\zeta\zeta} \tag{34}$$

$$\boldsymbol{\Gamma}^{\mathrm{ANS}}_{\mathrm{c}\,\eta\zeta} = \sum_{\mathrm{K=E}}^{\mathrm{H}} \bar{\mathrm{N}}_\mathrm{K} \boldsymbol{\Gamma}^{\mathrm{K}}_{\mathrm{c}\,\eta\zeta} \tag{35}$$

$$\boldsymbol{\Gamma}^{\mathrm{ANS}}_{\mathrm{c}\,\xi\zeta} = \sum_{\mathrm{K=J}}^{\mathrm{M}} \bar{\mathrm{N}}_\mathrm{K} \boldsymbol{\Gamma}^{\mathrm{K}}_{\mathrm{c}\,\xi\zeta} \tag{36}$$

$$\bar{\mathrm{N}}_\mathrm{K} = 1/4(1+\xi_\mathrm{K}\xi)(1+\eta_\mathrm{K}\eta) \text{ for } \mathrm{K} = \mathrm{A}, \ldots, \mathrm{D} \tag{37}$$

$$\bar{\mathrm{N}}_\mathrm{K} = 1/4(1+\xi_\mathrm{K}\xi)(1+\zeta_\mathrm{K}\zeta) \text{ for } \mathrm{K} = \mathrm{E}, \ldots, \mathrm{H} \tag{38}$$

$$\bar{\mathrm{N}}_\mathrm{K} = 1/4(1+\eta_\mathrm{K}\eta)(1+\zeta_\mathrm{K}\zeta) \text{ for } \mathrm{K} = \mathrm{J}, \ldots, \mathrm{M} \tag{39}$$

The present solid-shell formulation incorporates a reduced integration scheme within the shell plane (using one integration point), whereas a full integration is used in thickness direction, which allows for choosing arbitrary numbers of integration points (at least two), see Figure 3. Thus, all integration points are located on the normal through the center of the element defined by $\boldsymbol{\xi}^* := (0, 0, \zeta)^T$.

In order to cure volumetric locking as well as Poisson thickness locking, the EAS concept is adopted. These locking effects are treated on the level of the integration points, which can be expressed by $\hat{\mathbf{E}}_e = \hat{\mathbf{E}}^*_e$, indicating values to be evaluated in the integration points by *. Since in (34) the assumed transverse normal strain $\mathrm{E}^{\mathrm{ANS}}_{\mathrm{c}\,\zeta\zeta}$ has been defined independently of ζ,

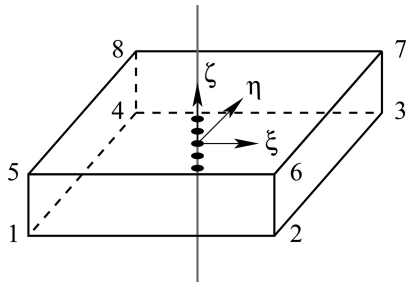

Figure 3. Solid-shell element with integration points at $\boldsymbol{\xi} = \boldsymbol{\xi}^* := (0, 0, \zeta)^T$.

the value $\mathrm{E}_{\mathrm{e}\,\zeta\zeta}$ is constructed linear in ζ in order to overcome the locking effects, and reads

$$\hat{\mathbf{E}}_\mathrm{e} = \hat{\mathbf{E}}^\star_\mathrm{e} = \mathbf{T}^0 \bar{\mathbf{B}}^\star_\mathrm{e} \mathrm{W}_\mathrm{e} \tag{40}$$

in which the interpolation matrix

$$\bar{\mathbf{B}}^\star_\mathrm{e} = [0, 0, \zeta, 0, 0, 0]^\mathrm{T} \tag{41}$$

requires only one EAS degree-of-freedom W_e. Here, $\mathbf{T}^0$ is the transformation matrix (31a) evaluated in the center of the element. For the reason of completeness, we additionally write

$$\delta\hat{\mathbf{E}}_\mathrm{e} = \delta\hat{\mathbf{E}}^\star_\mathrm{e} = \mathbf{T}^0 \bar{\mathbf{B}}^\star_\mathrm{e} \delta\mathrm{W}_\mathrm{e} \tag{42}$$

representing the virtual cartesian-enhanced strain.

In order to achieve a polynomial decoupling of the compatible Green-Lagrange strain tensor, $\hat{\mathbf{E}}_\mathrm{c} = \mathbf{T}\,\hat{\hat{\mathbf{E}}}_\mathrm{c}$, a Taylor expansion of the inverse Jacobian matrix is carried out with respect to the center of the element

$$\begin{aligned} \mathbf{J}^{-1} &\approx \mathbf{J}^{-1}\Big|_{\boldsymbol{\xi}=\mathbf{0}} + \sum_{i=1}^{3} \mathbf{J}^{-1}_{,\xi_i}\Big|_{\boldsymbol{\xi}=\mathbf{0}} \xi_i \\ &= \mathbf{J}^{-1}\Big|_{\boldsymbol{\xi}=\mathbf{0}} + \sum_{i=1}^{3} (\mathbf{J}^0)^{-1} \mathbf{J}^{\xi_i} (\mathbf{J}^0)^{-1} \xi_i \end{aligned} \tag{43}$$

up to the linear terms. The task is completed using the Taylor expansion of

$$\mathbf{J}\mathbf{J}^{-1} \approx (\mathbf{J}\mathbf{J}^{-1})\big|_{\boldsymbol{\xi}=0} + \sum_{\mathrm{i}=1}^{3} (\mathbf{J}\mathbf{J}^{-1})_{,\xi_\mathrm{i}}\big|_{\boldsymbol{\xi}=0} \xi_\mathrm{i} \tag{44}$$

as well as $\mathbf{J}\mathbf{J}^{-1} = \mathbf{I}$, which holds for arbitrary $\boldsymbol{\xi} = (\xi, \eta, \zeta)^T = (\xi_1, \xi_2, \xi_3)^T$. Inserting the coefficients of (43) into (31a), the transformation matrix is given by

$$\mathbf{T} \approx \mathbf{T}^0 + \xi\,\mathbf{T}^\xi + \eta\,\mathbf{T}^\eta + \zeta\,\mathbf{T}^\zeta \tag{45}$$

in polynomial form, where terms of higher order have been dropped, as proved sufficient in (Schwarze & Reese 2009). Nevertheless, using the approximation

(31a), the Cartesian compatible strain still represents a polynomial of higher order. For this reason, a Taylor expansion of the Cartesian compatible Green-Lagrange strain

$$\begin{aligned}\hat{\mathbf{E}}_{\mathrm{c}} &= \mathbf{T}\,\hat{\bar{\mathbf{E}}}_{c} \\ &\approx \hat{\mathbf{E}}_{\mathrm{c}}\big|_{\boldsymbol{\xi}=0} + \sum_{\mathrm{i}=1}^{3} \hat{\mathbf{E}}_{\mathrm{c},\xi_{\mathrm{i}}}\big|_{\boldsymbol{\xi}=0}\,\xi_{\mathrm{i}} \\ &\quad + \frac{1}{2}\sum_{i=1}^{3}\sum_{j\neq i=1}^{3} \hat{\mathbf{E}}_{c,\xi_i\xi_j}\Big|_{\boldsymbol{\xi}=\mathbf{0}}\,\xi_i\xi_j \\ &:= \underbrace{\hat{\mathbf{E}}_{\mathrm{c}}^{0} + \zeta\hat{\mathbf{E}}_{\mathrm{c}}^{\zeta}}_{\hat{\mathbf{E}}_{\mathrm{c}}^{\star}} + \underbrace{\xi\hat{\mathbf{E}}_{\mathrm{c}}^{\xi} + \eta\hat{\mathbf{E}}_{\mathrm{c}}^{\eta} + \xi\eta\hat{\mathbf{E}}_{\mathrm{c}}^{\xi\eta} + \eta\zeta\hat{\mathbf{E}}_{\mathrm{c}}^{\eta\zeta} + \xi\zeta\hat{\mathbf{E}}_{\mathrm{c}}^{\xi\zeta}}_{\hat{\mathbf{E}}_{\mathrm{c}}^{\mathrm{hg}}}\end{aligned} \tag{46}$$

is also carried out with respect to the center of the element. The hourglass strain term $\hat{\mathbf{E}}_{\mathrm{c}}^{\mathrm{hg}}$ represents an excellent basis for the construction of the hourglass stabilization. However, $\hat{\mathbf{E}}_{\mathrm{c}}^{*}$ is no longer quadratic in ζ. Thus, the according quadratic term is added:

$$\hat{\mathbf{E}}_{\mathrm{c}}^{\star} := \hat{\mathbf{E}}_{\mathrm{c}}^{0} + \zeta\hat{\mathbf{E}}_{\mathrm{c}}^{\zeta} + \zeta^2\hat{\mathbf{E}}_{\mathrm{c}}^{\zeta\zeta} \tag{47}$$

3.3 *The 2nd Piola-Kirchhoff stress tensor*

In this section, an efficient stress state $\hat{\mathbf{S}} := \hat{\mathbf{S}}^{*} + \hat{\mathbf{S}}^{\mathrm{hg}}$ is derived for the reduced integration, represented by the second Piola-Kirchhoff stress tensor. Here, $\hat{\mathbf{S}}^{*}$ is computed at the integration points placed at $\boldsymbol{\xi} = \boldsymbol{\xi}^{*}$ and must be able to take into account the highly nonlinear stress distributions in thickness direction. The hourglass stress part $\hat{\mathbf{S}}^{\mathrm{hg}}$ assures that the element is free of hourglass instabilities. Following (Reese 2007), a Taylor expansion of the stress field is carried out with respect to $\boldsymbol{\xi} = \boldsymbol{\xi}^{*}$.

$$\begin{aligned}\hat{\mathbf{S}} &\approx \hat{\mathbf{S}}\Big|_{\boldsymbol{\xi}=\boldsymbol{\xi}^{\star}} + \frac{\partial\hat{\mathbf{S}}}{\partial\xi}\Big|_{\boldsymbol{\xi}=\boldsymbol{\xi}^{\star}}(\xi-0) + \frac{\partial\hat{\mathbf{S}}}{\partial\eta}\Big|_{\boldsymbol{\xi}=\boldsymbol{\xi}^{\star}}(\eta-0) \\ &= \hat{\mathbf{S}}(\hat{\mathbf{E}}^{\star}) + \underbrace{\frac{\partial\hat{\mathbf{S}}(\hat{\mathbf{E}})}{\partial\hat{\mathbf{E}}}\Big|_{\boldsymbol{\xi}=\boldsymbol{\xi}^{\star}}}_{\hat{\mathbf{C}}^{\star}}\left(\frac{\partial\hat{\mathbf{E}}}{\partial\xi}\Big|_{\boldsymbol{\xi}=\boldsymbol{\xi}^{\star}}\xi + \frac{\partial\hat{\mathbf{E}}}{\partial\eta}\Big|_{\boldsymbol{\xi}=\boldsymbol{\xi}^{\star}}\eta\right) \\ &= \hat{\mathbf{S}}^{\star} + \underbrace{\hat{\mathbf{C}}^{\star}(\xi\hat{\mathbf{E}}_{c}^{\xi} + \eta\hat{\mathbf{E}}_{c}^{\eta} + \eta\zeta\hat{\mathbf{E}}_{c}^{\eta\zeta} + \xi\zeta\hat{\mathbf{E}}_{c}^{\xi\zeta})}_{:=\,\hat{\mathbf{S}}^{\mathrm{hg}}}\end{aligned} \tag{48}$$

The tangent $\hat{\mathbf{C}}^{*}$ is nonlinear in the thickness direction ζ but independent of ξ and η. In order to enable an analytical integration of the hourglass stabilization terms, $\hat{\mathbf{C}}^{*}$ is replaced by the deviatoric part of the linear-elastic material tangent $\hat{\mathbf{C}}^{\mathrm{hg}}$, which reads in Voigt notation

$$\hat{\mathbf{C}}^{\mathrm{hg}} = \mu^{\mathrm{hg}}\begin{bmatrix} 4/3 & -2/3 & -2/3 & 0 & 0 & 0 \\ -2/3 & 4/3 & -2/3 & 0 & 0 & 0 \\ -2/3 & -2/3 & 4/3 & 0 & 0 & 0 \\ 0 & 0 & 0 & 1 & 0 & 0 \\ 0 & 0 & 0 & 0 & 1 & 0 \\ 0 & 0 & 0 & 0 & 0 & 1 \end{bmatrix} \tag{49}$$

and which only depends on the artificial hourglass shear modulus μ^{hg}. In elastic problems μ^{hg} is equal to the elastic shear modulus $\mu = \mathrm{E}/(2(1+\nu))$, whereas in elastoplasticity it reads as follows:

$$\mu^{\mathrm{hg}} = \frac{1}{2}\sqrt{\frac{\mathbf{S}^{\star\,\mathrm{dev}} : \mathbf{S}^{\star\,\mathrm{dev}}}{\mathbf{E}^{\star\,\mathrm{dev}} : \mathbf{E}^{\star\,\mathrm{dev}}}} \tag{50}$$

Here, the superscript "dev" indicates the deviatoric part of the considered term. Summing up over the number of integration points ($i = 1, \ldots, n_{ip}$) leads to the following effective hourglass shear modulus

$$\begin{aligned}\mu_{\mathrm{eff}}^{\mathrm{hg}} &= \sum_{i=1}^{n_{ip}} \mu_i^{hg}\,\omega_i \\ &= \frac{1}{2}\sum_{i=1}^{n_{ip}}\left(\sqrt{\frac{\mathbf{S}^{\star dev} : \mathbf{S}^{\star dev}}{\mathbf{E}^{\star dev} : \mathbf{E}^{\star dev}}}\right)\Bigg|_{i}\omega_i\end{aligned} \tag{51}$$

where the weighting factors ω_i are scaled, such that $\sum_{i=1}^{n_{ip}}\omega_i = 1$ holds.

3.4 *Discretized weak form*

Introducing the virtual form of the cartesian enhanced Green-Lagrange strain $\delta\hat{\mathbf{E}}_e$ together with (48), Eq. (15) reads

$$\begin{aligned}\mathrm{g}_2^{\mathrm{e}} &\approx \int_{\Omega^e} \delta\hat{\mathbf{E}}_e^{T}\,\hat{\mathbf{S}}\,J^0\,d\Omega^e \\ &= \int_{\Omega^e} \delta\hat{\mathbf{E}}_e^{\star T}\,\hat{\mathbf{S}}^{\star}\,J^0\,d\Omega^e = \delta W_e\,R_w^{\star} = 0\end{aligned} \tag{52}$$

Note that the infinitesimal volume element $dV^e = J\,d\Omega^e$ has been approximated by means of $dV^e \approx J^0\,d\Omega^e$. Thereby, the integral $\int_{\Omega^e}\delta\hat{\mathbf{E}}_e^{*T}\,\hat{\mathbf{S}}^{*}\,J^0\,d\Omega^e$ vanishes, because (40) is only linear in ζ. Further, the virtual forms of (46) and (47) together with (48) are incorporated into (14), which can be written on element level as

$$\mathrm{g}_{\mathrm{l}}^{\mathrm{e}} - \mathrm{g}_{\mathrm{ext}}^{\mathrm{e}} \approx \int_{\Omega^e}\delta\mathbf{E}_c^{T}\,\hat{\mathbf{S}}\,J^0\,d\Omega^e \tag{53}$$

$$= \int_{\Omega^e}\delta\mathbf{E}_c^{\star T}\,\hat{\mathbf{S}}^{\star}\,J^0\,d\Omega^e + \int_{\Omega^e}\delta\mathbf{E}_c^{hg\,T}\,\hat{\mathbf{S}}^{hg}\,J^0\,d\Omega^e \tag{54}$$

$$= \delta\mathbf{U}_{\mathrm{e}}^{\mathrm{T}}\,\mathbf{R}_{\mathrm{u}}^{\star} + \delta\mathbf{U}_{\mathrm{e}}^{\mathrm{T}}\,\mathbf{R}_{\mathrm{u}}^{\mathrm{hg}} \tag{55}$$

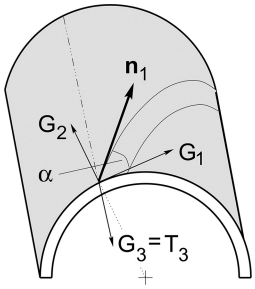

Figure 4. Cylindrical geometry.

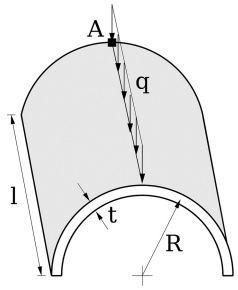

Figure 5. Pinched cylinder: geometry.

All the terms linear in the natural coordinates drop out. This leads to the desired decoupling of the parts corresponding to the integration point and the hourglass stabilization. Since the hourglass stress has deviatoric character (see Eqs. (48) and (49)), the hourglass residual vector $\mathbf{R}_{\mathrm{u}}^{\mathrm{hg}}$ simplifies to

$$\mathbf{R}_{\mathrm{u}}^{\mathrm{hg}} = \int_{-1}^{1}\int_{-1}^{1}\int_{-1}^{1} \mathbf{B}_{\mathrm{c}}^{\mathrm{hg\,dev\,T}}\,\hat{\mathbf{S}}^{\mathrm{hg}}\,\mathrm{J}^{0}\,\mathrm{d}\xi\,\mathrm{d}\eta\,\mathrm{d}\zeta \tag{56}$$

$$= \underbrace{\frac{8}{3}\mathrm{J}^{0}\mathbf{B}_{\mathrm{c}}^{\xi\,\mathrm{dev\,T}}\,\hat{\mathbf{C}}^{\mathrm{hg}}\,\hat{\mathbf{E}}_{\mathrm{c}}^{\xi\,\mathrm{dev}}}_{:=\,\mathbf{R}_{\mathrm{u}}^{\xi\,\mathrm{hg}}} + \underbrace{\frac{8}{3}\mathrm{J}^{0}\mathbf{B}_{\mathrm{c}}^{\eta\,\mathrm{dev\,T}}\,\hat{\mathbf{C}}^{\mathrm{hg}}\,\hat{\mathbf{E}}_{\mathrm{c}}^{\eta\,\mathrm{dev}}}_{:=\,\mathbf{R}_{\mathrm{u}}^{\eta\,\mathrm{hg}}}$$

$$+ \underbrace{\frac{8}{9}\mathrm{J}^{0}\mathbf{B}_{\mathrm{c}}^{\eta\zeta\,\mathrm{dev\,T}}\,\hat{\mathbf{C}}^{\mathrm{hg}}\,\hat{\mathbf{E}}_{\mathrm{c}}^{\eta\zeta\,\mathrm{dev}}}_{:=\,\mathbf{R}_{\mathrm{u}}^{\eta\zeta\,\mathrm{hg}}} + \underbrace{\frac{8}{9}\mathrm{J}^{0}\mathbf{B}_{\mathrm{c}}^{\xi\zeta\,\mathrm{dev\,T}}\,\hat{\mathbf{C}}^{\mathrm{hg}}\,\hat{\mathbf{E}}_{\mathrm{c}}^{\xi\zeta\,\mathrm{dev}}}_{:=\,\mathbf{R}_{\mathrm{u}}^{\xi\zeta\,\mathrm{hg}}}$$

in which the integration over the element domain is performed analytically. Further, bilinear terms in $\xi\eta$ drop out, because $\hat{\mathbf{S}}^{\mathrm{hg}}$ does not include any dependent summand.

3.5 *Curved structures*

For the special case of a curved structure, the vector $\mathbf{n}_1$ tangential to the fibre direction is not constant. Therefore, we have to evaluate the structural tensor in each element and integration point, respectively, using information such as geometry of the structure and the orientation angle α, see Figure 4.

The covariant basis

$$\mathbf{G}_j = \underbrace{(\mathbf{G}_i \otimes \mathbf{E}_i)}_{:=\,\mathbf{J}}\,\mathbf{E}_j \tag{57}$$

can be easily determined by means of the Jacobi matrix $\mathbf{J} = \frac{\partial \mathbf{X}}{\partial \boldsymbol{\xi}}$. A vector

$$\mathbf{T}_3 = -\frac{G_{13}}{G_{11}}\,\mathbf{G}_1 + \mathbf{G}_3 \tag{58}$$

is created fulfilling the condition $\mathbf{G}_1 \cdot \mathbf{T}_3 = 0$. Then, $\mathbf{T}_3$ is perpendicular to $\mathbf{G}_1$ and lies in the plane given by $\mathbf{G}_1$ and $\mathbf{G}_3$. The "structural vector" $\mathbf{n}_1$ is calculated using the relationship

$$\mathbf{n}_1 = \cos\alpha\,\bar{\mathbf{G}}_1 - \sin\alpha\,\bar{\mathbf{T}}_3, \tag{59}$$

where $\bar{\mathbf{T}}_3 = \mathbf{T}_3/|\mathbf{T}_3|$ and $\bar{\mathbf{G}}_1 = \mathbf{G}_1/|\mathbf{G}_1|$ denote normalized vectors. This procedure is very efficient from the computational point of view and can be carried out for any shell geometry. Note that in the special case of a cylinder, we obtain $G_{13} = 0$ and, as indicated in Figure 4, $\mathbf{G}_3 = \mathbf{T}_3$.

4 NUMERICAL EXAMPLE

As an example we investigate the pinched cylinder depicted in Figure 5. The performance of the present solid-shell element formulation is compared with the one of a classical shell element. The geometry data of the structure are defined by the length $l = 10$ m, radius $R = 5$ m and thickness $t = 0.5$ m. The distributed loading at the top of the structure is given by $q = 4.0$ kN/m. The cylinder is clamped at the bottom and consists of unidirectional laminate layers. To carry out a comparison with the shell formulation of (Stein & Tessmer 1999) a transversely isotropic model of linear elasticity is assumed, derived from the section 2.3. The material parameters of the solid-shell formulation are chosen as follows [10^6 kN/m^2]:

$$K_1^{\mathrm{iso}} = 1.39 \qquad K_1^{\mathrm{ani\,1}} = 15.42$$

$$K_2^{\mathrm{iso}} = -2.62 \qquad K_2^{\mathrm{ani\,1}} = 0.53 \tag{60}$$

$$K_1^{\mathrm{coup\,1}} = 0.32$$

The corresponding material parameters of the shell formulation read [10^6 kN/m^2]:

$$E_1 = 141 \qquad G_{12} = 6.29$$

$$E_2 = 11 \qquad G_{23} = 5.24 \tag{61}$$

$$\nu_{12} = 0.179$$

In Figure 6, the vertical displacements of the cylinder with one unidirectional layer ($\alpha = 30°$) are shown

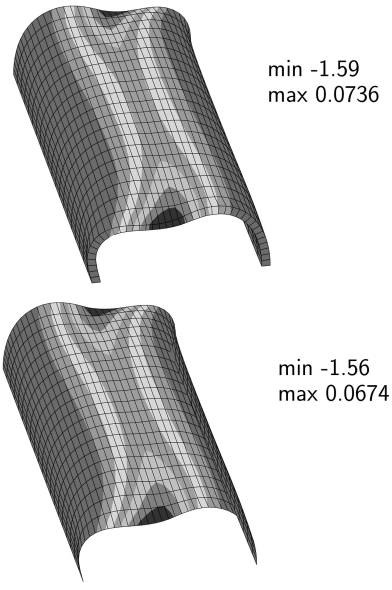

Figure 6. Vertical displacement [cm], one layer 30°.

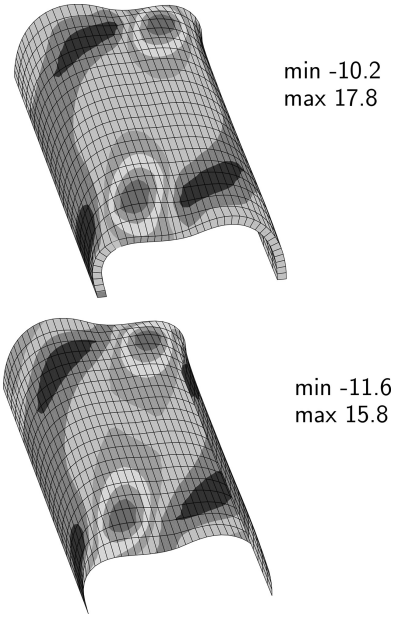

Figure 7. Stress in axial direction [kN/cm^2], one layer 30°.

(discretization with solid-shell elements at the top, discretization with shell elements at the bottom). As a result of the fiber orientation, the displacements are pointwise symmetric. Both the values of displacement and its distribution agree well. The same holds for the corresponding stresses in axial direction, see Figure 7.

In further computations, we assume that the structure shown in Figure 5 consists of two layers ($\alpha = \pm 30°$). A good agreement is achieved again (see e. g. the stresses in axial direction in Figure 8). Note

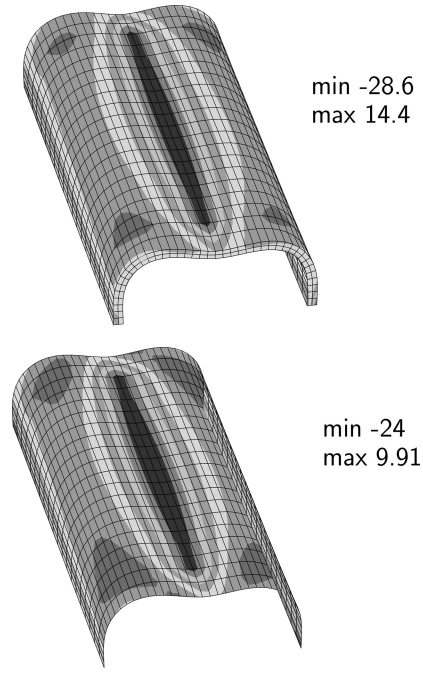

Figure 8. Stress in axial direction [kN/cm^2], two layers ±30°.

that these stresses are not perfectly symmetric because of the thickness effects. The deviation between the 3D and the shell computation is larger here, since the shell results have been evaluated exactly in the shell mid-surface whereas the stress in the upper part of Figure 8 (3D computation) refers to the middle of either the upper or the lower layer.

5 CONCLUSION

We have proposed a solid-shell finite element based on the EAS and ANS concepts which particularly suits for application to thin shell-like structures. A micromechanically motivated three-dimensional material model for fibre reinforced composites has been adopted to represent the anisotropic constitutive behaviour. Due to the use of reduced integration and hourglass stabilization, all integration points are located on the normal through the centre of the element, where the number of integration points can be chosen arbitrarily. The proposed solid-shell element has been successfully applied to a pinched cylinder consisting of one and two unidirectional layers, respectively.

ACKNOWLEDGEMENTS

Financial support of this work, related to the project Hybrid discontinuous Galerkin methods in solid

mechanics from the priority program (SPP) 1748 funded by the German Science Foundation (DFG) is gratefully acknowledged.

REFERENCES

Alves de Sousa, R. J., R. P. Cardoso, R. A. Fontes Valente, J.-W. Yoon, J. J. Grácio, & R. M. Natal Jorge (2006). A new one-point quadrature enhanced assumed strain (eas) solid-shell element with multiple integration points along thickness-part ii: nonlinear applications. *International Journal for Numerical Methods in Engineering 67*(2), 160–188.

Bischoff, M. & E. Ramm (1997). Shear deformable shell elements for large strains and rotations. *International Journal for Numerical Methods in Engineering 40*(23), 4427–4449.

Bonet, J. & A. Burton (1998). A simple orthotropic, transversely isotropic hyperelastic constitutive equation for large strain computations. *Computer methods in applied mechanics and engineering 162*(1-4), 151–164.

Brank, B., J. Korelc, & A. Ibrahimbegović (2002). Nonlinear shell problem formulation accounting for through-the-thickness stretching and its finite element implementation. *Computers & structures 80*(9), 699–717.

Cardoso, R. P. & J. W. Yoon (2005). One point quadrature shell element with through-thickness stretch. *Computer Methods in Applied Mechanics and Engineering 194*(9), 1161–1199.

Cardoso, R. P., J. W. Yoon, M. Mahardika, S. Choudhry, R. Alves de Sousa, & R. Fontes Valente (2008). Enhanced assumed strain (eas) and assumed natural strain (ans) methods for one-point quadrature solid-shell elements. *International Journal for Numerical Methods in Engineering 75*(2), 156–187.

Holzapfel, G. A., R. Eberlein, P. Wriggers, & H. Weizsäcker (1996). A new axisymmetrical membrane element for anisotropic, finite strain analysis of arteries. *Communications in numerical methods in engineering 12*(8), 507–517.

Kim, D.-N. & K.-J. Bathe (2008). A 4-node 3d-shell element to model shell surface tractions and incompressible behavior. *Computers & Structures 86*(21), 2027–2041.

Kim, K., G. Liu, & S. Han (2005). A resultant 8-node solid-shell element for geometrically nonlinear analysis. *Computational Mechanics 35*(5), 315–331.

Klinkel, S., F. Gruttmann, & W. Wagner (2006). A robust non-linear solid shell element based on a mixed variational formulation. *Computer methods in applied mechanics and engineering 195*(1), 179–201.

Klinkel, S., F. Gruttmann, & W. Wagner (2008). A mixed shell formulation accounting for thickness strains and finite strain 3d material models. *International journal for numerical methods in engineering 74*(6), 945–970.

Reese, S. (2003). Meso-macro modelling of fibre-reinforced rubber-like composites exhibiting large elastoplastic deformation. *International Journal of Solids and Structures 40*(4), 951–980.

Reese, S. (2007). A large deformation solid-shell concept based on reduced integration with hourglass stabilization. *International Journal for Numerical Methods in Engineering 69*(8), 1671–1716.

Reese, S., T. Raible, & P. Wriggers (2001). Finite element modelling of orthotropic material behaviour in pneumatic membranes. *International journal of solids and structures 38*(52), 9525–9544.

Rüter, M. & E. Stein (2000). Analysis, finite element computation and error estimation in transversely isotropic nearly incompressible finite elasticity. *Computer methods in applied mechanics and engineering 190*(5), 519–541.

Schwarze, M. & S. Reese (2009). A reduced integration solid-shell finite element based on the eas and the ans concept-geometrically linear problems. *International Journal for Numerical Methods in Engineering 80*(10), 1322–1355.

Schwarze, M. & S. Reese (2011). A reduced integration solid-shell finite element based on the eas and the ans concept-large deformation problems. *International Journal for Numerical Methods in Engineering 85*(3), 289–329.

Schwarze, M., I. N. Vladimirov, & S. Reese (2011). Sheet metal forming and springback simulation by means of a new reduced integration solid-shell finite element technology. *Computer Methods in Applied Mechanics and Engineering 200*(5), 454–476.

Stein, E. & J. Tessmer (1999). Theory and computation of multilayer composites. In *Mechanics of Composite Materials and Structures*, pp. 369–378. Springer.

Svendsen, B. (1994). On the representation of constitutive relations using structure tensors. *International journal of engineering science 32*(12), 1889–1892.

Valente, R. F., R. A. d. Sousa, & R. N. Jorge (2004). An enhanced strain 3d element for large deformation elastoplastic thin-shell applications. *Computational Mechanics 34*(1), 38–52.

Vu-Quoc, L. & X. Tan (2003). Optimal solid shells for non-linear analyses of multilayer composites. i. statics. *Computer methods in applied mechanics and engineering 192*(9), 975–1016.

Weiss, J. A., B. N. Maker, & S. Govindjee (1996). Finite element implementation of incompressible, transversely isotropic hyperelasticity. *Computer methods in applied mechanics and engineering 135*(1–2), 107–128.